

Pixel-Wise Recognition for Holistic Surgical Scene Understanding

Nicolás Ayobi^{a,*}, Santiago Rodríguez^{a,1}, Alejandra Pérez^{a,1}, Isabela Hernández^{a,1}, Nicolás Aparicio^a, Eugénie Dessevres^a, Sebastián Peña^b, Jessica Santander^b, Juan Ignacio Caicedo^b, Nicolás Fernández^{c,d}, Pablo Arbeláez^{a,*}

^aCenter for Research and Formation in Artificial Intelligence (CinfonIA), Universidad de los Andes, Carrera 1 No. 18a-12, 111711 Bogota, Colombia

^bDepartment of Urology, Fundación Santa Fe de Bogotá, Carrera 7 No. 118 - 09, 111071 Bogota, Colombia

^cDivision of Urology, Seattle Children's Hospital, 4800 Sand Point Way NE, 98105 Seattle, Washington, USA

^dDepartment of Urology, University of Washington, 1410 NE Campus Pkwy, 98195 Seattle, Washington, USA

ABSTRACT

This paper presents the Holistic and Multi-Granular Surgical Scene Understanding of Prostatectomies (GraSP) dataset, a curated benchmark that models surgical scene understanding as a hierarchy of complementary tasks with varying levels of granularity. Our approach enables a multi-level comprehension of surgical activities, encompassing long-term tasks such as surgical phases and steps recognition and short-term tasks including surgical instrument segmentation and atomic visual actions detection. To exploit our proposed benchmark, we introduce the Transformers for Actions, Phases, Steps, and Instrument Segmentation (TAPIS) model, a general architecture that combines a global video feature extractor with localized region proposals from an instrument segmentation model to tackle the multi-granularity of our benchmark. Through extensive experimentation, we demonstrate the impact of including segmentation annotations in short-term recognition tasks, highlight the varying granularity requirements of each task, and establish TAPIS's superiority over previously proposed baselines and conventional CNN-based models. Additionally, we validate the robustness of our method across multiple public benchmarks, confirming the reliability and applicability of our dataset. This work represents a significant step forward in Endoscopic Vision, offering a novel and comprehensive framework for future research towards a holistic understanding of surgical procedures.

Keywords: Holistic Surgical Scene Understanding, Robot-Assisted Surgery, Endoscopic Vision, Surgical Workflow Analysis, Surgical Instrument Segmentation, Vision Transformers

1. Introduction

Robot-assisted surgery (RAS) has emerged as a pivotal advancement in modern surgical practices (Goh and Ali (2022)), offering a minimally invasive option compared to common open surgeries and providing enhanced precision over conventional laparoscopic techniques (Chuchulo and Ali (2023)). This innovative approach provides enhanced instrumentation, visualization, and dexterity capabilities, greatly benefiting surgeons in the operating room and significantly reducing patient complications (Lanfranco et al. (2004); van Amsterdam et al. (2022)). However, robotic surgery currently faces several limitations, such as the lack of automated assistance from the robot (Fiorini (2021)), minimal image-based force feedback (Rassi and Rassi (2020)), and a steep learning curve for specific surgeries (Kim et al. (2019); Vining et al. (2021)). Nevertheless, the extensive and complex data collected by surgical robots provide a unique opportunity to develop data-based solutions that enrich the robot with surgical intelligence (Maier-Hein et al. (2017)).

These advancements would augment surgical processes, offering ways to overcome multiple challenges in robotic surgical practices.

A step towards exploiting the full potential of surgical robotic systems is the comprehension of the visual information relayed by the robot's endoscope (Mascagni et al. (2022)). This understanding extends beyond merely recognizing and categorizing present elements, such as anatomical structures and surgical instruments, in the visual data. Instead, it involves fully integrating the temporal and spatial dimensions for a coherent and holistic interpretation of surgical scenes that can be useful for the robotic system. Achieving this higher level of understanding can lead to enhanced augmented reality systems (Qian et al. (2020); Tanzi et al. (2021)), context-aware surgical assistance (Katić et al. (2013); Kolbinger et al. (2023)), improved surgical education methods (Maier-Hein et al. (2017)), and even the development of semi-automated surgical interventions.

In light of this, Endoscopic Vision is a critical area of Surgical Data Science that concentrates on interpreting and analyzing the rich visual information captured during endoscopic procedures (Fu et al. (2021); Maier-Hein et al. (2022)). This field tackles surgical scene understanding with multiple methodological approaches representing essential components of image-guided surgical cognition like comprehension of environmen-

*Corresponding authors: Nicolás Ayobi and Pablo Arbeláez
e-mail: n.ayobi@uniandes.edu.co (Nicolás Ayobi),

pa.arbelaez@uniandes.edu.co (Pablo Arbeláez)

¹Equal contribution

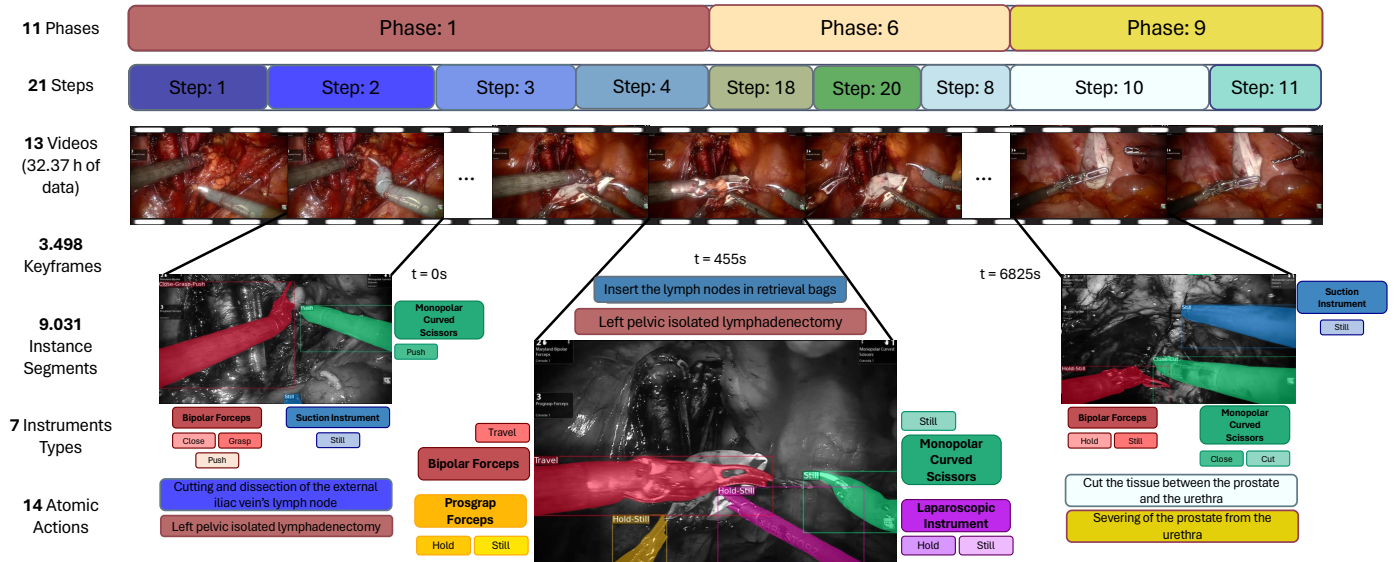


Fig. 1: **The GraSP Dataset** formulates a holistic understanding of robot-assisted Radical Prostatectomy videos by studying four hierarchical tasks annotated in their highest granularity. These tasks include two long-term tasks, recognition of surgical phases and steps, and two short-term tasks, surgical instrument segmentation and atomic action detection. Figure best viewed in color.

tal geometry (Allan et al. (2020); Wang et al. (2022)), surgical procedure knowledge (Maier-Hein et al. (2021); Wagner et al. (2023)), and understanding of agent-environment relations (Islam et al. (2020); Nwoye et al. (2020)). The specific visual cues that these approaches prioritize or the particular aspects of the surgical environment they study lead to distinct requirements in terms of visual recognition, temporal awareness, and spatial granularity. Among these approaches, surgical workflow analysis studies the complex interactions between surgical instruments and anatomical landmarks (Padoy et al. (2012); Valderama et al. (2022)). This area aims to comprehend the temporal progression of surgical procedures by understanding the activities performed throughout the sequence of surgical scenes in a surgical video. For instance, the most studied task in surgical workflow analysis is the recognition of surgical phases in a given endoscopic video clip or image (Demir et al. (2023)). Even so, surgical workflow analysis has an implicit need for a multi-recognition approach that identifies the different agents and activities in the surgical setting (Twinanda et al. (2016); Maier-Hein et al. (2021)). Hence, other surgical workflow approaches extend to the recognition of surgical steps, surgical gestures, the presence of surgical instruments, or the presence of actions (Demir et al. (2023)).

Despite the advancements in multi-task approaches of surgical workflow analysis benchmarks, there remains a significant gap in the literature concerning a holistic understanding of the multi-level nature of surgical interventions. A fundamental limitation of most current surgical workflow analysis benchmarks is their constrained study of the spatial dimensions of endoscopic images. Specifically, current benchmarks often disregard the visual localization of the constitutive acting agents, which are the surgical instruments in a surgical procedure (Nwoye et al. (2022)). Notably, just a few benchmarks of laparoscopic surgeries integrate surgical instrument detection or

segmentation into surgical workflow analysis, a gap primarily due to the time-consuming nature of gathering these annotations (Maier-Hein et al. (2021); Grammatikopoulou et al. (2021)). This oversight is evident, as instrument segmentation, detection, or tracking, despite their critical relevance, have mostly been treated as independent areas from surgical workflow analysis. For example, the Endoscopic Vision challenges on instrument segmentation (Bodenstedt et al. (2018); Allan et al. (2019, 2020)) have become the standard benchmarks on pixel-wise instrument recognition, but besides external annotations of instrument-tissue interactions (Islam et al. (2020)), these frameworks do not provide annotations for other surgical workflow analysis tasks.

Nonetheless, integrating visual locations of surgical instruments has primordial implications for robot-assisted surgery, as current robotic systems generate instrument utilization signals but lack the capability to relate these presence data to their visual locations within the surgical scene (Du et al. (2016); Su et al. (2018); Guan et al. (2023)). On top of that, instrument segmentation would allow surgical robotic systems to benefit from the most granular approach to instrument recognition and thus acquire a notion of instrument shape (Baby et al. (2023)), pose (Du et al. (2018)), and pixel-wise boundaries (García-Peraza-Herrera et al. (2017)), which, in turn, can lead to multiple augmented reality applications (Qian et al. (2020); De Backer et al. (2023)). Therefore, bridging this gap between instrument segmentation and surgical workflow analysis is essential for advancing the field of Robotic Endoscopic Vision.

A second area for improvement in current surgical workflow analysis and Endoscopic Vision benchmarks, closely related to the first, concerns the exploitation of the hierarchical complementarity among different visual perception tasks in Endoscopic Vision. Initially, some benchmarks treat recognition tasks such as phases recognition (Stauder et al. (2017)) and ac-

tion recognition (Bawa et al. (2021); Goodman et al. (2021)) as isolated entities rather than interdependent components of a cohesive surgical process. For example, as shown in Table 1, the LapChole dataset (Stauder et al. (2017)) focuses on the sole prediction of surgical phases in traditional Laparoscopic Surgeries (LS), the CATARACTS dataset (Al Hajj et al. (2019)) initially focused only on tool presence recognition in Cataract Surgery (CS), and the JIGSAWS (Ahmidi et al. (2017)), LR-SAO (Sharghi et al. (2020)), ESAD (Bawa et al. (2021)) and RARP45 (van Amsterdam et al. (2022)) benchmarks only study gestures and actions in either RAS data or Robot-Assisted Surgical Training (ST) data.

Similarly, multi-task benchmarks tend to focus on a few levels of visual understanding, like frame-level binary presence prediction or video-level temporal segmentation of phases, rather than tackling a comprehensive range of levels and granularities in the visual, temporal, and spatial dimensions. The Cholec80 benchmark (Twinanda et al. (2016)) and the re-annotated CATARACTS benchmark (Al Hajj et al. (2019); Zisimopoulos et al. (2018)) study one video-level task (phase recognition) with one frame-level presence recognition task (instrument presence) in LS data. The CholecT40 (Nwoye et al. (2020)), CholecT50 (Nwoye et al. (2022)), and HeiChole (Wagner et al. (2023)) benchmarks include more frame-level presence recognition tasks like the presence of actions and anatomical targets in LS as well. Alternatively, the MISAW framework (Hualmé et al. (2021)) is the only dataset to consider multiple granularities in video-level tasks by annotating phases, steps, and activities in ST data. Conversely, the HeiCo (Maier-Hein et al. (2021)) and CaDIS (Grammatikopoulou et al. (2021)) datasets are pioneering benchmarks in combining video-level phase recognition with pixel-wise instrument recognition in LS and CS data, but they disregard action information. Still, existing frameworks predominantly focus on single video-level tasks with some frame-wise recognition tasks without adequately addressing the multiple hierarchical granularities required for holistic surgical workflow analysis.

In our initial work (Valderrama et al. (2022)), we laid the foundation for studying surgical scenes across multiple levels of granularity in both the temporal and spatial dimensions. The empirical framework presented herein models surgical procedures as a hierarchy of semantic tasks encompassing long-term video-level tasks, such as phase and step recognition, and short-term spatio-temporal tasks, including instrument and atomic visual action localization. We base our modeling on the Atomic Visual Actions (AVA) formulation in Gu et al. (2018) and the activity understanding theory of Barker and Wright (1954). The latter presents a hierarchical comprehension of activity, where the finest expressions of activity are the atomic interactions and movements performed by the main acting agents of a scene, and the highest comprehension level of activity corresponds to the development of complex and general objectives. Our work adapts these concepts into surgical workflow analysis. Long-term recognition of phases and steps corresponds to a higher-level understanding of sequences of necessary goals in surgical reasoning. In contrast, short-term tasks of identifying instruments and their atomic actions are akin to the lower-level notion

of atomic movements done by an acting agent.

Thus, the rationale behind our framework hinges on a stratification of surgical analysis tasks where the apex is the recognition of surgical phases, representing the highest and most general level of understanding. These phases can be further decomposed into detailed steps, a more fine-grained level of reasoning. Each step involves the utilization of particular surgical instruments, which perform specific atomic actions. We introduce surgical atomic actions as our framework’s lowest and most fine-grained level of understanding, which provides a practical way of studying surgical activities and allows the further reconstruction of the activity hierarchy (Gu et al. (2018)). By breaking down the procedure into these distinct yet interconnected levels, we emphasize the importance of understanding the individual components and their collective dynamics. Such analysis is crucial for a holistic understanding of the surgical scene, capturing the essence of both the macro and micro-elements of surgeries.

In this work, we extend our original framework (Valderrama et al. (2022)) by integrating pixel-wise recognition of instruments to achieve the highest level of spatial recognition granularity. For this purpose, we transformed our original instrument detection annotations into detailed instrument segmentation annotations. Hence, we introduce a new instrument segmentation task in our dataset and a fully instance-based evaluation benchmark that aligns more closely with the practical needs of surgical scene analysis. Additionally, we augment our dataset with five new fully annotated videos, and we have established specific training, validation, and testing splits with per-task metrics for benchmarking. The newly annotated videos form the test set, while the previous videos are the training set divided into two explicitly defined folds for a two-fold cross-validation process. We curate and revise all our annotations to eliminate noise and inconsistencies, ensuring the highest level of data integrity. Our extension in data accounts for more than a 55% increase in data size and annotation over the initial PSI-AVA dataset. This advanced version of our framework is called the Holistic and Multi-Granular Surgical Scene Understanding of Prostatectomies (GraSP) dataset. Table 1 shows the contributions of our benchmark compared to previous literature. The discussed improvements make our benchmark the first publicly available in the robotic surgery domain with a multi-task approach and an instrument instance segmentation task using real in-patient surgical data on human subjects. To our knowledge, GraSP is the first Endoscopic Vision framework to consider multiple long and short-term tasks in their most fine-grained form.

Besides the extensions to our benchmark, we propose the Transformers for Actions, Phases, Steps, and Instrument Segmentation (TAPIS) model. A generalized, fully transformer-based architecture that combines a global video feature extractor with a localized region proposal network to tackle each task in the GraSP benchmark. TAPIS builds upon our previous outstanding methodologies for holistic surgical scene understanding (Valderrama et al. (2022)) and instrument segmentation (Ayobi et al. (2023)). To fully include our novel instrument segmentation benchmark, we transition from the instrument detector in Valderrama et al. (2022) into an instru-

ment segmentation baseline that provides detailed region proposals and shape-wise features of surgical instruments. Our experimentation demonstrates that these regions and their features consistently enhance recognition accuracy and enrich the atomic action recognition capabilities. We also propose an improved *region classification head* that exploits transformers' cross-attention to fully incorporate the totality of the rich temporal embeddings computed by the video feature extractor. Finally, we validate our method's robustness and applicability by comparing it with alternative baselines and our previous approaches and testing it in various publicly available frameworks. Our results demonstrate that TAPIS achieves outstanding performances in multiple datasets and establishes the state-of-the-art in our GraSP benchmark. Our efforts in dataset extension, methodological innovation, and benchmark validation significantly contribute to the research in surgical data science and pave the way towards a holistic understanding of surgical procedures.

To summarize, the main contributions of our work are:

- We propose the GraSP dataset for holistic surgical scene understanding, a curated and augmented version of the PSI-AVA benchmark, with defined benchmark splits and more than a 55% increase in data and annotations.
- We introduce a new instrument segmentation task into our benchmark as the most granular approach to instrument localization.
- We present a generalized, transformer-based architecture that strongly outperforms all previous baselines across all tasks of the GraSP framework.

For the sake of fairness and reproducibility and to promote further research in holistic and multi-granular surgical scene understanding, we make public the entire GraSP dataset along with our source codes and pretrained models under the MIT License in <https://github.com/BCV-Uniandes/GraSP>.

2. Related Work

2.1. Surgical Workflow Analysis Benchmarks

Over the years, the evolution of datasets for surgical workflow analysis has substantially impacted the field. In 2014, the JIGSAWS dataset (Gao et al. (2014)) emerged as a pioneering effort by combining video and kinematic data with annotations for three fundamental surgical tasks in robotic surgery and fifteen surgical gestures. Nevertheless, this dataset was acquired in a simulated training laboratory, distancing it from an actual surgical setting. Responding to the demand for *in vivo* human surgical data, the Cholec80 dataset (Twinanda et al. (2016)) introduced a collection of laparoscopic cholecystectomy surgeries with annotations for surgical phase and tool presence recognition. Simultaneously, TUM LapChole (Stauder et al. (2017)), another dataset for laparoscopic cholecystectomies, also labeled surgical phases within a smaller collection of surgeries. Given that the previous datasets focus on traditional laparoscopic procedures, the Nephrec9 dataset (Nakawala (2017)) was introduced as the first surgical workflow analysis dataset with real

RAS data of Robot-Assisted Partial Nephrectomy (RAPN) procedures. Remarkably, the Nephrec9 dataset provides temporal annotations at a more granular level, offering information about surgical steps instead of broader surgical phases.

In a different domain, the CATARACTS dataset (Al Hajj et al. (2019)) introduced an annotated video collection tailored for cataract surgeries. The dataset was initially labeled for surgical instrument recognition and expanded to include annotations for surgical phase recognition (Zisimopoulos et al. (2018)) and semantic segmentation of anatomic landmarks and surgical instruments (Grammatikopoulou et al. (2021)), but it does not provide information about surgical actions or steps. Within this same surgical data type, the Cataract-101 dataset (Schoeffmann et al. (2018)) subsequently introduced a collection of 101 videos while still maintaining high-level phase annotations.

A notable advancement in laparoscopic surgery datasets occurred with the introduction of the HeiCo dataset (Maier-Hein et al. (2021)) and the CholecT40, 45, and 50 datasets (Nwoye et al. (2020, 2022); Nwoye and Padoy (2023)). The HeiCo dataset features 30 surgical videos and sensor data from various laparoscopic procedures such as proctocolectomy, rectal resection, and sigmoid resection. The annotations include both phase recognition and surgical instrument segmentation. Remarkably, including diverse surgeries within this dataset allowed for exploring domain generalization in surgical workflow analysis. Nevertheless, it does not include more detailed temporal information, such as action and step recognition, crucial for comprehensive understanding across diverse annotation levels. Contrarily, the CholecT40, 45, and 50 datasets (Nwoye et al. (2020, 2022); Nwoye and Padoy (2023)) used a subset of Cholec80's data and included annotations for presence recognition of instruments, actions, and anatomical targets via surgical action triplets, thus allowing a more fine-grained study of surgical workflow but still disregarding steps recognition or localized information.

Following this effort, the HeiChole dataset (Wagner et al. (2023)) presented a detailed collection of 33 laparoscopic cholecystectomies and is also aimed at multi-level understanding by presenting phase recognition along with frame-level instrument and action presence recognition. While more specialized in its scope than the HeiCo dataset, HeiChole did not include crucial spatially localized information or step recognition within surgical procedures.

Even though the previously mentioned datasets have offered valuable insights into surgical workflow analysis within their specific surgical domains, they all confine their video-level annotations to studying a single long-term task. The MISAW dataset (Hualmé et al. (2021)) emerged as a crucial addition to surgical workflow analysis to address the previous gap in existing datasets. Focused on micro-surgical anastomosis on artificial blood vessels, MISAW encompassed 27 sequences with videos, kinematic data, and temporal annotations across three granularity levels: phases, steps, and specific activities that are constituted by a surgical gesture, a target, and a surgical instrument. This dataset marked a significant stride towards enabling multi-level surgical workflow analysis. However, the artificial nature of the data limits its applicability to real-time surgical

Table 1: **Our GraSP benchmark compared with current surgical workflow analysis and endoscopic vision datasets.** Each row represents a current Endoscopic Vision dataset, and each column is a possible dataset attribute corresponding to either the inclusion of multiple levels of semantic comprehension, annotations of a particular surgical scene understanding the task, video duration, public availability, or data source type. We show whether an attribute is present (✓), absent (–), has a different formulation (*), or its information is unavailable (?). We also indicate if the source of the provided data is from traditional Laparoscopic Surgery (LS), *ex vivo* Surgical Training Procedures (ST), Cataract Surgery (CS), Robot-Assisted Surgery on animal subjects (RASA), Robot-Assisted Surgery on human subjects (RASH), or multiple Open Surgery types (MOS). Our GraSP dataset, shown in bold, is the first publicly available benchmark to provide all the presented attributes. Note: We combine the Instrument Detection and Instrument Segmentation attributes to identify datasets with instance-level annotations. Datasets with both attributes have Instrument Instance Segmentation annotations, datasets with only Instrument Detection have bounding box annotations, and datasets with only Instrument Segmentation annotations have Semantic Segmentation annotations.

| Dataset | Multi-level Understanding | Phase Recognition | Step Recognition | Instrument Recognition | Instrument Detection | Instrument Segmentation | Action Recognition | Action Localization | Video hours | Publicly Available | Data Domain |
|---|---------------------------|-------------------|------------------|------------------------|----------------------|-------------------------|--------------------|---------------------|-------------|--------------------|-------------|
| Cholec80 (Twinanda et al. (2016)) | ✓ | ✓ | – | ✓ | – | – | – | – | 51.25 | ✓ | LS |
| TUM LapChole (Stauder et al. (2017)) | – | ✓ | – | – | – | – | – | – | 23.24 | ✓ | LS |
| JIGSAWS (Ahmidi et al. (2017)) | – | – | – | – | – | – | ✓* | * | 2.62 | ✓ | ST |
| Nephrec9 (Ahmidi et al. (2017)) | – | – | ✓ | – | – | – | – | – | 10.52 | ✓ | RASH |
| EndoVis 2015 (Bodenstedt et al. (2018)) | – | – | – | ✓ | – | ✓ | – | – | 0.10 | ✓ | LS, ST |
| EndoVis 2017 (Allan et al. (2019)) | – | – | – | ✓ | ✓ | ✓ | – | – | 0.83 | ✓ | RASA |
| CATARACTS (Al Hajj et al. (2019); Zisimopoulos et al. (2018)) | ✓ | ✓ | – | ✓ | – | – | – | – | 9.2 | ✓ | CS |
| CaDIS (Zisimopoulos et al. (2018); Grammatikopoulou et al. (2021)) | ✓ | ✓ | – | ✓ | – | ✓ | – | – | 9.1 | ✓ | CS |
| EndoVis 2018 (Allan et al. (2020); González et al. (2020); Islam et al. (2020)) | – | – | – | ✓ | ✓ | ✓ | ✓ | ✓ | 1.58 | ✓ | RASA |
| LSRAO (Sharghi et al. (2020)) | – | – | – | – | – | – | ✓ | – | ? | – | RASH |
| CholecT40, T45 & T50 (Nwoye et al. (2020, 2022)) | ✓ | ✓ | – | ✓ | – | – | ✓ | – | 28.03 | ✓ | LS |
| HeiCo (Maier-Hein et al. (2021); Roß et al. (2021)) | ✓ | ✓ | – | ✓ | ✓ | ✓ | – | – | 96.12 | ✓ | LS |
| MISAW (Huaulmé et al. (2021)) | ✓ | ✓ | ✓ | –* | – | – | – | – | 1.52 | ✓ | ST |
| ESAD (Bawa et al. (2021)) | – | – | – | – | – | – | ✓ | ✓ | 9.33 | ✓ | RASH |
| AVOS (Goodman et al. (2021)) | – | – | – | ✓ | ✓ | – | ✓ | ✓ | 4.7 | – | MOS |
| RARP45 (van Amsterdam et al. (2022)) | – | – | – | – | – | – | ✓* | – | 3.2 | ✓ | RASH |
| RARR (Kolbinger et al. (2023)) | – | ✓ | – | – | – | – | – | – | 393.3 | – | RASH |
| HeiChole (Wagner et al. (2023)) | ✓ | ✓ | – | ✓ | – | – | ✓ | – | 22 | ✓ | LS |
| PSI-AVA (Valderrama et al. (2022)) | ✓ | ✓ | ✓ | ✓ | ✓ | – | ✓ | ✓ | 20.45 | ✓ | RASH |
| GraSP (this-work) | ✓ | ✓ | ✓ | ✓ | ✓ | ✓ | ✓ | ✓ | 32.37 | ✓ | RASH |

scene understanding.

In contrast, the RARP-45 dataset (van Amsterdam et al. (2022)) stands out as a significant contribution by addressing the need for finer-grained temporal annotation within human *in vivo* robot-assisted interventions. This dataset comprises a comprehensive collection of video and kinematics data derived from Robot-Assisted Radical Prostatectomies (RARP), enriched with temporal segment annotations for fine-grained bimanual gesture recognition. Nevertheless, it solely offers surgical gesture annotations. Within the same RAS domain, the recently introduced RARR dataset (Kolbinger et al. (2023)) allows multi-level understanding by introducing annotations for higher-level phase recognition and lower-level anatomical targets segmentation in human *in vivo* robot-assisted rectal resection (RARR). Despite providing spatial and temporal annotations, it does not address instrument recognition or the multi-granularity of broken-down phases into steps or surgical actions.

In exploring surgical workflow analysis advancements, we acknowledged the need for a single benchmark encompassing hierarchically various granularity levels of long- and short-term surgical workflow tasks. We especially recognize this need in datasets utilizing real RAS data on human subjects. Our dataset, as an extension of our previously proposed PSI-AVA dataset (Valderrama et al. (2022)), provides annotations with high-level temporal information regarding phases and their division into steps, a more detailed temporal understanding. Thus, ours is the only surgical workflow analysis dataset up to date that provides both levels of semantic understanding with human *in vivo* data. Additionally, our dataset contains detailed low-level spatio-temporal information on atomic actions, and, in this work, we include precise delineation of the different surgical instruments for a more detailed understanding of instru-

ment poses and surgical gestures. Consequently, our work addresses multiple previous needs in surgical scene understanding by offering a holistic comprehension of the surgical workflow at different granularity levels with real RAS data on human subjects.

2.2. Surgical Instrument Segmentation

Most benchmarks for surgical instrument segmentation started as part of the Endoscopic Vision Grand Challenge². The inaugural benchmark in this series was the 2015 Instrument Segmentation and Tracking Challenge (Endovis 2015) (Bodenstedt et al. (2018)), which provided short video clips of laparoscopic colorectal surgeries and some *ex vivo* robot-assisted procedures. The corresponding semantic segmentation annotations focused on the sub-parts of the surgical instruments. Later, the 2017 Robotic Instrument Segmentation Challenge (Endovis 2017) (Allan et al. (2019)) introduced a more complex approach to instrument segmentation by proposing the recognition of instrument types. Thus, Endovis 2017 provided instance-wise annotations for entire instruments and their sub-type label in multiple videos of robot-assisted porcine procedures. The 2018 Robotic Scene Segmentation Challenge (Endovis 2018) (Allan et al. (2020)) further expanded the scope of these benchmarks, offering surgical scene semantic segmentation in robot-assisted porcine procedures. These detailed annotations included instrument parts, anatomical structures, and specific surgical objects like clips, threads, and needles, which provided a richer context for segmentation tasks. Still, all these benchmarks solely focus on segmentation tasks, lacking annotations for surgical workflow analysis tasks, and none of them provide data from

²<https://endovis.grand-challenge.org/>

human *in vivo* robot-assisted procedures. Also, all these benchmarks were mainly formulated for semantic segmentation approaches, as they all use semantic segmentation-based annotations and metrics, and only Endovis 2017 could be directly employed for instance segmentation. Thus, these benchmarks significantly ignored the instance-level nature of surgical instrument segmentation.

In our previous research (González et al. (2020)), our team adapted the original annotations from Endovis 2018 for instance-level segmentation of instrument types. We used these annotations to fully exploit the potential of mask classification models for instance segmentation (He et al. (2017)). This approach demonstrated the superior potential of instance-based approaches for surgical instrument segmentation, as we strongly outperformed all previous semantic segmentation-based methods (González et al. (2020)). Nevertheless, we kept a semantic segmentation evaluation metric to maintain comparability with previous studies. Alternatively, Islam et al. (2020) re-annotated the data from Endovis 2018 for detecting instruments and anatomical structures, along with annotations for the interactions between instruments and tissues. These interaction annotations are analogous to instrument action annotations and provide a deeper understanding of the dynamics within the surgical scene.

Finally, the CaDIS dataset (Grammatikopoulou et al. (2021)) and the HeiCo dataset (Maier-Hein et al. (2021)) were the first ones to provide instrument segmentation and video-level task annotations. The CaDIS dataset is a subset of the CATARACTS dataset (Al Hajj et al. (2019)), which focuses on cataract surgery and provides phase recognition annotations. CaDIS offers entire scene semantic segmentation that includes instrument types and anatomical structures. Further, the 2019 ROBUST-MIS challenge (Roß et al. (2021)) used the videos of the HeiCo dataset (Maier-Hein et al. (2021)) (also with phases recognition annotations) for instance-level instrument-type segmentation and established the first instance-based evaluation metric. Still, these datasets use different data sources from robot-assisted surgery and do not cover relevant recognition tasks like steps or action recognition. Our dataset aims to bridge the gaps mentioned above, offering pixel-level annotations for robotic surgical instrument segmentation, along with the atomic actions performed by those instruments and multiple video-level recognition tasks in real robot-assisted surgical footage.

2.3. Surgical Action Recognition

The concept of action recognition in computer vision began as a classification task in short clips (Schuldt et al. (2004); Blank et al. (2005); Marszalek et al. (2009); Kuehne et al. (2011); Soomro et al. (2012) and extended videos (Over et al. (2013); Karpathy et al. (2014); Abu-El-Haija et al. (2016); Kay et al. (2017); Goyal et al. (2017); Zhao et al. (2019)), where a single action category was associated with a specific time segment. Over time, the problem expanded to multiple categories within each time segment (Caba Heilbron et al. (2015); Idrees et al. (2017); Yeung et al. (2018); Sigurdsson et al. (2016)). Some works further extended the problem to include spatial location detection of actions (Ke et al. (2005); Rodriguez et al.

(2008); Yuan et al. (2009); Jhuang et al. (2013)). Subsequently, AVA (Gu et al. (2018)) introduced an agent-centric approach, suggesting that a video consisted of various agents capable of independently executing multiple actions and interacting with each other and their environment. This approach incorporated atomic actions, which divided categories into finer components for a richer and more complete understanding of actions in videos.

In the surgical context, action recognition corresponds to a higher temporal granularity in surgical scene understanding (Khatibi (2020); Rupprecht et al. (2016)). The JIGSAWS dataset (Gao et al. (2014)) made early efforts in this direction by defining actions as gestures within the surgical environment. This dataset adopted a classification framework, including 15 distinct categories observed in *ex vivo* surgery videos recorded by the da Vinci Surgical System (dVSS). However, as mentioned earlier, it derives its data from external sources to the patient, limiting its representativeness in real-life cases

Subsequently, Sharghi et al. (2020) introduced a video dataset captured within an operating room, featuring ten specific actions performed by medical personnel during robot-assisted surgeries. Nevertheless, this dataset does not include scenarios involving in-patient data. Later, the CholecT40 dataset (Nwoye et al. (2020)) and its subsequent versions, CholecT45 and CholecT50 (Nwoye et al. (2022); Nwoye and Padoy (2023)), formulated the challenge of action identification in laparoscopic cholecystectomy surgeries as triplets. The task was defined as an instrument that executes an action on a target, adopting the structure of $\langle \text{instrument}, \text{verb}, \text{target} \rangle$. Correspondingly, the MISAW dataset (Huault et al. (2021)) employed a similar formulation for anastomosis micro-surgeries. However, the use of triplets does not explicitly provide the location where each action takes place, which would allow for a more detailed understanding of surgical scenes.

Recently, the RARP45 (van Amsterdam et al. (2022)) and the HeiChole (Maier-Hein et al. (2021)) datasets introduced action recognition frameworks, approaching them as frame-wise recognition problems similar to that of JIGSAWS, but within the context of *in vivo* scenarios. RARP45 includes ten distinct actions on videos of Robot-Assisted Radical Prostatectomies. Similarly, HeiChole extends this approach to laparoscopic cholecystectomy with four possible categories. However, these annotations do not include spatial location information and offer a rather generalized understanding of actions.

Furthermore, Islam et al. (2020) introduced the localization of actions within surgical scenes in the Endovis 2018 dataset to enhance comprehension of the implicit relationships between instruments and tissues. The approach associated interaction categories with bounding boxes in Endovis 2018, designating the specific actions executed by each instrument or tissue. The dataset annotations used a graph structure, where each node represented an instrument or tissue, and the edges depicted the interactions between these nodes. Subsequently, the ESAD dataset (Bawa et al. (2021)) extended the localization of actions in robot-assisted surgery to Radical Prostatectomy data. Moreover, the AVOS dataset (Goodman et al. (2021)) expanded action localization to multiple surgery types. Nonetheless, these

datasets assign a single action category to each instrument and offer classes that could be further analyzed into even finer actions.

Contrary to previous approaches, our work adopts the Atomic Visual Actions (AVA) (Gu et al. (2018)) formulation for a more detailed study of temporal activities by employing atomic actions. As their name suggests, atomic actions are indivisible and represent the most fine-grained level of action understanding, thus allowing practical and precise activity modeling. Our GraSP dataset and its predecessor are pioneering in integrating the concept of atomic actions into the surgical domain. Accordingly, our benchmark deconstructs surgical activities into various atomic actions that surgical tools perform. As a result, GraSP presents a localized and multi-target atomic action detection task where each instrument independently performs multiple atomic actions simultaneously. This novel and highly challenging approach facilitates a more in-depth analysis of surgical actions and endorses applications across diverse surgery types, as it is a naturally transferable notion to any surgical domain.

2.4. Surgical Scene Understanding with Vision Transformers

Transformer models (Vaswani et al. (2017)) made a breakthrough in natural language processing, demonstrating their formidable capacity to process sequences by employing attention mechanisms across temporal dimensions. With the introduction of Vision Transformers (Dosovitskiy et al. (2021)), their application expanded to the realm of visual data processing. In recent years, Vision Transformers have gained significant prominence, showcasing their ability to utilize attention mechanisms to capture intricate and wide-ranging dependencies among diverse elements within an image. This ability translated to encouraging outcomes in image and video analysis (Carion et al. (2020); Fan et al. (2021); Zhu et al. (2021)).

This success has extended to the domain of endoscopic surgeries since previous works have successfully included transformers in their approach. For instance, in the domain of instrument classification, Kondo (2021) proposed a technique employing a CNN for feature extraction along with a temporal module based on Transformers, offering insights into a temporal window of features. In a distinctive approach, Nwoye et al. (2022) introduced a Transformer-inspired method for classifying triplets, incorporating a Convolutional Neural Network (CNN) backbone and attention mechanisms for enhanced feature mapping. Later, Sharma et al. (2023a) expanded on this model by incorporating a temporal consistency module, which fused features within a temporal window. Recently, Sharma et al. (2023b) proposed a triplet detection model, leveraging Deformable DETR (Zhu et al. (2021)) and a ResNet50 (He et al. (2016)) coupled with a transformer encoder for feature extraction. The methodology included incorporating a graph to process these features and understand interactions and a Multi-Head Attention layer applied to the nodes' features.

In phase recognition, Gao et al. (2021) utilized a CNN backbone for spatial feature extraction, coupled with temporal processing through a Temporal Convolutional Network (TCN) and refinement with Transformer layers. Similarly, Czempiel et al.

(2021) integrated a CNN backbone and Transformer layers, introducing a regularization parameter to focus attention on high-confidence features. Additionally, Ding and Li (2022) explored phases as temporal segments, employing a combination of CNN, temporal convolutions, and Transformers to achieve an enhanced capture of semantics and interrelations.

Addressing action localization, Zhang et al. (2022) compared models based on CNN, Transformers, and a hybrid approach. Superior results were achieved by integrating a CNN-based backbone with a BERT-based transformer network (Devlin et al. (2019)), showcasing enhanced temporal video understanding compared to ViT (Dosovitskiy et al. (2021)) for feature extraction.

Regarding the task of instrument segmentation, Zhao et al. (2022) pioneered a region classification approach, utilizing a modified MaskFormer (Cheng et al. (2021)) along with a CNN backbone. However, this model is limited in its comprehension of long-term surgical dynamics, relying solely on the previous frame for predictions in the current frame. Recently, Dhanakshirur et al. (2023) employed a Mask DINO (Li et al. (2023)) model with a ResNet50 (He et al. (2016)) backbone for instrument segmentation. The approach incorporated a transformer encoder to process the backbone features and implemented layers of various attention forms using the best queries predicted by Mask DINO to enhance the consistency and quality of region proposals.

However, these methodologies have not exploited the potential of transformers for a comprehensive understanding of surgical scenes, often relying on CNNs for feature extraction. Moreover, these approaches are designed for specific tasks rather than employing a general design that embraces the holistic nature of surgeries. Regarding these gaps, our previous works, Valderrama et al. (2022) and Ayobi et al. (2023), leveraged transformers for various tasks. These methods marked the introduction of architectures entirely based on Transformers, demonstrating satisfactory results in instrument detection, instrument segmentation, phase classification, and step classification tasks, achieving state-of-the-art performance. In this regard, our TAPIS model introduces a single method fully based on transformer architectures that can effectively tackle multiple surgical workflow analysis tasks within different levels of visual, temporal, and spatial understanding. Thus presenting a generalized state-of-the-art transformer model for multi-granular surgical scene understanding.

3. The Holistic and Multi-Granular Surgical Scene Understanding of Prostatectomies Dataset

We present the Holistic and Multi-Granular Surgical Scene Understanding of Prostatectomies (GraSP) benchmark. An Endoscopic Vision dataset comprised of 32 hours of Robot-Assisted Radical Prostatectomies annotated with a hierarchy of multiple long and short-term tasks, including the recognition of surgical phases and steps through time, the instance segmentation of surgical instruments present in a frame, and the detection of the atomic visual actions performed by those instruments. In this section, we explain the details of the dataset creation pro-

Table 2: **Category sets for all the presented tasks in GraSP.** We present the defined sets of semantic categories for each proposed task in our GraSP dataset. We showcase the ID number and the defined label name for each phase, step, instrument, or atomic action category.

| Phases Categories | | Steps Categories | | | Atomic Action Categories | | | |
|-------------------|---|------------------------------|--|--|--|----|--------------------------|---------|
| 0 | Idle. | 0 | Idle. | 10 | Cut the tissue between the prostate and the urethra. | 1 | Cauterize | |
| 1 | Left pelvic isolated lymphadenectomy. | 1 | Identification and dissection of the Iliac vein and artery. | 11 | Hold prostate. | 2 | Close | |
| 2 | Right pelvic isolated lymphadenectomy. | 2 | Cutting and dissection of the external iliac vein's lymph node. | 12 | Insert prostate in retrieval bag. | 3 | Cut | |
| 3 | Developing the Space of Retzius. | 3 | Obturator nerve and vessel path identification, dissection and cutting of the obturator lymph nodes. | 13 | Pass suture to the urethra. | 4 | Grasp | |
| 4 | Ligation of the deep dorsal venous complex. | 4 | Insert the lymph nodes in retrieval bags. | 14 | Pass suture to the bladder neck. | 5 | Hold | |
| 5 | Bladder neck identification and transection. | 5 | Prevesical dissection. | 15 | Pull suture. | 6 | Open | |
| 6 | Seminal vesicle dissection. | 6 | Ligation of the dorsal venous complex. | 16 | Tie suture. | 7 | Open Something | |
| 7 | Development of the plane between the prostate and rectum. | 7 | Prostate dissection until the levator ani. | 17 | Suction. | 8 | Pull | |
| 8 | Prostatic pedicle control. | 8 | Seminal vesicle dissection. | 18 | Cut suture or tissue. | 9 | Push | |
| 9 | Severing of the prostate from the urethra. | 9 | Dissection of Denonvilliers' fascia. | 19 | Cut between the prostate and bladder neck. | 10 | Release | |
| 10 | Bladder neck reconstruction. | | | 20 | Vascular pedicle control. | 11 | Still | |
| | | Instrument Categories | | | | | 12 | Suction |
| 1 | Bipolar Forceps (BF) | 4 | Monopolar Curved Scissors (MCS) | Laparoscopic Instrument (LI): [Laparoscopic Retraction Forceps, Laparoscopic Suture Scissors, Laparoscopic Needle Holder] | | 13 | Travel | |
| 2 | Prograsp Forceps (PF) | 5 | Suction Instrument (SI) | | | 14 | Other: [Staple, Wash] | |
| 3 | Large Needle Driver (LND) | 6 | Clip Applier (CA) | | | | | |

cess, including data collection, annotation, and curation, and we analyze the main statistics of our dataset.

3.1. Data Collection

The data acquisition process involved recording the surgical procedures of patients undergoing Robotic-Assisted Laparoscopic Radical Prostatectomy at Fundación Santa Fé de Bogotá, with explicit consent obtained for using these visual materials from the respective patients. We did all the data collection protocols under the approval of the ethics committees of all institutions directly involved in this work.

The surgical team utilized an endoscopic camera to capture recordings, generating a 2D image signal of the left view of the endoscope, which they subsequently extracted through an HDMI cable connected to a KARL STORZ (AIDA mini WD 100) high-definition video capture device. This device facilitated real-time storage of procedural information, providing imagery at 720 dots per inch (dpi) and ensuring robust data storage onto an external hard disk. We anonymized all the data collected according to our ethical protocols.

Three highly experienced surgeons performed the surgeries using a da Vinci Si 3000 robot manufactured by Intuitive Inc. (Sunnyvale, California). The equipment included the robot assembled with a high-definition video camera, providing independent viewing for each eye. The team placed the Monopolar Energy Scissors (Monopolar Curved Scissors) in port #1 (right hand). At the same time, they located the Bipolar Energy Forceps (Bipolar Forceps), capable of being fenestrated or configured as Maryland Forceps, in port #2. The third port accommodated a Prograsp Retraction Forceps (Prograsp Forceps).

For the reconstructive stages of the surgery, surgeons removed the previous instruments located in ports #1 and #2 and positioned two robotic Needle Holders (Large Needle Drivers). Additionally, the surgical setup designated two ports for the bedside assistant. One port housed a Laparoscopic Suction cannula (Suction Instrument), and the other contained either a Laparoscopic Intestinal Retraction Forceps, a Laparoscopic Needle Holder, Laparoscopic Scissors designed explicitly for cutting suture material (Laparoscopic Instruments), or a Clip Applier with Plastic Hemostatic clips of the HEM-O-LOCK type.

3.2. Annotation Process

We classify phases and steps as long-term reasoning tasks, following the temporal breakdown outlined in Hualmé et al.

(2021). Phases represent the fundamental segments of surgical procedures, including key stages like preparation, organ manipulation, and anatomical reconstruction. Meanwhile, steps provide a more detailed breakdown within these phases, focusing on specific surgical activities and maneuvers, such as dissecting anatomical landmarks, making incisions, pulling sutures, and packing dissected structures. In the following subsection, we explain the process of defining phases and step categories.

Conversely, our approach for localized atomic action recognition and surgical instrument segmentation focuses on short-term reasoning tasks. On the one hand, this facet includes identifying localized atomic actions within RARP procedures based on the atomic action definition of AVA (Gu et al. (2018)). Our medical experts stated a set of surgical atomic actions based on the most detailed and singular actions that could be performed in surgery by instruments, such as pull, push, and hold, among others. Table 2 displays the final defined set of atomic action categories on the right side. On the other hand, surgical instrument segmentation involves precisely delineating and identifying surgical tools within the scene. We defined Surgical Instrument classes based on the da Vinci Robot user manual and catalog (Intuitive Inc. (2014, 2023)) and the instrument setup used during data collection (Section 3.1). We showcase the final set of surgical instrument categories in Table 2. By categorizing these aspects as short-term reasoning tasks, our dataset represents both the general and detailed facets of the RARP procedure, enabling a multi-level holistic understanding of surgical scenes in varying degrees of granularity. Due to the time-consuming nature of short-term task annotations and considering our resource constraints, we only annotated a subset of keyframes uniformly sampled through time with a fixed temporal stride, as explained in upcoming Subsections 3.2.2 and 3.2.3.

3.2.1. Phase and Step Tasks Annotation

The delineation of phases, steps, and their corresponding nomenclature adhered closely to the procedural framework of radical prostatectomy coupled with bilateral extended lymphadenectomy. This categorization gained validation through the comprehensive insights outlined in the 12th edition of Campbell-Walsh Urology (Partin et al. (2020)). Within this framework, defining surgical phases involved recognizing distinctive stages within the surgical process, each occurring singularly and without repetition. In contrast, surgical steps re-

fer to specific acts undertaken during the surgical process, often occurring multiple times. The aggregation of multiple steps formed a phase and the determination of the number of phases correlated with the sequential execution of surgical steps.

We then established the sequencing and hierarchy of phases based on standardized steps intrinsic to Robot-Assisted Radical Prostatectomy, a procedural protocol routinely practiced at Fundación Santa Fé de Bogotá. Subsequently, our surgical team reviewed the initial version of the phases and steps categories and hierarchies, involving scrutiny by two experienced urologists with specialized proficiency in Robotic-Assisted Surgery. This collaborative evaluation facilitated the refinement of the defined phases and steps, ensuring alignment with the intricate aspects of the surgical technique. The final set of phases and steps categories is portrayed in Table 2, and the hierarchical structure of phases and steps is visually represented in Figure B.2 in the Supplementary Material.

After establishing the labels and hierarchies of the long-term tasks, we conducted an annotation procedure that involved a team of two urologist residents specializing in transperitoneal radical prostatectomy surgeries. The annotation team independently annotated each surgical video, defining specific timestamps for the start and end times of phases and step intervals down to the hour, minute, and second, resulting in two annotations per video. In the case of the eight previously annotated surgeries, these were annotated by the team once more, resulting in two sets of annotations per surgery as well. When discrepancies arose between the annotations, the resident annotators collectively reviewed and reconciled differences to establish a consensus regarding the definitive delineation of phases and steps.

3.2.2. Surgical Instrument Segmentation

We undertook an annotation process for surgical instrument segmentation that prioritizes dataset consistency, following a structured sequence of steps: (1) frame selection, (2) annotation of surgical instrument masks in the selected frames, (3) and a methodical and iterative validation phase aimed at rectifying errors.

Firstly, we selected frames at 35-second intervals within the surgical videos. This selection aimed to maintain a balanced, uniform representation across categories while considering computational and annotation resource constraints. Secondly, we trained a team of 17 annotators based on an expert-designed and highly specific protocol to maintain annotation quality and consistency across surgical instrument annotations. Employing both Label-Studio (Tkachenko et al. (2020-2022)) and Toronto Annotation Suite (Kar et al. (2021)) open-source annotation platforms, annotators delineated instrument masks and labeled them with one of the predefined instrument subtype categories. Annotators defined instrument regions either by refining predicted masks semi-automatedly or directly without initial mask predictions. We obtained initial surgical instrument mask predictions using MATIS (Ayobi et al. (2023)), a previous work of ours trained in Endovis 2017 (Allan et al. (2019)) and Endovis 2018 (Allan et al. (2020)). For surgeries in our dataset that already had bounding boxes established for

the Instrument Detection task in the earlier version (Valderrama et al. (2022)), we provided these boxes to the annotation team. Their tasks were to refine these bounding boxes into segmentation masks, verify the adequate classification of instruments, and look for possibly missing hidden instances. It is noteworthy to add that we ensured consistent annotation conditions among all annotators to mitigate potential biases in the dataset. Similarly, as an aid for instrument instance identification, all annotators had access to 3-second clips centered on each assigned keyframe along with all the surgical videos corresponding to their assigned keyframes.

Thirdly, we followed a three-staged validation phase. In the first stage, four experts in surgical data science reviewed all segmentation masks to identify any errors, such as missing instrument masks, misclassifications, or delineation errors. These experts accurately described these errors to send these instances back to the annotation team for corrections. In the second stage, the annotation team re-annotated instances with identified errors to ensure rectification. Finally, as a third stage following the re-annotation process, the surgical data science experts conducted a second review of the entire dataset, correcting the remaining annotation errors themselves and ensuring further validation. It is important to note that despite utilizing predefined masks in one of the platforms, the experts in surgical data science ascertained that its presence did not impact the quality of annotations.

3.2.3. Atomic Action Recognition

The annotation process for atomic action recognition involved the team of four experts in surgical data science trained explicitly for this task with the guidance of the surgeons team, following a detailed annotation protocol designed by domain experts. The annotation process consisted of three main stages: (1) Estimation of instrument location with bounding boxes and labeling of atomic actions, (2) Spatial refinement and validation by retrieving bounding boxes from the previously precisely annotated segmentation masks, and (3) Annotation consensus and rectification between independent annotators and guidance of experienced surgeons.

We underwent this process using the open-source Toronto Annotation Suite (Kar et al. (2021)) platform to annotate the same previously selected frames for surgical instrument segmentation. Since atomic action labeling explicitly requires temporal context, annotators defined atomic actions based on the 3-second clips centered on the frame of interest as initially done in AVA (Gu et al. (2018)). However, annotators could also access all of the surgical footage when necessary. Hence, the annotators first localized instruments with bounding boxes regardless of the instrument segmentation annotation process. After defining surgical instruments' spatial locations with bounding boxes, annotators identified and labeled combinations of maximum 3 atomic actions, treating them as discrete states that instruments could simultaneously undertake based on the predefined set of atomic action categories (Table 2).

Subsequently, we spatially aligned the bounding boxes generated from the atomic action labeling with those obtained from instrument segmentation mask annotations. Hence, we kept the

Table 3: **Distribution of the number of frames on each defined dataset split.** The Table presents the duration in seconds and the number of frames sampled at 1fps of each collected Case in our dataset. Each Case corresponds to an entire surgery performed. We also show our predefined dataset partition into Fold 1 and Fold 2 for two-fold cross-validation and a Test set for final model testing.

| Set | Case No. | Duration (h) | Frames (1fps) |
|--------------|----------|--------------|---------------|
| Fold 1 | 001 | 3.05 | 10972 |
| | 004 | 2.36 | 8490 |
| | 014 | 2.77 | 9973 |
| | 015 | 2.48 | 8969 |
| Fold 2 | 002 | 2.62 | 9443 |
| | 003 | 1.63 | 5882 |
| | 007 | 2.23 | 8018 |
| | 021 | 3.30 | 11871 |
| Test | 041 | 2.63 | 9452 |
| | 047 | 1.81 | 6504 |
| | 050 | 3.86 | 13899 |
| | 051 | 0.69 | 2496 |
| | 053 | 2.93 | 10552 |
| Total | 13 | 32.37 | 116521 |

refined bounding boxes derived from segmentation masks to locate atomic actions. This simultaneous annotation procedure allowed a further validation of instrument localization annotations by comparing the outcomes between separate groups of annotators. The surgical data science experts carefully revised cases with considerable discrepancies between the annotated instrument segments and instrument bounding boxes for atomic actions.

The labeling of atomic actions for each instrument was performed in parallel by three different annotators. In the case of the eight previously annotated surgeries, the team re-annotated these two times more, also resulting in three sets of annotations per instrument. Consequently, each instrument in the dataset had three sets of atomic action combinations. To reduce biases and ensure robustness in our annotations, we retained individual atomic action categories labeled by at least two annotators (present in at least two of the three sets) as the final atomic action annotations. For instrument instances where the intersection of at least two sets over the union of the three sets was lower than 0.3, the team collectively reviewed and deliberated upon them to establish a final set of atomic actions.

Additionally, we constructed theoretical co-occurrence matrices under the guidance of our experienced surgeons to establish valid presence relationships among the different atomic actions and between actions and instruments (Figure C.11 of the Supplementary Material). These matrices ensured logical consistency in actions performed simultaneously by an instrument and verified correlations between specific actions executed by their annotated instrument type. We applied these matrixes to validate the annotated combinations of atomic actions, ensuring compatibility within sets of actions. In cases where conflicting atomic actions arose, or actions were incompatible with the corresponding instrument, the team collectively reviewed and deliberated to establish consensus for re-annotation.

3.3. Dataset Statistics

Our GraSP dataset comprises thirteen (13) Robot-Assisted Radical Prostatectomy videos captured at a frame rate of 30 frames per second (fps). These surgical videos account for 32.37 hours, with an average duration of 2.49 hours and a standard deviation of 0.77 hours. For benchmarking purposes, we define a two-fold cross-validation setup for training and validation and establish a test set for final performance evaluation. Table 3 presents the data splits and the duration and number of frames (sampled at 1fps) for each video in the GraSP dataset. The original videos of the PSI-AVA dataset with curated annotations make the defined cross-validation set, and the test set comprises the five new videos included in this work.

Figure 1 portrays an overview of our proposed tasks and annotations, and Table 2 presents our sets of semantic categories. The final ground truth annotations of GraSP comprise eleven (11) surgical phase categories, twenty-one (21) surgical steps, seven (7) instrument categories, and fourteen (14) atomic action categories. Therefore, our GraSP dataset proposes diverse classes for each task, integrating local and temporal visual understanding of surgeries. The hierarchical dendrogram of Figure B.2 of the Supplementary Material represents the relations between each phase and its nested steps, and it also includes the labels and names of all the categories (IDs) for each task in the GraSP dataset.

Figures 2 and 3 illustrate the distribution of the percentage of annotated frames (counted at 1fps) for each phase and step class, respectively. We also present transition matrices of the annotated categories and visualizations of the temporal progression of phases and steps in Figures C.5, C.6, C.7, and C.9 of the Supplementary Material. The frequency distribution of the long-term annotations for a particular class is highly influenced by the occurrence rate of a specific phase or step and the average duration of each occurrence. Notably, these distributions reveal a pronounced long-tail effect, indicating that some phase and step categories are significantly more prevalent than others. For instance, the *Idle* class is over-represented in the annotations of phases and steps compared to other categories. The transition matrices and temporal visualizations explain this trend, as they demonstrate that most phases and steps frequently transition from or to an *Idle* state. This tendency is typical and representative of Radical Prostatectomies, as surgeons pause between stages to change instruments, evacuate waste, clean and relocate the endoscope, or rest due to the complexity and duration of the procedures.

In addition, for Phase and Step annotations, we present the duration distribution of each continuous temporal segment for each phase and step category in seconds. We display the phase duration distribution in Figure 4 and the step duration distribution in Figure 5. These distributions and the visualizations in Figures C.7 and C.9 of the Supplementary Material underscore these tasks' granularity and complexity differences. On the one hand, phases represent broader surgery segments, usually occurring once (though interrupted by *Idle* segments) and covering more general aspects of the procedure. Thus, they constitute a coarser level of understanding and exhibit longer average durations, with some continuous segments lasting over 20 min-

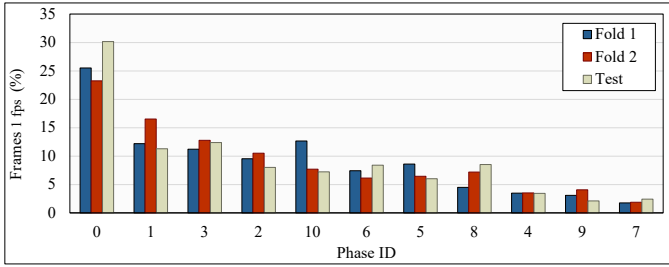


Fig. 2: **Distribution of the percentage of frames per surgical phase category on each data split.** We count the number of frames sampled at 1fps. We organize the graphic in descending order and present correspondence between phase IDs and phase labels in Table 2. The figure is best viewed in color.

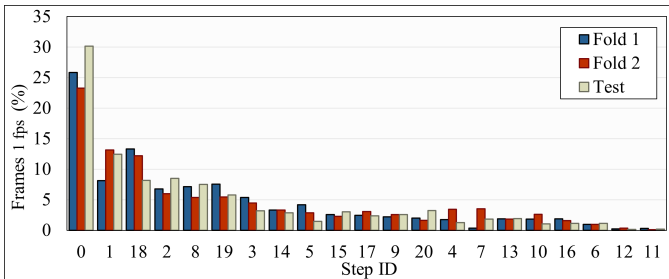


Fig. 3: **Distribution of the percentage of frames per surgical step category on each data split.** We count the number of frames sampled at 1fps. We organize the graphic in descending order and present correspondence between step IDs and step labels in Table 2. The figure is best viewed in color.

utes. On the other hand, steps recur in shorter segments repetitively, representing more specific parts of the surgery. Hence, step segments present shorter average durations, with the most extended segments spanning around 11 minutes, indicating a finer-grained level of detail.

Moreover, Figures 4 and 5 denote different intra-class duration variability across all phase and step categories with multiple outliers in most categories. Intuitively, categories with larger average durations exhibit more variability in segment length. For example, step categories such as *Identification and Dissection of the iliac vein and artery* (1), *Cutting and dissection of the external iliac vein's Lymph Node* (2), *Ligation of the dorsal venous complex* (6), or *Cut between the prostate and bladder neck* (19) present larger duration times and variabilities as they mainly involve dissection or cutting of blood vessels or tissues and bleeding control, which demand more time, may vary among patients and often require the alternation with other steps. In contrast, categories like *Pass suture to the urethra* (13), *Pass suture to the bladder neck* (14), *Pull suture* (15), or *Tie suture* (16), show lower durations and variability as they are related to the suturing process which is usually performed within faster and more standardized time windows.

Similar patterns are evident in phase categories where the categories with the highest average duration and variabilities are *Left and Right pelvic isolated lymphadenectomy* (1 and 2, respectively) and *Bladder neck identification and transection* (5), which regard tissue cutting and remotion. Conversely, the least durable and variable categories are *Prostatic pedicle control* (8) and *Bladder neck reconstruction* (10), mostly related to suturing and clipping procedures but also significantly affected by a

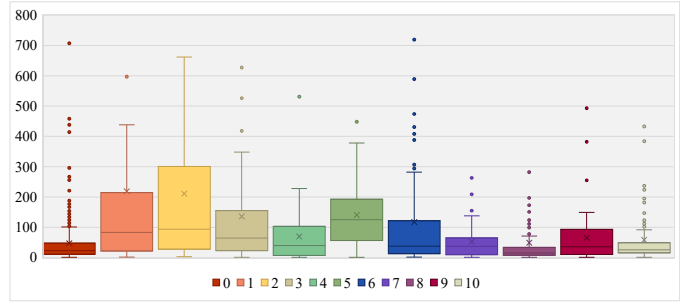


Fig. 4: **Boxplot distribution of the duration of each phase category.** Each boxplot presents the distribution in seconds of the period of all the present temporal windows corresponding to each phase category in our dataset. We clipped this figure to a maximum of 800 seconds for better visualization; the entire figure is presented in the Supplementary Material. The figure is best viewed in color.

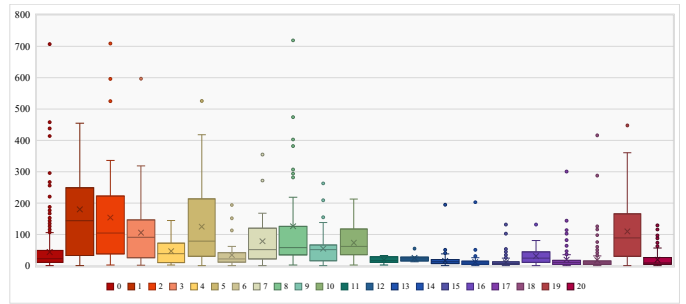


Fig. 5: **Boxplot distribution of the duration of each step category.** Each boxplot presents the distribution in seconds of the period of all the present temporal windows corresponding to each step category in our dataset. We clipped this figure to a maximum of 800 seconds for better visualization; the entire figure is presented in the Supplementary Material. The figure is best viewed in color.

consistent interruption by *Idle* stages. This tendency similarity highlights the complementary relation between phase and step recognition tasks.

In this way, the observed statistical distributions of our long-term annotations, like the long-tail distribution in frame frequency and the significant inter- and intra-class variability in our phases and steps' duration, present considerable challenges within our benchmark. Nevertheless, it is evident that these distributions accurately represent the realities of surgical scenarios, thus emphasizing the value of utilizing human *in vivo* data sources and demonstrating the complexities involved in visually understanding surgical scenes.

Furthermore, Figure 6 and Table C.3 (Supplementary Material) display the frequency distribution of the instrument instances per class, also demonstrating a natural long-tail effect. The reason for this distribution can also be observed in the co-occurrence matrices detailed in the Supplementary Material. The Monopolar Curved Scissors (MCS) and Bipolar Forceps (BF) are the most frequent instruments. This overrepresentation is primarily because these tools are the most actively used in robot-assisted surgeries, owing to their versatility and capacity to perform most surgical actions. They are also among the most crucial robotic instruments of the da Vinci Surgical System (dVSS). Following these, the Large Needle Driver (LND), another typical robotic instrument of the dVSS, also

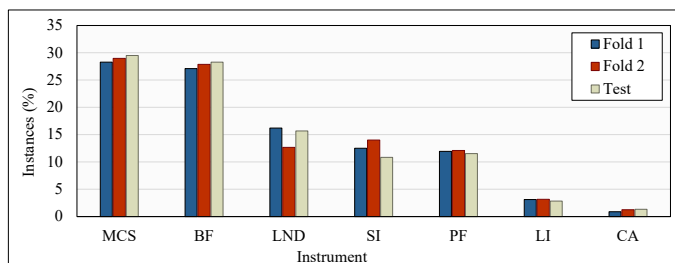


Fig. 6: **Distribution of the percentage of instrument instances per instrument type category on each data split.** We organize the graphic in descending order. The instrument categories are Monopolar Curved Scissors (MCS), Bipolar Forceps (BF), Large Needle Driver (LND), Suction Instrument (SI), Prograsp Forceps (PF), Laparoscopic Instrument (LI) and Clip Applier (CA). The figure is best viewed in color.

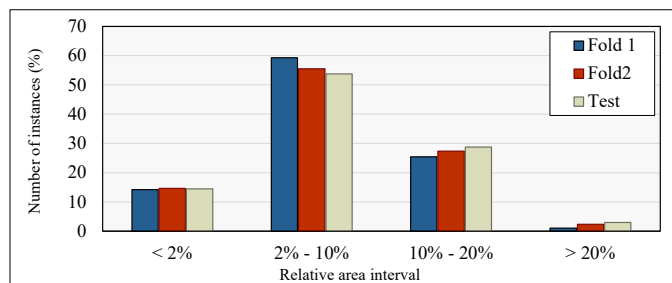


Fig. 8: **Distribution of the percentage of annotated segments per segment relative area interval on each data split.** The relative area of an annotated segment corresponds to the fraction of the image it occupies. The figure is best viewed in color.

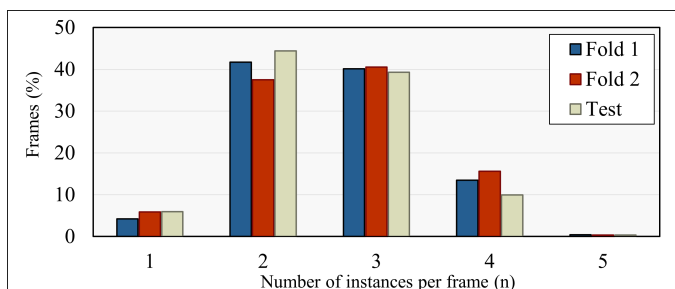


Fig. 7: **Distribution of the percentage of frames presenting (n) instrument instances per frame on each data split.** The percentage of frames at 35 fps that have (n) instrument instances in it. The figure is best viewed in color.

presents high frequencies as it is utilized for all suturing stages, but it has reduced functionalities compared to the MCS and BF. While also commonly used, the Prograsp Forceps (PF) and the Suction Instrument (SI) have more specific roles in surgery and often function passively and steadily. The latter is additional to the dVSS. Finally, instruments like the Clip Applier (CA) and other Laparoscopic Instruments (LI) are also additional to the dVSS and employed for specific purposes during certain stages of the surgery.

Figure 7 and Table C.4 (Supplementary Material) illustrate the distribution of the number of instrument instances per video frame. We observe that each video frame contains 1 to 5 instrument instances (2.23 average of instrument instances per frame), with approximately 80% of frames containing between 2 and 3 instances. These statistics are characteristic of robotic surgeries, where surgeons mainly use two robotic instruments simultaneously with their hands. The additional presence of non-robotic instruments (SI, LI, and CA) manipulated by an assistant or a third robotic instrument left stationary increases the possible number of instances per frame and contributes to the diversity in surgical visual scenes. Situations involving four or five instruments are less common and usually indicate specific complex scenarios within the surgery. The upper limit of five instruments per frame is due to the inherent limitations of the dVSS and the specific complexities associated with Radical Prostatectomies.

Figure 8 displays the dataset’s relative area distribution of instrument instances. Our instrument instances’ relative sizes range from 0.02% to 40.4%, with an average relative size of

7.5% and most instruments occupying between 2 and 10% of the video frames. This variation in relative size stems from factors such as the proximity of the instruments to the endoscope or the portion of the instrument that is visible. In this regard, a prominent challenge of our instrument segmentation benchmark is the significant number of small segments, with more than 10% of instrument instances corresponding to segments with less than a 2% relative area. Smaller instances typically result from instruments being distant from the camera, partial occlusion, or most of the instrument body being out of the camera’s field of view. One notable improvement in our GraSP dataset over the PSI-AVA benchmark is the inclusion of more instrument instances with minimal areas. This enhancement is a direct result of our meticulous data curation process.

Finally, Figure 9 and Table C.5 (Supplementary Material) present the frequency and normalized distribution of the atomic action instances per class. Again, the distribution of atomic actions suggests a long-tail behavior where *still* (11), *hold* (5), and *travel* (13) are the most frequently occurring actions in the dataset. Indeed, during the surgery, most instruments are either used to hold and maintain tissues and objects in place or to move these tissues and objects to a different location. Later on, *Push* (9) and *Pull* (8) represent more specialized movements and thus are less present. *Suction* (12) is an action that can only be performed by the SI (as shown in the instrument-action co-occurrence matrix in Figure C.14 in the Supplementary Material). Nonetheless, when on the frame, the SI very frequently performs this action, which explains the higher frequency of this action. The remaining actions present lower frequencies as they are much more specialized and usually done by a specific type of instrument in shorter time frames. For instance, *Cauterize* (1) can only be performed by the BF and MCS, and *Cut* (3) is only performed by the MCS. Similarly, *Open* (6) can be done by all the instruments with tips (all except SI) but for very short durations. Lastly, the *Other* class (14) is the most scarce category since it is a composition of *Staple* and *Wash*, which can only be performed by the CA and the SI, respectively, and only happen in very particular moments of the surgery.

The statistical distributions presented in Figures 2, 3, 6, 7, 8 and 9 demonstrate that our dataset maintains similar distributions across all the predefined dataset splits. First, this consistency highlights the reliability of our entire dataset and its predefined cross-validation folds and test set, showing that all the

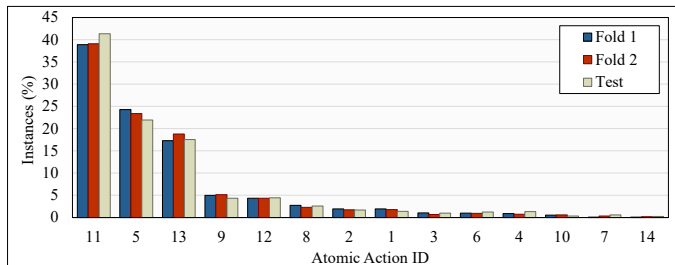


Fig. 9: **Distribution of the percentage of instances per atomic action category on each data split.** We consider each annotated action within an instrument instance an independent atomic action instance. We organize the graphic in descending order and present the correspondence between atomic action IDs and atomic action labels in Table 2. The figure is best viewed in color.

categories in all the proposed tasks keep comparable frequency distributions in all splits. Second, this observation validates our annotation process as it proves the efficiency of our designed annotation protocols and our multiple stages of data validation and correction.

We include further statistical analysis in Appendix C of the Supplementary Material. This section provides information about the total number of instances in each task of the GraSP dataset, the transition probabilities for both phase and steps, the intra-task categories co-occurrences for the instruments and actions tasks, and the detailed inter-task categories co-occurrences for instruments-phases, instrument-steps, and instruments-actions in GraSP. Our previously presented statistics and the additional statistics in the Supplementary Material prove the intrinsic complementarity among the proposed tasks in GraSP. We previously established the relation between phases as steps where their per-class frequency and duration distributions demonstrated similar patterns related to the semantic meaning of the categories. Regarding this, the most durable phase categories encompass many of the most durable step categories, and the least durable phases encompass many short steps. Likewise, there is a clear relation between the surgical instrument and action categories, where many actions can be performed only by specific instruments. Thus, the frequency of different instruments affects the frequencies of actions. Additionally, the co-occurrence matrixes demonstrate an evident correspondence between instruments and phases or steps as, intuitively, different instruments are more present or completely absent in different phases and steps.

3.4. Evaluation Metrics

To evaluate the performance of phase and step recognition, we keep the originally proposed metric in Valderrama et al. (2022): the mean Average Precision (mAP) per frame. We chose this metric as it is a standard and robust metric commonly used for frame-wise evaluation of action recognition (Caba Heilbron et al. (2015)). We use the implementation of Python’s Scikit-learn library³ for the calculation of this metric.

Regarding the instrument segmentation task, we adopt the conventional instance-based mean Average Precision (mAP)

from PASCAL VOC (Everingham et al. (2015)) to exploit the instance-wise nature of this task entirely. Following Everingham et al. (2015), we adopt the $mAP@0.5IoU_{segm}$ metric, which uses a minimum Intersection over Union (IoU) threshold of 50% between the ground-truth masks and the predicted masks to categorize predictions into true positive predictions. We hope that including the $mAP@0.5IoU_{segm}$ will encourage the community to approach the surgical instrument segmentation problem from a similar evaluation perspective. We calculate the $mAP@0.5IoU_{segm}$ metric using a modification of Activity Net’s (Caba Heilbron et al. (2015)) implementation⁴.

Additionally, we maintain the usual semantic segmentation evaluation metrics we introduced in González et al. (2020). These metrics include the Mean Intersection over Union (mIoU), Intersection over Union (IoU), and Mean Class Intersection over Union (mcIoU). We kept these metrics as they are highly stringent metrics that have been the standard evaluation methodology for the instrument segmentation task in multiple works. We utilize the implementation provided in Ayobi et al. (2023)⁵.

Lastly, for the Atomic Action Detection task, we adhere to the original evaluation framework from AVA (Gu et al. (2018); Li et al. (2020)) and Activity Net (Caba Heilbron et al. (2015)), which is, in turn, based on PASCAL VOC’s object detection evaluation (Everingham et al. (2015)). As previously stated, the atomic actions in our framework are performed by an instrument and, as such, are centered on it. Thus, locating surgical atomic visual actions consists of locating the acting instrument that performs the actions. However, the primary objective is to accurately detect the presence and location of these actions rather than delineating the exact shape of the agent that executes them. Hence, an object detection approach is better than an object segmentation approach for the atomic action location task.

For this reason, regardless of our instrument segmentation annotations, we maintain the original $mAP@0.5IoU_{box}$ metric from AVA, which is analogous to the previously explained $mAP@0.5IoU_{segm}$ metric but using the ground truth and predicted bounding boxes to calculate the IoU. Finally, due to the multi-target fashion of atomic action detection, where each instrument instance can perform up to three actions, we independently evaluate the presence of each atomic action in an instrument instance instead of assessing whether the entire expected combination of ground truth actions was predicted. This methodology is a more robust and sensitive way of measuring the atomic action detection performance. Once again, we use Activity Net’s implementation of the $mAP@0.5IoU_{box}$ metric for atomic visual actions detection.

4. Transformers for Actions, Phases, Steps and Instrument Segmentation

We propose the Transformers for Actions, Phases, Steps, and Instrument Segmentation (TAPIS) model, a generalized archi-

³sklearn.metrics.average_precision_score

⁴<https://github.com/activitynet/ActivityNet>

⁵<https://github.com/BCV-Uniandes/MATIS>

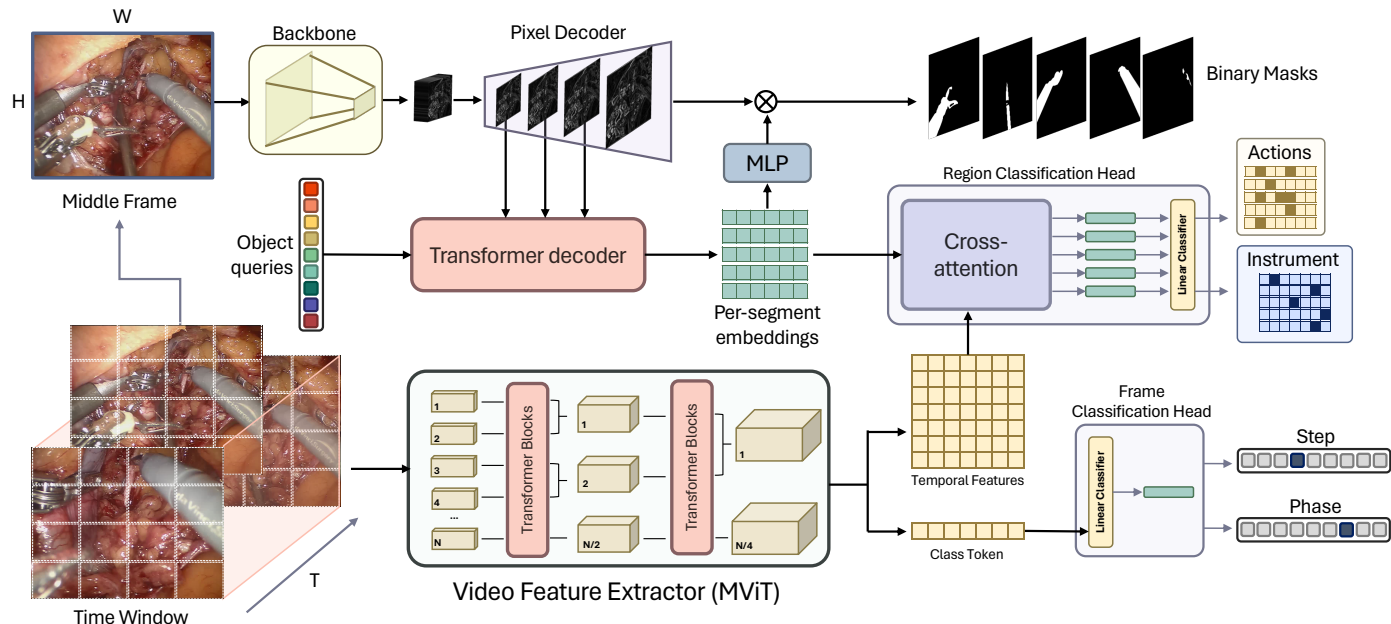


Fig. 10: **TAPIS** utilizes Mask2Former (Cheng et al. (2022)) as its instrument segmentation baseline and MViT (Fan et al. (2021)) as its video feature extractor. On the one hand, the segmentation baseline takes an input frame and computes a set of per-segment embeddings by cross-attending learnable object queries with multi-scale features extracted with a visual backbone and processed with a pixel decoder. Then, the model generates a set of binary masks with the dot multiplication between the linearly transformed per-segment embedding with pixel features from a pixel decoder. On the other, the video feature extractor uses a time window centered on the keyframe used for segmentation and computes a sequence of spatio-temporal embeddings by patchifying the input video and applying multiple stages made by blocks of Multi Head Pooling Attention. These stages progressively reduce the sequence length and increase the number of features. For the long-term tasks, the *frame classification head* linearly classifies the learnable class token of the video feature extractor into either a phase or a step category. For the short-term tasks, a region classification head cross-attends the precalculated segment embeddings from the instrument segmentation with the spatio-temporal features, and then they are linearly classified into instruments or action classes. The figure is best viewed in color.

ecture designed to tackle all the proposed tasks in the GraSP benchmark. Figure 10 portrays the general architecture of TAPIS. Our method utilizes a localized instrument segmentation baseline applied on independent keyframes that acts as a region proposal network and provides pixel-precise instrument masks and their corresponding segment embeddings. Further, our model uses a global video feature extractor on time windows centered on a keyframe to compute a class embedding and a sequence of spatio-temporal embeddings. A *frame classification head* uses the class embedding to classify the middle frame of the time window into a phase or a step, and a *region classification head* interrelates the global spatio-temporal features with the localized region embeddings for atomic action prediction or instrument region classification. In the following subsections, we explain the details of our proposed architecture.

4.1. Instrument Segmentation Baseline

We follow MATIS (Ayobi et al. (2023)), our previous approach for the instrument segmentation task, which adapts our winning solution of the SAR-RARP50 challenge⁶. Hence, we employ Mask2Former (Cheng et al. (2022)) as our primary instrument segmentation baseline and region proposal method. We select this method as it is highly efficient and has demonstrated excellent performance in instance segmentation of natu-

ral and robot-assisted surgery images. In this section, we briefly review Mask2Former’s methodologies.

The general intuition behind Mask2Former is to generate a fixed set of \mathcal{N} binary instance masks with their corresponding class probability distribution. For this purpose, Mask2Former adapts DETR’s (Carion et al. (2020)) and MaskFormer’s (Cheng et al. (2021)) meta architectures based on processing a set of \mathcal{N} learnable object queries into \mathcal{N} per-segment embedding by using a transformer decoder that cross-attends the learnable object queries with the image features extracted from the backbone. However, Mask2Former utilizes a Multi-Scale Deformable Attention (Zhu et al. (2021)) pixel decoder with upsampling layers to compute multi-scale per pixel features to feed as image features for the transformer decoder. Also, it replaces the conventional global cross-attention with masked attention, which employs binary masks generated from the pixel embeddings and the transformed object queries to restrict attention and focus on relevant regions. These enhancements significantly increase training efficiency and boost segmentation performance. Finally, a linear classifier projects each outputted segment embedding into a class probability, and simultaneously, a multi-layer perceptron (MLP) transforms the segment embeddings into mask embeddings to generate the final binary masks by the dot multiplication with the per-pixel features. Figure 10 displays this methodology at the top.

We refer the reader to the original Mask2Former (Cheng et al. (2022)) and MATIS (Ayobi et al. (2023)) papers for further details on the Mask2Former architecture and its adaptation

⁶synapse.sar-rarp50.challenge

for surgical instrument segmentation. Furthermore, our TAPIS model utilizes Mask2Former’s region proposals two-fold. First, as in MATIS, to improve temporal consistency in instrument segmentation by reclassifying region proposals utilizing temporal context provided by a video feature extractor. Second, to handle the implicit need for instrument localization in atomic action detection. Thereby, TAPIS uses the corresponding segment embeddings of the proposed regions as inputs for a *region classification head* that enhances the segment classification process or predicts the atomic actions performed by the proposed instruments. We provide further insights about our *region classification module* in Section 4.3.

4.2. Video Feature Extractor

Following our previous work, we employ MViT (Fan et al. (2021)) as our video feature extractor to capture intricate details across various space-time scales by leveraging transformers. Once again, we briefly review MViT and refer the reader to the original paper for further details (Fan et al. (2021)).

MViT, an extension of ViT Dosovitskiy et al. (2021) for video-level recognition, is based on consecutive *stages* of multiple transformer blocks. This architecture first partitions the image into overlapping patches, and then, through each stage, it contracts the spatio-temporal dimensions (sequence length/resolution) while the channel dimensions (features length) expand. To achieve this, MViT replaces the Multi-Head Attention employed in ViT with Multi-Head Pooling Attention (MHPA). This adaptation involves pooling the queries, keys, and values at the beginning of each stage to reduce the spatio-temporal resolution before computing attention. Additionally, MViT uses linear projections at the end of each stage to increase the channel dimension for the following stages. This process creates a feature pyramid network, with the initial stages operating at more detailed resolutions and minor features and the final stages processing shorter sequences with more complex spatio-temporal features. Additionally, MViT follows BERT’s (Devlin et al. (2019)) and ViT’s (Dosovitskiy et al. (2021)) methodology of including a learnable class token that acts as a single embedding of the entire sequence for classification tasks.

We utilize the classification nature of MViT for phases and steps recognition by classifying an entire time window centered on a keyframe with the class of the middle frame. For this purpose, we use a *frame classification head* that employs a linear classifier on the output class token of the video features extractor to derive the final Phase or Step class probability distribution. Figure 4.4 portrays the video feature extractor and the *frame classification head* at the bottom. The following section extends how we use the remaining embeddings for region classification and action recognition.

4.3. Region Classification Head

We introduce a novel *region classification head* for instrument classification and atomic action detection. Our *region classification head* builds upon the box classification head proposed in Valderrama et al. (2022), which mainly combines pre-calculated region features from a frame-wise box proposal network with the sequence of temporal features generated by the

video feature extractor. In this work, we leverage transformers’ cross-attention to correlate region and temporal features. For this purpose, we input the per-segment embeddings of the proposed regions into a cross-attention layer that performs Multi-Head Attention over the entire sequence of spatio-temporal features from the video feature extractor. Consequently, this layer can fully exploit the spatio-temporal resolution to enrich the region features with relevant temporal context. Finally, we use a linear classification layer to project the enriched region features outputted by the cross-attention layer into either instrument or atomic action class probability distributions.

Although the region classification head can be agnostic to the specific region proposal method, we use our instrument segmentation baseline (explained in Section 4.1) to obtain pixel-wise instrument instance region proposals and their per-segment embeddings. Hence, our region classification head cross-attends these shape-wise embeddings with the temporal cues of the video feature extractor to enhance the instrument region classification process and predict each instrument’s atomic actions. Figure 10 shows this head in the upper-right part.

4.4. Implementation Details

Instrument Segmentation Baseline: We used the official PyTorch implementation of Mask2Former⁷. We trained Mask2Former for 100 epochs on 4 NVIDIA Quadro RTX 8000 GPUs using a batch size of 32 for a ResNet50 backbone (He et al. (2016)) and 4 for a Swin Large (Liu et al. (2021)) backbone. We used a base learning rate of $1e^{-5}$ decayed by 0.1 in epochs 50 and 75 and an ADAMW optimizer (Loshchilov and Hutter (2019)). We used the publicly available pretrained weights for instance segmentation on the MS-COCO dataset (Lin et al. (2014)). We selected the top 5 scoring regions with more than 0.1 confidence scores for inference and region selection.

Phase and Step Recognition: We used MViT’s official implementation⁸. Using a cross-entropy loss, we trained MViT with its Base configuration for 30 epochs on a single NVIDIA Quadro RTX 8000 GPU. We trained our models using MViT’s pretrained weights in Kinetics 400 (Kay et al. (2017)). We used windows of 16 frames with a stride of 4 seconds (0.25fps sampling rate) for phases recognition and 1 second (1fps sampling rate) for steps recognition, and we used a batch size of 24 for both tasks. We used a cosine learning rate scheduler (Loshchilov and Hutter (2017)) with 5 warm-up epochs and an SGD optimizer with a base learning rate of $1.25e^{-3}$ and an end learning rate of $1e^{-4}$.

Instrument Region Classification: We trained TAPIS for 20 epochs in a single NVIDIA Quadro RTX 8000 GPU with a batch size of 24. We used time windows of 16 frames with a stride of 0.5 seconds (2fps sampling rate). We used a cosine learning rate (Loshchilov and Hutter (2017)) with 0 warm-up epochs and an SGD optimizer with a base learning rate of $1.25e^{-2}$ and an end learning rate of $1e^{-4}$. We trained our models using the pretrained weights in phases recognition.

⁷<https://github.com/facebookresearch/Mask2Former>

⁸<https://github.com/facebookresearch/SlowFast>

Table 4: **Performance of TAPIS in GraSP.** We report the results of TAPIS on the test set of GraSP, and we compare its performance with a CNN-based baseline (SlowFast), the TAPIR model proposed in Valderrama et al. (2022) and a Video Swin Transformer-based implementation (TAPIS-VST). We present the number of parameters (Params.) and floating point operations (FLOPs) of each model without counting the region proposal network. The best results are shown in bold.

| Method | FLOPs (G) | Params. (M) | Long-Term Tasks mAP (%) | | Short-Term Tasks $mAP@0.5IoU_{box}$ (%) | | Instrument Segmentation Metrics (%) | | | |
|-----------|-----------|-------------|---------------------------|--------------|---|----------------|-------------------------------------|--------------|--------------|--------------|
| | | | Phases | Steps | Instruments | Atomic Actions | $mAP@0.5IoU_{segm}$ | mIoU | IoU | mIoU |
| SlowFast | 81 | 33 | 70.70 | 46.23 | 74.33 | 22.01 | 71.32 | 77.16 | 72.26 | 58.75 |
| TAPIR | 71 | 36 | 74.55 | 49.42 | 74.43 | 25.57 | – | – | – | – |
| TAPIS-VST | 66 | 96 | 70.88 | 46.99 | 90.29 | 33.10 | 89.58 | 86.36 | 83.51 | 77.54 |
| TAPIS | 71 | 44 | 76.07 | 49.42 | 89.85 | 39.26 | 89.10 | 86.61 | 83.38 | 77.42 |

Atomic Action Detection: We trained TAPIS for 50 epochs in a single NVIDIA Quadro RTX 8000 GPU with a batch size of 24 and binary a cross-entropy loss. We used the pre-trained weights in phases recognition as initialization. We used time windows of 16 frames with the smallest stride possible (0.033 stride or 30fps sampling rate). We used a cosine learning rate (Loshchilov and Hutter (2017)) with 0 warm-up epochs and an SGD optimizer with a base learning rate of $1.25e-1$ and an end learning rate of $1e-2$.

Benchmarking: We performed all our optimization and design experiments in the defined cross-validation folds. For testing, we re-trained our best models selected during cross-validation in the entire training set (fold one plus fold two) and tested them on the defined test set. We do this to take full advantage of the entire extension of the training data. Since we maintain the atomic action evaluation as a detection evaluation, we consider the bounding boxes generated directly from the edges of the predicted instrument masks as bounding box predictions (no further bounding box coordinates regression). Finally, our collected videos include multiple flags, signals, and indicators about the mounted instruments and their usage. To avoid biases and correctly assess our models’ recognition capabilities, we removed all these signals from the sampled images throughout all our models and experiments. We provide an example of this frame modification procedure in the Supplementary Material.

5. Experiments and Results

We present our overall test results in Table 4. Based on the experimental setup presented in Valderrama et al. (2022), we compare the performance of the best TAPIS model with a CNN-based baseline. For this alternative baseline, we employ SlowFast (Feichtenhofer et al. (2019)) as the central video feature extractor and use ISINet (González et al. (2020)) (based on Mask R-CNN (He et al. (2017))) as the region proposal network for short-term tasks. We use the exact implementation details of SlowFast presented in Valderrama et al. (2022). We call this model SlowFast in Table 4. We also compare TAPIS with an alternative implementation using Video Swin Transformer (VST) (Liu et al. (2022)) as the video feature extractor and maintaining our proposed *region classification head*; we call this model TAPIS-VST in Table 4. The results in Table 4 demonstrate TAPIS’s and VST-TAPIS’s superiority over the CNN-based counterpart. This behavior proves that the inherent sequence-processing capability of transformers allows for a superior comprehension of temporal progressions, and their attention mechanisms result in better recognition of instruments, anatomical cues, and other relevant visual contexts

in surgical videos, leading to higher performance in all the proposed semantic tasks. Likewise, TAPIS surpasses TAPIS-VST in most tasks and achieves comparable instrument segmentation performance with significantly fewer parameters. The outperformance of TAPIS over TAPIS-VST in phases, steps, and actions recognition proves that our global video feature extractor is optimal and sufficient to understand the temporal progressions of surgical procedures. Although TAPIS-VST yields a better instrument region classification performance due to its finer-grained spatial processing and its increased amount of parameters, it still surpasses TAPIS by less than a 0.5% relative improvement with more than twice the parameters, hence highlighting TAPIS’s satisfactory performance.

Moreover, Table 4 also compares TAPIS’ performance with the TAPIR model (Valderrama et al. (2022)). To ensure a fair comparison, we train TAPIR with its original implementation details, parameters, and box proposal architecture (Deformable DETR (Zhu et al. (2021))) on the training set of GraSP and test its performance on the test set. This comparison reveals that TAPIS significantly outperforms TAPIR across all tasks in the GraSP benchmark, especially in the novel and highly challenging atomic action detection task, where TAPIS achieves more than a 53% relative improvement over TAPIR’s results. The performance difference proves the potential of our instrument segmentation annotations for short-term tasks and underscores the impact of our technical improvements and methodological experimentation. Notably, TAPIR exhibits a slight decrease in performance for short-term tasks compared to the originally reported metrics in PSI-AVA⁹, which we attribute to the refining and curation of our dataset that eliminated biases and included annotations for challenging tiny instrument segments that were previously unannotated. The superiority of TAPIS over TAPIR and all alternative baselines positions it as state-of-the-art in all tasks of our GraSP dataset.

5.1. Validation of TAPIS in Public Benchmarks

In this section, we validate the consistency of our proposed methods by analyzing TAPIS’s performance on multiple publicly available benchmarks. Specifically, we compare the performance of our method with either previously proposed models on those benchmarks or our own proposed alternative baselines. In turn, these comparisons lend themselves to assessing our dataset’s solidity by contrasting the relative performance behavior of our proposed architectures in alternative benchmarks to their performance behavior in GraSP. Thus, Subsec-

⁹<https://github.com/BCV-Uniandes/TAPIR>

Table 5: **Comparative Results of TAPIS in Instrument and Action Presence Recognition in GraSP.** We report the results of our model on frame-wise prediction of instrument presence and atomic action presence, regardless of location or instance count. The best results are shown in bold.

| Model | Presence mAP (%) | |
|----------------------------------|--------------------|--------------|
| | Instruments | Actions |
| Rendezvous (Nwoye et al. (2022)) | 80.41 | 20.65 |
| TAPIS w/o region proposals | 61.39 | 12.27 |
| TAPIS (Ours) | 95.05 | 43.57 |

tion 5.1.1 describes how we follow the conventional instrument and action recognition formulation in Twinanda et al. (2016); Nwoye et al. (2022); Maier-Hein et al. (2021); Wagner et al. (2023) and adapt our benchmark and methods for frame-wise recognition of instrument and action presence. Later, Subsections 5.1.2 and 5.1.3 explain how we also tailor our methods to analogous datasets in phases, steps, and gesture recognition (Huauilmé et al. (2021); van Amsterdam et al. (2022)), and even instrument-centric action localization (Islam et al. (2020)).

5.1.1. Instruments and Actions Presence Recognition

Given that GraSP includes instrument localization annotations, we expand our model evaluation to cover simpler and coarser tasks, such as recognizing the presence of instruments and associated actions. For this purpose, we adapt the dataset by transforming annotations into single binary vectors of dimensions $[1, N]$ for multi-label classification in each frame, where N represents the number of classes (7 for instruments presence and 14 for actions presence). To enable TAPIS to execute this task, we modify the model output to consolidate predictions from each predicted region into a single classification vector. Since it is our best region proposal method, we employ our instrument segmentation baseline with a SwinL backbone as the region proposal model.

We compare TAPIS’s performance with two alternative baselines to validate our data and model. First, an alternative implementation of TAPIS without region proposal features that predicts instruments and actions presence directly from the video feature extractor. Second, with Rendezvous (Nwoye et al. (2022)), a state-of-the-art model for recognizing the presence of actions and instruments. This model predicts triplets in the form of $\langle Instrument, Verb, Target \rangle$, where verb categories indicate the actions of each instrument in the keyframe, treated as analogous to the action categories in GraSP. To adapt Rendezvous for instrument presence recognition, we utilize all instrument categories, along with the “null verb” and “null target” categories, forming the triplets. Similarly, for the action presence task, we employ all action categories, along with the “instrument” and “null target” categories, to create the triplets. Additionally, we modify Rendezvous’ outputs according to the multi-label nature of GraSP actions. This adjustment included generating triplets for all actions present within each keyframe. Importantly, we train the models without pretraining on surgical datasets to ensure a fair comparison while preserving the pretraining in COCO of our region proposal network. The evaluation metric used for assessing performance was the mAP .

The results in Table 5 demonstrate that TAPIS strongly out-

Table 6: **Comparative results of TAPIS in Instrument and Interactions Detection on the EndoVis 2018 dataset.** We test our TAPIS model in the benchmark proposed in Islam et al. (2020) and compare our performance with previously proposed methods. The best results are shown in bold.

| Model | $mAP@0.5IoU_{box}$ (%) | |
|--|------------------------|--------------|
| | Instruments | Interactions |
| MSLRGR-GISFSG (Seenivasan et al. (2022)) | 42.59 | 39.11 |
| TAPIS (Ours) | 63.55 | 41.97 |

performs its implementation without region proposals and the Rendezvous model. These findings underscore the significance of having localized information from instruments and actions over time, as they provide valuable insights for the model and enhance its overall understanding. The results further validate that the spatial information offered by GraSP is essential for a comprehensive understanding of the surgical scene. These outcomes are also influenced by the temporal component of TAPIS, enabling more consistent predictions over time and integrating global information from the video feature extractor with local information from the region proposal method.

5.1.2. Interactions Recognition in Endovis 2018

To compare our method with other models in alternative instrument and action detection benchmarks, we test our model on the Endovis 2018 interaction dataset (Islam et al. (2020)) and compare its performance with a current publicly available state-of-the-art method for this dataset. We adhere to the established splits in (Islam et al. (2020)), excluding the *stapler* class present in only one sequence of the dataset. Additionally, we omit the *kidney* class during the training and evaluation of TAPIS, as our model does not include tissue information to predict the actions performed by each instrument. In this experiment, we train TAPIS to simultaneously address instrument and action detection by combining the instrument and action losses multiplied by fixed coefficients. The composite loss function used for training used a 0.95 coefficient for the action detection loss and a 0.05 coefficient for the instrument detection loss.

We employ DINO (Zhang et al. (2023)) as our instrument detector and use the proposed $mAP@0.5IoU_{box}$ metric for evaluation. For a fair comparison, we evaluate the predictions made by the other models for each instrument (excluding the *kidney* category) as a conventional detection problem. We compare our method with MSLRGR-GISFSG (Seenivasan et al. (2022)), which simultaneously performs semantic instrument segmentation and interaction detection utilizing a graph reasoning approach. To compare accurately with this method, which relies on ground-truth bounding boxes for inference, we assume perfect bounding box locations for instruments, as this model does not perform direct detection. For interactions, we used the model’s predicted class for each box. We assign the bounding box class for instruments based on the instrument mask predicted within it.

On the one hand, the results shown in Table 6 highlight the significant proficiency of our method in instrument localization, once more emphasizing the superiority of transformer-based models for detection tasks compared to CNN approaches. On the other hand, TAPIS outperforms a state-of-the-art method in

Table 7: **Comparative results of TAPIS in gesture recognition task on the RARP-45 dataset.** We compare the performance of TAPIS and its alternative baseline architectures on gesture recognition in the dataset proposed by van Amsterdam et al. (2022). The best results are shown in bold.

| Method | FLOPs (G) | Param (M) | Gesture Recognition <i>mAP</i> |
|--------------|-----------|-----------|--------------------------------|
| SlowFast | 25.29 | 33.7 | 49.00 |
| TAPIS-VST | 65.76 | 87.7 | 52.65 |
| TAPIS | 70.80 | 36.3 | 57.25 |

the interaction detection task. Despite the graph structure of the dataset, TAPIS effectively extracts rich information from each keyframe by combining global and temporal information from the video feature extractor and local details from the detector, proving that our proposed methodology is highly competitive in comprehending complex relationships between instruments with the surgical scene.

5.1.3. Gesture Recognition in RARP45

We further validate our methodology using the RARP-45 public gesture recognition benchmark. Given the absence of a public test set in the original RARP-45 dataset, we create our splits, using 27 videos for training and 9 videos for evaluation. To ensure the integrity of the splits, we maintain a consistent class distribution with the original training set. Specifically, for the test split, we select videos 2, 3, 4, 6, 7, 9, 14, 17, 23, 28, 32, and 33, while we use the remaining videos for the training split.

Following our previous experimental framework, we compare our method with its alternative versions using SlowFast and VST as video feature extractors. All experiments employed a window of 16 frames with a stride of 1. As shown in Table 7, our TAPIS model outperforms the alternative baselines, with all transformer-based methods surpassing the CNN model. This behavior demonstrates our model’s robustness by achieving outstanding performance in tasks analogous to the ones proposed in GraSP yet differently formulated. These results are consistent with the findings in the GraSP dataset, thus reinforcing the effectiveness of our approach in handling video-level tasks and proving the reliability of our results.

5.1.4. Phase and Step Recognition in MISAW

To further validate our results in phases and steps recognition, we test our models on the MISAW dataset (Hualmé et al. (2021)), which is analogous in long-term tasks to GraSP. We again follow the experimental setup we define for GraSP and compare the performance of the different explored architectures for GraSP (SlowFast and TAPIS-VST) in the phases and steps recognition benchmarks of the MISAW dataset.

We use a temporal window of 16 frames and a temporal stride of 1 second for our setting in MISAW. Moreover, we use cases 1-17 for training and 18-27 for validation, as proposed by the authors in Hualmé et al. (2021). The results in Table 8 portray the performance of our TAPIS model when evaluated on the MISAW dataset. Compared to both SlowFast and VST architectures, TAPIS performs better on both phases and steps recognition tasks. These results are also consistent in proving the potential advantages of using Transformers for video feature extraction over CNNs across both benchmarks and recti-

Table 8: **Comparative results of TAPIS in phases and steps recognition on the MISAW dataset.** We compare the performance of TAPIS and its alternative baseline architectures on Phase and Step recognition in the benchmark proposed by Hualmé et al. (2021). The best results are shown in bold.

| Method | FLOPs (G) | Param (M) | Long-Term Tasks <i>mAP</i> (%) | |
|--------------|-----------|-----------|--------------------------------|--------------|
| | | | Phases | Steps |
| SlowFast | 25.29 | 33.66 | 94.04 | 70.50 |
| TAPIS-VST | 65.76 | 87.65 | 96.16 | 73.46 |
| TAPIS | 70.80 | 36.31 | 97.14 | 77.52 |

fying the correctness of the method we propose for addressing phase and step understanding tasks.

5.2. Design and Ablation Experiments

5.2.1. Long-Term Tasks Experiments

We conduct design studies to determine the optimal temporal window for both phases and steps recognition tasks. We aim to define the best configuration for each task within our computational resource limitations. We present our results in Tables 9 and 10.

As stated earlier in this work, phases comprise broader temporal segments within surgical procedures, implying the need for a broader temporal context to recognize them effectively. In our phases recognition temporal window design experiments illustrated in Table 9, we validate that a wide-spaced temporal window correlates positively with the phases recognition performance. These findings substantiate the statement that temporal windows that allow wide-reaching temporal context capture more relevant information for accurate phases recognition. However, the refinement of this temporal context showcases a trade-off in model performance, where excessively large and spaced temporal windows tend to hinder performance. Consequently, our optimal temporal context for accurate phase recognition is a 16-frame window with a 4-second temporal stride, capturing 64 seconds centered on the frame of interest. Remarkably, our optimal window design is consistently related to average phase duration statistics showcased in Figure 4, where phase duration ranges mostly from 45 to 300 seconds approximately. Therefore, a 64-second temporal window encapsulates the semantic context needed to discern among different surgical phases.

In contrast, steps represent finer-grained time segments within these phases. Consequently, discerning these discrete steps requires a more detailed temporal context around the central frame to extract relevant features for step differentiation effectively. As detailed in Table 10, our analysis highlights that employing temporal windows sampled with shorter temporal stride (higher frame rates) results in higher performance in steps recognition. Increasing the temporal stride reduces performance, and excessively augmenting it yields the lowest *mAP* values observed. We find that the optimal temporal window for step recognition is to keep a 16-frame window size and use a low 1-second temporal stride so the model captures a temporal window of 16 seconds centered on the frame of interest. Our optimal window design is consistently related to average step duration statistics from Figure 5, where step duration ranges mostly from 10 to 200 seconds approximately. Notably, steps

Table 9: **Temporal window design experiments for Phase Recognition in the cross-validation set.** The number of frames denotes the temporal window size centered on the frame of interest. Temporal stride is the gap between consecutive sampled frames of the sequence in seconds. The best results are shown in bold.

| Window Size | Temporal Stride (seconds) | <i>mAP</i> (%) |
|-------------|---------------------------|-------------------------|
| 16 | 1 | 72.21 \pm 0.8 |
| 16 | 4 | 72.90 \pm 1.65 |
| 16 | 8 | 71.40 \pm 0.24 |
| 24 | 1 | 72.41 \pm 1.04 |
| 24 | 4 | 72.27 \pm 1.22 |
| 32 | 4 | 72.04 \pm 1.70 |

exhibit a wider range of durations compared to phases. This variability implies that employing a uniform temporal window to identify all step categories poses a challenge, as certain instances might require a larger temporal context for accurate identification compared to others.

Studying the temporal windows for each task allows us to acknowledge the relationship between the temporal window resolution designed for each task and the multi-level understanding nature of our dataset. As we show in Table 9 and 10, tasks with finer granularity, such as steps, require higher temporal resolutions for our model to discern individual steps effectively. In contrast, tasks with lower granularity, such as phases, demand lower resolutions of temporal context for our model to distinguish them accurately.

Additionally, we present more specific results of phases and steps recognition per-class performance in the Supplementary Material. Initially, the assessment of the model’s performance across diverse phase categories reveals differing levels of success in identifying individual surgical phases. Notably, phases 1-6 and 10 consistently attain relatively higher *AP* scores across all three methods, while categories 7 and 8 exhibit relatively lower scores. When correlating these observations with the dataset statistics (Figure 2), it is notable that the phases with lower *AP* scores across the methods display a low representation in the dataset, as it is natural when studying long-tailed datasets. Additionally, the lower mean duration of these phases (Figure 4) might contribute to the model finding it more challenging to discern and accurately predict these phases, such as classes 7 and 8. This relation is related to the broader temporal stride that may not be optimal for shorter phase instances that span fewer consecutive frames.

Similarly, the model’s performance across various step categories reveals that steps 12 to 18 and 20, characterized by lower mean durations, exhibit lower Average Precision (*AP*) scores across the evaluated methods. Additionally, less represented step classes in the dataset, like 6, 7, and 11, tend to manifest lower *AP* scores, and steps 0, 1, and 19, with higher representation, demonstrate comparatively better performance. However, the model’s performance was still low for some highly represented classes like 2, 3 and 5. This effect may be due to the high variability in these steps’ duration, as shown in Figure 5. Once again, the varying performance between classes is related to the fixed temporal window design, which may not be optimally suited to capture the high inter and intra-class variability

Table 10: **Temporal window design experiments for Step recognition in the cross-validation set.** The number of frames denotes the temporal window size centered on the frame of interest. Temporal stride is the gap between consecutive sampled frames in seconds. The best results are shown in bold.

| Window Size | Temporal Stride (seconds) | <i>mAP</i> (%) |
|-------------|---------------------------|-------------------------|
| 16 | 0.10 | 45.40 \pm 0.78 |
| 16 | 0.23 | 46.56 \pm 0.66 |
| 16 | 1 | 48.36 \pm 1.14 |
| 16 | 4 | 43.95 \pm 1.07 |
| 24 | 0.10 | 45.31 \pm 0.17 |
| 24 | 0.23 | 46.55 \pm 0.07 |
| 24 | 1 | 48.23 \pm 2.30 |
| 32 | 0.10 | 45.13 \pm 0.36 |
| 32 | 0.23 | 46.55 \pm 0.44 |
| 32 | 1 | 48.02 \pm 1.13 |

Table 11: **Comparative results in Instrument Detection in the cross-validation set.** We test multiple object detection architectures using the bounding boxes generated by GraSP’s segmentation annotations. We also report the number of parameters (Params.) and floating point operations (FLOPs) of each model. The best results are shown in bold.

| Model | Backbone | FLOPs (G) | Params (M) | <i>mAP</i> @0.5IoU _{box} |
|-----------------|----------|-----------|------------|-----------------------------------|
| Faster R-CNN | R50 | 180 | 42 | 80.88 \pm 1.16 |
| Deformable DETR | R50 | 173 | 40 | 87.33 \pm 2.91 |
| DINO | SwinL | 310 | 218 | 90.93 \pm 1.15 |

in the duration of different step instances.

5.2.2. Instrument Segmentation Experiments

Due to our new instance segmentation annotations and the data curation process, our annotations in GraSP have more precise bounding box coordinates than the PSI-AVA benchmark. In this section, we first assess the performance of multiple object detectors on these bounding box annotations, and we use these results as reference points for our experiments with instance segmentation. For this purpose, we adapt, train, and optimize multiple object detectors on our cross-validation set and present our results in Table 11. We compare Faster R-CNN (Ren et al. (2017)) as a CNN-based detector with Deformable DETR (Zhu et al. (2021)) as a transformer-based detector. In this work, we also test DINO (Zhang et al. (2023)) with its largest backbone (Swin Large (Liu et al. (2021))) as a way of including a larger and more recent state-of-the-art method in the evaluation of instrument detection performance. Our results show that transformer-based detectors consistently surpass CNN-based detectors and that the DINO detector performs better than Deformable DETR. These results are consistent with our initial results (Valderrama et al. (2022)) and with the general state-of-the-art in object detection, thus showing the reliability of our data and its applicability for instrument detection tasks.

Furthermore, we validate our segmentation annotations by training and optimizing ISINet (González et al. (2020)) as a CNN-based baseline and comparing it with our instrument segmentation baseline (called *TAPIS Frame*), as detailed in Table 12. We evaluate the performance of *TAPIS Frame* using multiple backbones, including ResNet50, for comparison with ISINet and a Swin Large (SwinL) backbone to lever-

Table 12: **Comparative results of TAPIS in Instrument Segmentation in the cross-validation set.** We showcase the instance and semantic segmentation performance of our instrument segmentation baseline (*TAPIS Frame*) and our complete model (*TAPIS Full*), and we compare it to our CNN baseline and previous state-of-the-art models for instrument segmentation. The parameters and floating point operations reported for the *TAPIS Full* models correspond to the video feature extractor and the region classification head while the values reported for *TAPIS Frame* correspond to Mask2Former. The best results are shown in bold.

| Model | Backbone | FLOPs (G) | Params. (M) | Instance Segmentation Metrics (%) | | Semantic Segmentation Metrics (%) | | |
|--|----------|-----------|-------------|-----------------------------------|---------------------|-----------------------------------|--------------------|--------------------|
| | | | | $mAP@0.5IoU_{box}$ | $mAP@0.5IoU_{segm}$ | mIoU | IoU | mcIoU |
| TernausNet (Shvets et al. (2018)) | UNet 16 | - | - | - | - | 41.74 ±5.07 | 24.46 ±6.04 | 16.87 ±3.70 |
| MF-TAPNet (Jin et al. (2019)) | TAPNet | - | - | - | - | 66.63 ±1.24 | 29.23 ±1.43 | 24.98 ±0.59 |
| ISINet (González et al. (2020)) | R50 | 201 | 44 | 79.85 ±2.17 | 78.29 ±2.82 | 78.44 ±1.13 | 70.85 ±0.00 | 56.67 ±1.46 |
| QPD Mask DINO (Dhanakshirur et al. (2023)) | R50 | 228 | 54 | 88.46 ±1.14 | 87.39 ±1.75 | 83.89 ±1.23 | 82.56 ±1.14 | 74.36 ±1.04 |
| TAPIS Frame | R50 | 226 | 44 | 89.65 ±1.26 | 88.65 ±1.43 | 84.81 ±1.62 | 81.34 ±1.44 | 73.48 ±0.88 |
| TAPIS Full | | 71 | 44 | 88.66 ±0.79 | 87.20 ±1.12 | 84.76 ±1.63 | 81.64 ±1.45 | 74.43 ±0.79 |
| TAPIS Frame | SwinL | 868 | 216 | 92.65 ±1.57 | 91.71 ±1.72 | 86.91 ±1.59 | 83.92 ±0.68 | 77.59 ±0.08 |
| TAPIS Full | | 71 | 44 | 91.72 ±0.87 | 90.34 ±1.11 | 87.05 ±1.63 | 84.45 ±0.72 | 78.82 ±0.88 |

age the most extensive backbone configuration. Our findings consistently demonstrate the superiority of transformer-based methods, with performance positively correlating with the number of parameters of the backbone. Notably, all instance segmentation methods exceed their detection counterparts in $mAP@0.5IoU_{box}$, with even the most minor *TAPIS Frame* configuration achieving comparable performance to the largest detector with less than half of the parameters and FLOPs. These results highlight our segmentation annotations’ impact on training specialized models that capture finer visual cues regarding the pixel-level shape of instruments that improve instrument localization and recognition. Additionally, as shown in Table 12, we test multiple publicly available instrument segmentation methods on our cross-validation set. For this purpose, we optimize and adapt methods designed for instrument segmentation in Endovis 2017 and 2018 by using their official public implementations; these methods include TernausNet (Shvets et al. (2018))¹⁰ and MF-TAPNet (Jin et al. (2019))¹¹ for semantic segmentation, and ISINet (González et al. (2020))¹² and QPD Mask DINO (Dhanakshirur et al. (2023))¹³ for Instance Segmentation. These methods yield a relative behavior that aligns with the current state-of-the-art in instrument segmentation and underscores the enhanced performance of our instrument segmentation model over previous approaches. Also, they consistently prove the superiority of Transformer-based architectures.

Moreover, Table 12 also presents the performance of the entire TAPIS model for instrument segmentation (called *TAPIS Full*), which integrates the *region classification head* with the *TAPIS Frame*’s region proposals. The metrics for this experiment, including parameters and FLOPs, focus on the video feature extractor and the *region classification head*. Including the *region classification head* enhances performance in the highly stringent semantic segmentation metrics, although with a decrease in $mAP@0.5IoU_{segm}$ performance. We attribute this outcome to the head’s ability to accurately reclassify more prominent and complex regions by correlating them over time. However, it tends to misclassify smaller, independent regions that appear momentarily, resulting in higher recall regarding inter-

section over union but slightly reduced effectiveness in instance identification. Throughout our experimentation, we noted minimal variance in instrument classification performance related to the specific design of the time window and the *region classification head*. However, we observed marginally lower performance with windows covering less than 8 seconds and achieved the optimal performance using a sampling rate of 2fps. Consequently, we opted for a window design comprising 16 frames at a 2fps sampling rate.

We provide detailed results of per-class instrument segmentation performance in the Supplementary Material. On the one hand, the per-class performance is highly correlated to the frequency of each instrument type within the dataset. On the other hand, the results are significantly affected by the specific identity of each instrument and its typical presence in surgeries. For example, the MCS demonstrates excellent performance due to its distinctive shaft and tip and its frequent, clear visibility in the frontal parts of the video. Similarly, besides its unique tip, the LND often appears alone during parts of the surgery where few other instruments are present, thus underlining the importance of the visual surgical context in segmentation accuracy. On the contrary, the PF exhibits lower performance due to frequent occlusions and their appearance in distant, smaller parts of the image. Besides often being covered by other instruments or objects, the LI presents high intra-class variability. It appears in various forms throughout our data as it is a generic category for external laparoscopic instruments independent from the da Vinci Surgical System. This variability in performance further emphasizes the complex nature of instrument segmentation in surgical videos and the necessity of considering the entire visual and temporal context.

Figure 11 shows examples of qualitative results of TAPIS for instrument segmentation, and we present more examples in the Supplementary Material. These results demonstrate that TAPIS achieves a very high segmentation performance in both instrument recognition capabilities and pixel-level delineation precision. For example, the results on the left part of Figure 11 demonstrate TAPIS’s ability to accurately segment complex images with up to five instrument instances with intricate, varied, and occasionally overlapping figures. The second row on the left shows an example of a correct segmentation with significantly overlapping instances. Nevertheless, our method presents some error patterns related to high occlusions and complicated instrument appearances. The results on the first three

¹⁰<https://github.com/ternaus/robot-surgery-segmentation>

¹¹<https://github.com/keyuncheng/MF-TAPNet>

¹²<https://github.com/BCV-Uniandes/ISINet>

¹³<https://github.com/AINeurosurgey/Learnable-QPD-for-maskDINO>

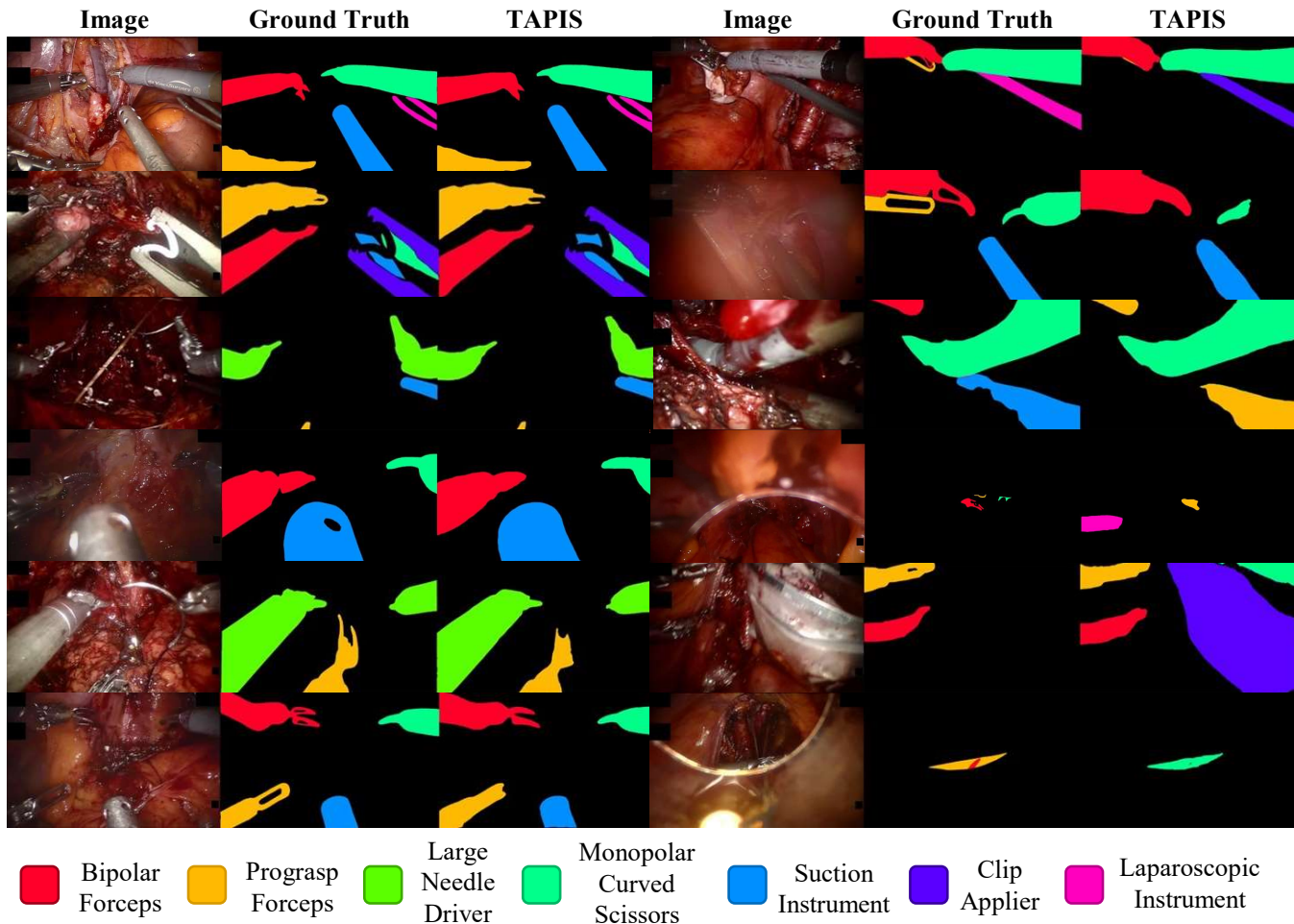


Fig. 11: **Qualitative Results of TAPIS in Instrument Segmentation.** We present twelve examples of our best model’s segmentation results. The first three rows on the left show nearly perfect results, the next three rows on the left show average results, the first three rows on the right show slight segmentation errors and the last three rows show significant segmentation errors.

rows on the right show minor defects on moving and still instruments occluded by tissue and fluids. The last three rows on the right show examples of inaccurate predictions due to a high degree of overlapping between instances and a problematic view of specific instruments, which makes them challenging to segment accurately, even for the naked eye. However, we highlight that TAPIS achieves a very high segmentation recall as it can propose a segmentation mask to cover most instances, failing primarily in tiny segments. These insights prove our proposal’s strength but show room for improvement in segmentation.

5.2.3. Atomic Action Detection

We first evaluate the impact of using different region proposal networks for the action detection tasks. Table 13 contains the results of testing TAPIS’s atomic action detection performance and our proposed *region classification head* with region features provided by multiple transformer-based architectures. We also report the number of parameters and floating point operations of those region proposal architectures. The results demonstrate that performance in atomic action detection increases proportionally to instrument detection or segmentation performance. This relation occurs since higher-quality region proposals provide a broader instrument location recall and

Table 13: **Comparative results of TAPIS in Atomic Action Detection.** We present the results of employing region features from multiple detection and segmentation models. We also report the number of parameters and floating point operations corresponding to the region proposal networks. The best results are shown in bold.

| Model | Region Proposal Method | | | $mAP@0.5IoU_{box}$ (%) |
|-----------------|------------------------|-----------|-------------|------------------------------------|
| | Backbone | FLOPs (G) | Params. (M) | |
| Deformable DETR | R50 | 173 | 40 | 28.54 \pm 0.68 |
| DINO | SwinL | 310 | 218 | 31.37 \pm 0.50 |
| TAPIS Frame | R50 | 226 | 44 | 31.24 \pm 1.84 |
| | SwinL | 868 | 216 | 34.04 \pm 2.40 |

better recognition insights in their features, leading to increased action detection and recognition capabilities. Additionally, we observe that using *TAPIS Frame’s* features with a ResNet50 backbone achieves a comparable performance to DINO’s features with a SwinL backbone. These results highlight the impact of segmentation approaches as they provide finer-grained features with detailed cues of instruments’ shapes and poses that improve TAPIS’s understanding of the actions that those instruments perform. On top of that, for all the experiments, we used the pretrained weights in phase recognition as we observed that these learned models provided better results for atomic action detection.

Table 14: **Ablation results on the design of the region classification head in the cross-validation set.** We compare the performance in atomic action detection using the Time Pooling design of Valderrama et al. (2022), the Time MLP from Ayobi et al. (2023), and our new Cross-Attention layer design. The best results are shown in bold.

| Region Proposal Model | Atomic Actions $mAP@0.5IoU_{box}$ | | |
|-----------------------|-----------------------------------|------------------|-------------------------|
| | Time Pooling | Time MLP | Cross-Attention |
| Deformable DETR | 25.03 \pm 1.06 | 26.97 \pm 0.09 | 28.54 \pm 0.68 |
| DINO | 26.64 \pm 2.39 | 28.64 \pm 0.34 | 31.37 \pm 0.50 |
| TAPIS Frame (R50) | 29.61 \pm 0.72 | 30.67 \pm 0.08 | 31.24 \pm 1.84 |
| TAPIS Frame (SwinL) | 32.48 \pm 1.23 | 33.43 \pm 1.38 | 34.04 \pm 2.40 |
| FLOPs (G) | 0.003 | 0.633 | 0.538 |
| Params. (M) | 0.289 | 8.882 | 8.086 |

Moreover, we assess our proposed *region classification head* compared with TAPIR’s design (Valderrama et al. (2022)). TAPIR’s box classification head performed a mean pooling of spatio-temporal features and concatenated the result with the region embeddings for a final linear classification. We now evaluate the efficacy of employing a cross-attention layer that correlates the region features with the spatio-temporal features of the video feature extractor. For a fair comparison, given the higher parameters and floating point operations count of the cross-attention layer, we also test using a multi-layer perceptron (MLP) similar in design to the one presented in MATIS (Ayobi et al. (2023)), which consists of multiple linear layers before and after the pooling operation. Table 14 shows the results of using TAPIR’s original design (Time Pooling), MATIS’s design (Time MLP), and our proposed cross-attention layer (Cross-Attention). The results show that, for any region proposal architecture, the performance scales with the number of parameters as the Time MLP outperforms the Time Pooling, thus showing consistency with the results reported in Ayobi et al. (2023). More importantly, the cross-attention layer significantly outperforms both Time MLP and Time Pooling designs despite having slightly lower Parameters and FLOPs counts than the Time MLP. This improvement demonstrates the effectiveness of our proposed design, where the cross-attention layer allows region embeddings to attend to all the features extracted by the video feature extractor, hence avoiding the heavy loss of information caused by pooling the rich sequence of temporal embeddings. Therefore, our proposed *region classification head* performs better since it classifies features enriched by observing the complete temporal information provided by the video feature extractor.

Finally, we conduct a series of design experiments to achieve the optimal time window size for atomic action detection, and we present our results in Table 15. Our observations reveal that our model performs best when the window size ranges between 16 and 32 frames, and we note a significant drop in performance when using a smaller window size. We attribute this decline to the model’s reduced temporal field, compromising its ability to capture atomic actions that extend over longer periods, such as tissue cauterization or cutting. Conversely, larger time windows also resulted in a slight decrease in performance. We hypothesize that this decline is due to the model processing noise from irrelevant distant frames, which complicates the correlation between region features and temporal embeddings. These results

Table 15: **Temporal window design experiments for atomic action detection.** The number of frames denotes the temporal window size centered on the frame of interest. Temporal stride is the gap between consecutive sampled frames in seconds.

| Window Size | Temporal Stride (seconds) | $mAP@0.5IoU_{box}$ (%) |
|-------------|---------------------------|-------------------------|
| 8 | 0.033 | 32.74 \pm 2.12 |
| 8 | 0.066 | 33.33 \pm 1.74 |
| 16 | 0.033 | 34.04 \pm 2.40 |
| 16 | 0.066 | 33.37 \pm 1.59 |
| 16 | 0.5 | 30.32 \pm 1.60 |
| 16 | 1 | 28.07 \pm 2.78 |
| 32 | 0.033 | 33.66 \pm 1.10 |
| 32 | 0.066 | 33.58 \pm 0.42 |

underscore the need for a more localized and centered temporal understanding of atomic action recognition.

Additionally, our experiments showed that decreasing the temporal window’s sampling rate per second (increasing the temporal stride) significantly decreases performance, hence validating our hypothesis about the temporal granularity of the atomic actions detection task. As their name indicates, atomic actions develop in extremely short periods, and they are a highly specific and granular form of modeling surgical activities. During the annotation process, we observed numerous instances where atomic actions unfolded in as few as four consecutive video frames. This observation indicates that the model requires a finer temporal sampling to fully identify actions over time. Consequently, the model performs best with the highest possible sampling rate, allowing for a more detailed and accurate temporal analysis of the surgical actions. This insight is crucial for enhancing the precision and effectiveness of atomic action detection in surgical videos.

We provide a table with the per-class results of the atomic action detection task in the Supplementary Material. The performance distribution is once again related to the frequency of each action’s occurrence within the dataset since actions like *travel*, *hold*, and *still* demonstrate the highest performance metrics. However, the complexity and variability of the actions also significantly influence their detectability. For example, actions like *cauterize* and *suction* record good AP values, as they are specific actions associated with particular instruments. Also, contextual cues provided by the video feature extractor, such as the appearance of smoke during cauterization or the movement of blood during suction, further aid in recognizing these actions. Conversely, while seemingly straightforward to identify, actions like *pull* and *push* often get confused with each other or with similar actions, leading to relatively lower performance. Moreover, abstract action categories such as *release* or *open something* can present in many ways within the surgical environment, making it challenging to consistently classify these actions accurately, as reflected in their low-performance metrics. This aspect of our results highlights the intricate nature of action detection in surgical videos and the need to precisely understand subtle and significant differences and overlaps in the motion patterns.

5.3. Discussion

The outstanding performance of TAPIS in different tasks and the consistency observed throughout our experiments in alternative frameworks and the GraSP dataset strongly emphasizes the efficacy of our proposed benchmark and methods. Our experimentation effectively showcases how our approach leverages the diverse granularity requirements of each task within the proposed multi-level hierarchy of surgical procedures. For instance, at the highest level of our task pyramid, phases recognition needed global and sparse time windows (64s at 0.25fps) to capture long-term procedural information effectively. Moving down the hierarchy, steps recognition achieved optimal performance with finer sampled time windows (16s at 1fps). Instrument recognition excelled with the most granular spatial recognition (pixel-wise) coupled with a relatively short and dense temporal field (8s at 2fps). Finally, at the base of the pyramid, atomic action detection, our lowest-level task, saw significant performance enhancements when applying the finest-grained approaches in time (0.53s at 30fps) and space.

Our results also confirm the hypothesized interrelationships among the tasks. We observed that using pretrained weights on the Phase recognition task could enhance performance in shorter-term tasks. Similarly, improving the recall in instrument recognition and employing shape-level recognition positively impacted the effectiveness of atomic action detection. This interconnected approach reinforces our understanding of the hierarchical nature of surgical scene analysis. Finally, TAPIS's superiority in the GraSP dataset and alternative benchmarks highlights our proposed method's robustness and ability to efficiently leverage multi-level annotations in endoscopic vision datasets. Although TAPIS achieves state-of-the-art performance across ours and alternative benchmarks, our results exhibit considerable room for improvement in all the proposed tasks of our framework. Still, our methodologies set a strong precedent and significantly push the envelope for future research in our benchmark to achieve a more holistic and multi-granular surgical scene understanding.

6. Conclusions

We have introduced a novel dataset and methodological framework to formulate surgical scene understanding into a holistic comprehension. Our approach models surgical procedures as a hierarchy of complementary long-term and short-term tasks, implicitly requiring multiple levels of visual understanding. By curating and enlarging our previously proposed benchmark for holistic surgical scene understanding and incorporating the surgical instrument instance segmentation task, we have presented the first Endoscopic Vision dataset that provides four distinct levels of visual understanding, each with the highest annotation granularity. Through detailed statistics of our dataset, we showed that our benchmark poses multiple challenges that are highly pertinent to real-life applications, effectively capturing the intricacies of robot-assisted surgical procedures. Additionally, we have established an explicit and reliable training, validation, and testing distribution to promote future reproducibility and comparability in our framework.

Furthermore, we developed the TAPIS model to exploit the provided annotations of our GraSP benchmark. Our results demonstrated the effectiveness of instrument segmentation annotations, allowing for better instrument recognition capabilities and providing helpful shape-level cues for better atomic action detection. Similarly, our extensive design experimentation with TAPIS highlighted each task's particular granularity requirements and the intrinsic complementarity among different tasks. Higher-level tasks achieved the best performance with sparser time windows, and lower-level tasks outperformed with finer spatial recognition and shorter-term temporal processing. Our method significantly performed all alternative baselines and previously proposed methods, thus underscoring the superiority of transformer-based approaches and setting a new state-of-the-art in holistic surgical scene understanding. We validated our benchmark and method's reliability by showing that TAPIS achieves a consistent relative performance in public benchmarks. Our work presents a significant advancement in the Endoscopic Vision field, aiming to promote a multi-granular and multi-level understanding of surgical procedures. This research is a stepping stone in holistic surgical scene understanding and image-guided surgical robot intelligence.

Acknowledgments: The authors would like to thank Natalia Valderrama and Paola Ruiz for their contributions to the early stages of this work. We would also like to thank Nicolás Cantillo and Gabriela Monroy for their contribution to data annotation and Dr. Felipe Gomez for his contributions to data collection. Isabela Hernández, Nicolás Ayobi, Alejandra Perez, and Santiago Rodríguez acknowledge the support of the 2021, 2022, and 2023 UniAndes-Google DeepMind Scholarships. This work was partially supported by Azure sponsorship credits granted by Microsoft's AI for Good Research Lab.

References

- Abu-El-Haija, S., Kothari, N., Lee, J., Natsev, A.P., Toderici, G., Varadarajan, B., Vijayanarasimhan, S., 2016. Youtube-8m: A large-scale video classification benchmark, in: arXiv:1609.08675. URL: <https://arxiv.org/pdf/1609.08675v1.pdf>.
- Ahmidi, N., Tao, L., Sefati, S., Gao, Y., Lea, C., Haro, B.B., Zappella, L., Khudanpur, S., Vidal, R., Hager, G.D., 2017. A dataset and benchmarks for segmentation and recognition of gestures in robotic surgery. *IEEE Transactions on Biomedical Engineering* 64, 2025–2041.
- Al Hajj, H., Lamard, M., Conze, P.H., Roychowdhury, S., Hu, X., Maršalkaitė, G., Zisimopoulos, O., Dedmari, M.A., Zhao, F., Prellberg, J., Sahu, M., Galdran, A., Araújo, T., Vo, D.M., Panda, C., Dahiya, N., Kondo, S., Bian, Z., Vahdat, A., Bialopetravičius, J., Flouty, E., Qiu, C., Dill, S., Mukhopadhyay, A., Costa, P., Aresta, G., Ramamurthy, S., Lee, S.W., Campilho, A., Zachow, S., Xia, S., Conjeti, S., Stoyanov, D., Armitis, J., Heng, P.A., Mcready, W.G., Cochener, B., Quellec, G., 2019. Cataracts: Challenge on automatic tool annotation for cataract surgery. *Medical Image Analysis* 52, 24–41. URL: <https://www.sciencedirect.com/science/article/pii/S136184151830865X>, doi:<https://doi.org/10.1016/j.media.2018.11.008>.
- Allan, M., Kondo, S., Bodenstedt, S., Leger, S., Kadkhodamohammadi, R., Luengo, I., Fuentes, F., Flouty, E., Mohammed, A., Pedersen, M., Kori, A., Alex, V., Krishnamurthi, G., Rauber, D., Mendel, R., Palm, C., Bano, S., Saibro, G., Shih, C.S., Chiang, H.A., Zhuang, J., Yang, J., Igloukov, V., Dobrenkii, A., Reddiboina, M., Reddy, A., Liu, X., Gao, C., Unberath, M., Kim, M., Kim, C., Kim, C., Kim, H., Lee, G., Ullah, I., Luna, M., Park,

- S.H., Azizian, M., Stoyanov, D., Maier-Hein, L., Speidel, S., 2020. 2018 robotic scene segmentation challenge. *arXiv:2001.11190*.
- Allan, M., Shvets, A., Kurmann, T., Zhang, Z., Duggal, R., Su, Y.H., Rieke, N., Laina, I., Kalavakonda, N., Bodenstedt, S., Herrera, L., Li, W., Igloukov, V., Luo, H., Yang, J., Stoyanov, D., Maier-Hein, L., Speidel, S., Azizian, M., 2019. 2017 robotic instrument segmentation challenge. *arXiv:1902.06426*.
- van Amsterdam, B., Funke, I., Edwards, E., Speidel, S., Collins, J., Sridhar, A., Kelly, J., Clarkson, M.J., Stoyanov, D., 2022. Gesture recognition in robotic surgery with multimodal attention. *IEEE Transactions on Medical Imaging* 41, 1677–1687. doi:10.1109/TMI.2022.3147640.
- Ayobi, N., Pérez-Rondón, A., Rodríguez, S., Arbeláez, P., 2023. Matis: Masked-attention transformers for surgical instrument segmentation, in: 2023 IEEE 20th International Symposium on Biomedical Imaging (ISBI), pp. 1–5. doi:10.1109/ISBI53787.2023.10230819.
- Baby, B., Thapar, D., Chasmai, M., Banerjee, T., Dargan, K., Suri, A., Banerjee, S., Arora, C., 2023. From forks to forceps: A new framework for instance segmentation of surgical instruments, in: 2023 IEEE/CVF Winter Conference on Applications of Computer Vision (WACV), IEEE Computer Society, Los Alamitos, CA, USA. pp. 6180–6190. URL: <https://doi.ieeecomputersociety.org/10.1109/WACV56688.2023.00613>, doi:10.1109/WACV56688.2023.00613.
- Barker, R., Wright, H., 1954. *Midwest and Its Children: The Psychological Ecology of an American Town*. Row, Peterson. URL: <https://books.google.com.co/books?id=rPQhAAAAAAAJ>.
- Bawa, V.S., Singh, G., Kaping, A., F., Skarga-Bandurova, I., Oleari, E., Leporini, A., Landolfo, C., Zhao, P., Xiang, X., Luo, G., Wang, K., Li, L., Wang, B., Zhao, S., Li, L., Stabile, A., Setti, F., Muradore, R., Cuzzolin, F., 2021. The saras endoscopic surgeon action detection (esad) dataset: Challenges and methods. *arXiv:2104.03178*.
- Blank, M., Gorelick, L., Shechtman, E., Irani, M., Basri, R., 2005. Actions as space-time shapes, in: Tenth IEEE International Conference on Computer Vision (ICCV'05) Volume 1, IEEE. pp. 1395–1402.
- Bodenstedt, S., Allan, M., Agustinos, A., Du, X., Garcia-Peraza-Herrera, L., Kennigott, H., Kurmann, T., Müller-Stich, B., Ourselin, S., Pakhomov, D., Sznitman, R., Teichmann, M., Thoma, M., Vercauteren, T., Voros, S., Wagner, M., Wochner, P., Maier-Hein, L., Stoyanov, D., Speidel, S., 2018. Comparative evaluation of instrument segmentation and tracking methods in minimally invasive surgery. *arXiv:1805.02475*.
- Caba Heilbron, F., Escorcia, V., Ghanem, B., Carlos Niebles, J., 2015. Activitynet: A large-scale video benchmark for human activity understanding, in: 2015 IEEE Conference on Computer Vision and Pattern Recognition (CVPR), pp. 961–970. doi:10.1109/CVPR.2015.7298698.
- Carion, N., Massa, F., Synnaeve, G., Usunier, N., Kirillov, A., Zagoruyko, S., 2020. End-to-end object detection with transformers, in: European conference on computer vision, Springer. pp. 213–229.
- Cheng, B., Misra, I., Schwing, A.G., Kirillov, A., Girdhar, R., 2022. Masked-attention mask transformer for universal image segmentation, in: 2022 IEEE/CVF Conference on Computer Vision and Pattern Recognition (CVPR), pp. 1280–1289. doi:10.1109/CVPR52688.2022.00135.
- Cheng, B., Schwing, A., Kirillov, A., 2021. Per-pixel classification is not all you need for semantic segmentation. *Advances in Neural Information Processing Systems* 34, 17864–17875.
- Chuchulo, A., Ali, A., 2023. Is Robotic-Assisted surgery better? *AMA J Ethics* 25, E598–604.
- Czempiel, T., Paschali, M., Ostler, D., Kim, S.T., Busam, B., Navab, N., 2021. Opera: Attention-regularized transformers for surgical phase recognition, in: de Bruijne, M., Cattin, P.C., Cotin, S., Padoy, N., Speidel, S., Zheng, Y., Essert, C. (Eds.), *Medical Image Computing and Computer Assisted Intervention – MICCAI 2021*, Springer International Publishing, Cham. pp. 604–614.
- De Backer, P., Van Praet, C., Simoens, J., Peraire Lores, M., Creemers, H., Mestdagh, K., Allaey, C., Vermijs, S., Piazza, P., Mottaran, A., Bravi, C.A., Paciotti, M., Sarchi, L., Farinha, R., Puliatti, S., Cisternino, F., Ferraguti, F., Debbaut, C., De Naeyer, G., Decaestecker, K., Mottrie, A., 2023. Improving augmented reality through deep learning: Real-time instrument delineation in robotic renal surgery. *European Urology* 84, 86–91. URL: <https://www.sciencedirect.com/science/article/pii/S0302283823026337>, doi:<https://doi.org/10.1016/j.eururo.2023.02.024>.
- Demir, K.C., Schieber, H., Weise, T., Roth, D., May, M., Maier, A., Yang, S.H., 2023. Deep learning in surgical workflow analysis: A review of phase and step recognition. *IEEE Journal of Biomedical and Health Informatics* 27, 5405–5417. doi:10.1109/JBHI.2023.3311628.
- Devlin, J., Chang, M.W., Lee, K., Toutanova, K., 2019. BERT: Pre-training of deep bidirectional transformers for language understanding, in: Burstein, J., Doran, C., Solorio, T. (Eds.), *Proceedings of the 2019 Conference of the North American Chapter of the Association for Computational Linguistics: Human Language Technologies, Volume 1 (Long and Short Papers)*, Association for Computational Linguistics, Minneapolis, Minnesota. pp. 4171–4186. URL: <https://aclanthology.org/N19-1423>, doi:10.18653/v1/N19-1423.
- Dhanakshir, R.R., Shastry, K.N.A., Borgavi, K., Suri, A., Kalra, P.K., Arora, C., 2023. Learnable query initialization for surgical instrument instance segmentation, in: Greenspan, H., Madabhushi, A., Mousavi, P., Salcudean, S., Duncan, J., Syeda-Mahmood, T., Taylor, R. (Eds.), *Medical Image Computing and Computer Assisted Intervention – MICCAI 2023*, Springer Nature Switzerland, Cham. pp. 728–738.
- Ding, X., Li, X., 2022. Exploring segment-level semantics for online phase recognition from surgical videos. *IEEE Transactions on Medical Imaging* 41, 3309–3319. doi:10.1109/TMI.2022.3182995.
- Dosovitskiy, A., Beyer, L., Kolesnikov, A., Weissenborn, D., Zhai, X., Unterthiner, T., Dehghani, M., Minderer, M., Heigold, G., Gelly, S., Uszkoreit, J., Houshy, N., 2021. An image is worth 16x16 words: Transformers for image recognition at scale, in: *International Conference on Learning Representations*. URL: <https://openreview.net/forum?id=YicbFdNTTy>.
- Du, X., Allan, M., Dore, A., Ourselin, S., Hawkes, D., Kelly, J.D., Stoyanov, D., 2016. Combined 2d and 3d tracking of surgical instruments for minimally invasive and robotic-assisted surgery. *International Journal of Computer Assisted Radiology and Surgery* 11, 1109–1119. URL: <https://doi.org/10.1007/s11548-016-1393-4>, doi:10.1007/s11548-016-1393-4.
- Du, X., Kurmann, T., Chang, P.L., Allan, M., Ourselin, S., Sznitman, R., Kelly, J.D., Stoyanov, D., 2018. Articulated multi-instrument 2-d pose estimation using fully convolutional networks. *IEEE Transactions on Medical Imaging* 37, 1276–1287. doi:10.1109/TMI.2017.2787672.
- Everingham, M., Eslami, S.A., Van Gool, L., Williams, C.K., Winn, J., Zisserman, A., 2015. The pascal visual object classes challenge: A retrospective. *International journal of computer vision* 111, 98–136.
- Fan, H., Xiong, B., Mangalam, K., Li, Y., Yan, Z., Malik, J., Feichtenhofer, C., 2021. Multiscale vision transformers, in: *Proceedings of the IEEE/CVF International Conference on Computer Vision*, pp. 6824–6835.
- Feichtenhofer, C., Fan, H., Malik, J., He, K., 2019. Slowfast networks for video recognition, in: *Proceedings of the IEEE/CVF International Conference on Computer Vision*, pp. 6202–6211.
- Fiorini, P., 2021. *Automation and Autonomy in Robotic Surgery*. Springer International Publishing, Cham. pp. 237–255. URL: https://doi.org/10.1007/978-3-030-53594-0_23, doi:10.1007/978-3-030-53594-0_23.
- Fu, Z., Jin, Z., Zhang, C., He, Z., Zha, Z., Hu, C., Gan, T., Yan, Q., Wang, P., Ye, X., 2021. The future of endoscopic navigation: A review of advanced endoscopic vision technology. *IEEE Access* 9, 41144–41167. doi:10.1109/ACCESS.2021.3065104.
- Gao, X., Jin, Y., Long, Y., Dou, Q., Heng, P.A., 2021. Trans-svnet: accurate phase recognition from surgical videos via hybrid embedding aggregation transformer, in: *International Conference on Medical Image Computing and Computer-Assisted Intervention*, Springer. pp. 593–603.
- Gao, Y., Swaroop Vedula, S., Reiley, C., Ahmidi, N., Varadarajan, B., Lin, H., Tao, L., Zappella, L., Béjar, B., Yuh, D., Chiung, C., Chen, G., Vidal, R., Khudanpur, S., Hager, G., 2014. Jhu-isi gesture and skill assessment working set (jigsaws): A surgical activity dataset for human motion modeling. *Modeling and Monitoring of Computer Assisted Interventions (M2CAI) – MICCAI Workshop*.
- García-Peraza-Herrera, L.C., Li, W., Fidon, L., Grijthuijsen, C., Devreker, A., Attilakos, G., Deprest, J., Poorten, E.V., Stoyanov, D., Vercauteren, T., Ourselin, S., 2017. Toolnet: Holistically-nested real-time segmentation of robotic surgical tools, in: 2017 IEEE/RSJ International Conference on Intelligent Robots and Systems (IROS), pp. 5717–5722. doi:10.1109/IROS.2017.8206462.
- Goh, E.Z., Ali, T., 2022. Robotic surgery: an evolution in practice. *Journal of Surgical Protocols and Research Methodologies* 2022, snac003. URL: <https://doi.org/10.1093/jsprm/snac003>, doi:10.1093/jsprm/snac003.
- González, C., Bravo-Sánchez, L., Arbeláez, P., 2020. Isinet: An instance-based approach for surgical instrument segmentation, in: *International Con-*

- ference on Medical Image Computing and Computer-Assisted Intervention, Springer. pp. 595–605.
- Goodman, E.D., Patel, K.K., Zhang, Y., Locke, W., Kennedy, C.J., Mehrotra, R., Ren, S., Guan, M.Y., Downing, M., Chen, H.W., Clark, J.Z., Brat, G.A., Yeung, S., 2021. A real-time spatiotemporal ai model analyzes skill in open surgical videos. *arXiv:2112.07219*.
- Goyal, R., Kahou, S., Michalski, V., Materzynska, J., Westphal, S., Kim, H., Haenel, V., Fruend, I., Yianilos, P., Mueller-Freitag, M., Hoppe, F., Thureau, C., Bax, I., Memisevic, R., 2017. The “something something” video database for learning and evaluating visual common sense, in: 2017 IEEE International Conference on Computer Vision (ICCV), IEEE Computer Society, Los Alamitos, CA, USA. pp. 5843–5851. URL: <https://doi.ieeecomputersociety.org/10.1109/ICCV.2017.622>, doi:10.1109/ICCV.2017.622.
- Grammatikopoulou, M., Flouty, E., Kadkhodamohammadi, A., Quellec, G., Chow, A., Nehme, J., Luengo, I., Stoyanov, D., 2021. Cadis: Cataract dataset for surgical rgb-image segmentation. *Medical Image Analysis* 71, 102053. URL: <https://www.sciencedirect.com/science/article/pii/S1361841521000992>, doi:<https://doi.org/10.1016/j.media.2021.102053>.
- Gu, C., Sun, C., Ross, D.A., Vondrick, C., Pantofaru, C., Li, Y., Vijayanarasimhan, S., Toderici, G., Ricco, S., Sukthandar, R., Schmid, C., Malik, J., 2018. Ava: A video dataset of spatio-temporally localized atomic visual actions, in: Proceedings of the IEEE Conference on Computer Vision and Pattern Recognition, pp. 6047–6056.
- Guan, S., Li, T., Meng, C., Ma, L., 2023. Multi-mode information fusion navigation system for robot-assisted vascular interventional surgery. *BMC Surgery* 23, 51. URL: <https://doi.org/10.1186/s12893-023-01944-5>, doi:10.1186/s12893-023-01944-5.
- He, K., Gkioxari, G., Dollár, P., Girshick, R., 2017. Mask r-cnn, in: Proceedings of the IEEE international conference on computer vision, pp. 2961–2969.
- He, K., Zhang, X., Ren, S., Sun, J., 2016. Deep residual learning for image recognition, in: Proceedings of the IEEE conference on computer vision and pattern recognition, pp. 770–778.
- Huault, A., Sarikaya, D., Le Mut, K., Despinoy, F., Long, Y., Dou, Q., Chng, C.B., Lin, W., Kondo, S., Bravo-Sánchez, L., Arbeláez, P., Reiter, W., Mitsuishi, M., Harada, K., Jannin, P., 2021. Micro-surgical anastomosis workflow recognition challenge report. *Computer Methods and Programs in Biomedicine* 212, 106452. URL: <https://www.sciencedirect.com/science/article/pii/S0169260721005265>, doi:<https://doi.org/10.1016/j.cmpb.2021.106452>.
- Idrees, H., Zamir, A.R., Jiang, Y.G., Gorban, A., Laptev, I., Sukthandar, R., Shah, M., 2017. The thumos challenge on action recognition for videos “in the wild”. *Computer Vision and Image Understanding* 155, 1–23.
- Intuitive Inc., 2014. da vinci si surgical system user manual. <https://fcc.report/FCC-ID/2AAZF-CHB01/2607924.pdf>. [Accessed on 11-12-2023].
- Intuitive Inc., 2023. Da vinci xi system instrument and accessory catalog. <https://www.intuitive.com/en-us/-/media/ISI/Intuitive/Pdf/xi-x-ina-catalog-no-pricing-us-1052082.pdf>. [Accessed 11-12-2023].
- Islam, M., Seenivasan, L., Ming, L.C., Ren, H., 2020. Learning and reasoning with the graph structure representation in robotic surgery, in: Martel, A.L., Abolmaesumi, P., Stoyanov, D., Mateus, D., Zuluaga, M.A., Zhou, S.K., Racoceanu, D., Joskowicz, L. (Eds.), *Medical Image Computing and Computer Assisted Intervention – MICCAI 2020*, Springer International Publishing, Cham. pp. 627–636.
- Jhuang, H., Gall, J., Zuffi, S., Schmid, C., Black, M.J., 2013. Towards understanding action recognition, in: Proceedings of the IEEE international conference on computer vision, pp. 3192–3199.
- Jin, Y., Cheng, K., Dou, Q., Heng, P.A., 2019. Incorporating temporal prior from motion flow for instrument segmentation in minimally invasive surgery video, in: Shen, D., Liu, T., Peters, T.M., Staib, L.H., Essert, C., Zhou, S., Yap, P.T., Khan, A. (Eds.), *Medical Image Computing and Computer Assisted Intervention – MICCAI 2019*, Springer International Publishing, Cham. pp. 440–448.
- Kar, A., Kim, S.W., Boben, M., Gao, J., Li, T., Ling, H., Wang, Z., Fidler, S., 2021. Toronto annotation suite. <https://aidemos.cs.toronto.edu/toras>.
- Karpathy, A., Toderici, G., Shetty, S., Leung, T., Sukthandar, R., Fei-Fei, L., 2014. Large-scale video classification with convolutional neural networks, in: Proceedings of the IEEE conference on Computer Vision and Pattern Recognition, pp. 1725–1732.
- Katić, D., Wekerle, A.L., Görtler, J., Spengler, P., Bodenstedt, S., Röhl, S., Suwelack, S., Kenngott, H.G., Wagner, M., Müller-Stich, B.P., Dillmann, R., Speidel, S., 2013. Context-aware augmented reality in laparoscopic surgery. *Computerized Medical Imaging and Graphics* 37, 174–182. URL: <https://www.sciencedirect.com/science/article/pii/S0895611113000335>, doi:<https://doi.org/10.1016/j.compmedimag.2013.03.003>. special Issue on Mixed Reality Guidance of Therapy - Towards Clinical Implementation.
- Kay, W., Carreira, J., Simonyan, K., Zhang, B., Hillier, C., Vijayanarasimhan, S., Viola, F., Green, T., Back, T., Natsev, P., Suleyman, M., Zisserman, A., 2017. The kinetics human action video dataset. *arXiv:1705.06950*.
- Ke, Y., Sukthandar, R., Hebert, M., 2005. Efficient visual event detection using volumetric features, in: Tenth IEEE International Conference on Computer Vision (ICCV’05) Volume 1, IEEE. pp. 166–173.
- Khatibi, T., 2020. Proposing novel methods for gynecologic surgical action recognition on laparoscopic videos. *Multimedia Tools and Applications* 79, doi:10.1007/s11042-020-09540-y.
- Kim, M.S., Kim, W.J., Hyung, W.J., Kim, H.I., Han, S.U., Kim, Y.W., Ryu, K.W., Park, S., 2019. Comprehensive learning curve of robotic surgery: Discovery from a multicenter prospective trial of robotic gastrectomy. *Annals of Surgery* 273, 949–956. URL: <http://dx.doi.org/10.1097/sla.0000000000003583>, doi:10.1097/sla.0000000000003583.
- Kolbinger, F.R., Bodenstedt, S., Carstens, M., Leger, S., Krell, S., Rinner, F.M., Nielen, T.P., Kircheng, J., Fritzmann, J., Weitz, J., Distler, M., Speidel, S., 2023. Artificial intelligence for context-aware surgical guidance in complex robot-assisted oncological procedures: An exploratory feasibility study. *European Journal of Surgical Oncology*, 106996URL: <https://www.sciencedirect.com/science/article/pii/S0748798323006224>, doi:<https://doi.org/10.1016/j.ejso.2023.106996>.
- Kondo, S., 2021. Lapformer: surgical tool detection in laparoscopic surgical video using transformer architecture. *Computer Methods in Biomechanics and Biomedical Engineering: Imaging & Visualization* 9, 302–307.
- Kuehne, H., Jhuang, H., Garrote, E., Poggio, T., Serre, T., 2011. Hmdb: a large video database for human motion recognition, in: 2011 International conference on computer vision, IEEE. pp. 2556–2563.
- Lanfranco, A.R., Castellanos, A.E., Desai, J.P., Meyers, W.C., 2004. Robotic surgery: A current perspective. *Annals of Surgery* 239. URL: https://journals.lww.com/annalsofsurgery/fulltext/2004/01000/robotic_surgery__a_current_perspective.3.aspx.
- Li, A., Thotakuri, M., Ross, D.A., Carreira, J., Vostrikov, A., Zisserman, A., 2020. The ava-kinetics localized human actions video dataset. *arXiv:2005.00214*.
- Li, F., Zhang, H., Xu, H., Liu, S., Zhang, L., Ni, L.M., Shum, H.Y., 2023. Mask dino: Towards a unified transformer-based framework for object detection and segmentation, in: Proceedings of the IEEE/CVF Conference on Computer Vision and Pattern Recognition, pp. 3041–3050.
- Lin, T.Y., Maire, M., Belongie, S., Hays, J., Perona, P., Ramanan, D., Dollár, P., Zitnick, C.L., 2014. Microsoft coco: Common objects in context, in: Fleet, D., Pajdla, T., Schiele, B., Tuytelaars, T. (Eds.), *Computer Vision – ECCV 2014*, Springer International Publishing, Cham. pp. 740–755.
- Liu, Z., Lin, Y., Cao, Y., Hu, H., Wei, Y., Zhang, Z., Lin, S., Guo, B., 2021. Swin transformer: Hierarchical vision transformer using shifted windows, in: Proceedings of the IEEE/CVF International Conference on Computer Vision, pp. 10012–10022.
- Liu, Z., Ning, J., Cao, Y., Wei, Y., Zhang, Z., Lin, S., Hu, H., 2022. Video swin transformer, in: Proceedings of the IEEE/CVF Conference on Computer Vision and Pattern Recognition, pp. 3202–3211.
- Loshchilov, I., Hutter, F., 2017. SGDR: stochastic gradient descent with warm restarts, in: 5th International Conference on Learning Representations ICLR, OpenReview.net. URL: <https://openreview.net/forum?id=Skq89Scxx>.
- Loshchilov, I., Hutter, F., 2019. Decoupled weight decay regularization, in: International Conference on Learning Representations. URL: <https://openreview.net/forum?id=Bkg6RiCqY7>.
- Maier-Hein, L., Eisenmann, M., Sarikaya, D., März, K., Collins, T., Malpani, A., Fallert, J., Feussner, H., Giannarou, S., Mascagni, P., Nakawala, H., Park, A., Pugh, C., Stoyanov, D., Vedula, S.S., Cleary, K., Fichtinger, G., Forestier, G., Gibaud, B., Grantcharov, T., Hashizume, M., Heckmann-Nötzel, D., Kenngott, H.G., Kikinis, R., Mündermann, L., Navab, N., Onogur, S., Roß, T., Sznitman, R., Taylor, R.H., Tizabi, M.D., Wag-

- ner, M., Hager, G.D., Neumuth, T., Padoy, N., Collins, J., Gockel, I., Goedeke, J., Hashimoto, D.A., Joyeux, L., Lam, K., Leff, D.R., Madani, A., Marcus, H.J., Meireles, O., Seitel, A., Teber, D., Ückert, F., Müller-Stich, B.P., Jannin, P., Speidel, S., 2022. Surgical data science – from concepts toward clinical translation. *Medical Image Analysis* 76, 102306. URL: <https://www.sciencedirect.com/science/article/pii/S1361841521003510>, doi:<https://doi.org/10.1016/j.media.2021.102306>.
- Maier-Hein, L., Vedula, S.S., Speidel, S., Navab, N., Kikinis, R., Park, A., Eisenmann, M., Feussner, H., Forestier, G., Giannarou, S., Hashizume, M., Katic, D., Kennigott, H., Kranzfelder, M., Malpani, A., März, K., Neumuth, T., Padoy, N., Pugh, C., Schoch, N., Stoyanov, D., Taylor, R., Wagner, M., Hager, G.D., Jannin, P., 2017. Surgical data science for next-generation interventions. *Nature Biomedical Engineering* 1, 691–696. URL: <https://doi.org/10.1038/s41551-017-0132-7>, doi:10.1038/s41551-017-0132-7.
- Maier-Hein, L., Wagner, M., Ross, T., Reinke, A., Bodenstedt, S., Full, P.M., Hempe, H., Filimon, D.M., Scholz, P., Tran, T.N., Bruno, P., Kisilenko, A., Müller, B., Davitashvili, T., Capek, M., Tizabi, M.D., Eisenmann, M., Adler, T.J., Gröhl, J., Schellenger, M., Seidlitz, S., Lai, T.Y.E., Roethlingshoefer, V., Both, F., Bittel, S., Mengler, M., Apitz, M., Speidel, S., Kennigott, H., Müller-Stich, B.P., 2021. Heidelberg colorectal data set for surgical data science in the sensor operating room. *Scientific Data* 8, 1–11. URL: <https://api.semanticscholar.org/CorpusID:218538016>.
- Marszalek, M., Laptev, I., Schmid, C., 2009. Actions in context, in: 2009 IEEE Conference on Computer Vision and Pattern Recognition, IEEE. pp. 2929–2936.
- Mascagni, P., Alapatt, D., Sestini, L., Altieri, M.S., Madani, A., Watanabe, Y., Alseidi, A., Redan, J.A., Alfieri, S., Costamagna, G., Boškoski, I., Padoy, N., Hashimoto, D.A., 2022. Computer vision in surgery: from potential to clinical value. *npj Digital Medicine* 5, 163. URL: <https://doi.org/10.1038/s41746-022-00707-5>, doi:10.1038/s41746-022-00707-5.
- Nakawala, H., 2017. Nephrec9. Zenodo doi:<https://doi.org/10.5281/zenodo.1066831>.
- Nwoye, C.I., Gonzalez, C., Yu, T., Mascagni, P., Mutter, D., Marescaux, J., Padoy, N., 2020. Recognition of instrument-tissue interactions in endoscopic videos via action triplets, in: *International Conference on Medical Image Computing and Computer-Assisted Intervention*, Springer. pp. 364–374.
- Nwoye, C.I., Padoy, N., 2023. Data splits and metrics for method benchmarking on surgical action triplet datasets. *arXiv:2204.05235*.
- Nwoye, C.I., Yu, T., Gonzalez, C., Seeliger, B., Mascagni, P., Mutter, D., Marescaux, J., Padoy, N., 2022. Rendezvous: Attention mechanisms for the recognition of surgical action triplets in endoscopic videos. *Medical Image Analysis* 78, 102433. URL: <https://www.sciencedirect.com/science/article/pii/S1361841522000846>, doi:<https://doi.org/10.1016/j.media.2022.102433>.
- Over, P., Fiscus, J., Sanders, G., Joy, D., Michel, M., Awad, G., Kraaij, W., Smeaton, A., Quénot, G., 2013. Trecvid 2013 – an overview of the goals, tasks, data, evaluation mechanisms, and metrics.
- Padoy, N., Blum, T., Ahmadi, S.A., Feussner, H., Berger, M.O., Navab, N., 2012. Statistical modeling and recognition of surgical workflow. *Medical Image Analysis* 16, 632–641. URL: <https://www.sciencedirect.com/science/article/pii/S1361841510001131>, doi:<https://doi.org/10.1016/j.media.2010.10.001>. computer Assisted Interventions.
- Partin, A.W., Wein, A.J., Kavoussi, L.R., Peters, C.A., Dmochowski, R.R., 2020. *Campbell Walsh Urology*, E-Book. Elsevier, Philadelphia.
- Qian, L., Wu, J.Y., DiMaio, S.P., Navab, N., Kazanides, P., 2020. A review of augmented reality in robot-assisted surgery. *IEEE Transactions on Medical Robotics and Bionics* 2, 1–16. doi:10.1109/TMRB.2019.2957061.
- Rassi, I.E., Rassi, J.M.E., 2020. A review of haptic feedback in tele-operated robotic surgery. *Journal of Medical Engineering & Technology* 44, 247–254. URL: <https://doi.org/10.1080/03091902.2020.1772391>, doi:10.1080/03091902.2020.1772391, *arXiv:https://doi.org/10.1080/03091902.2020.1772391*. PMID: 32573288.
- Ren, S., He, K., Girshick, R., Sun, J., 2017. Faster r-cnn: Towards real-time object detection with region proposal networks. *IEEE Transactions on Pattern Analysis and Machine Intelligence* 39, 1137–1149. doi:10.1109/TPAMI.2016.2577031.
- Rodriguez, M.D., Ahmed, J., Shah, M., 2008. Action mach a spatio-temporal maximum average correlation height filter for action recognition, in: 2008 IEEE conference on computer vision and pattern recognition, IEEE. pp. 1–8.
- Roß, T., Reinke, A., Full, P.M., Wagner, M., Kennigott, H., Apitz, M., Hempe, H., Mindroc-Filimon, D., Scholz, P., Tran, T.N., Bruno, P., Arbeláez, P., Bian, G.B., Bodenstedt, S., Bolmgren, J.L., Bravo-Sánchez, L., Chen, H.B., González, C., Guo, D., Halvorsen, P., Heng, P.A., Hosgor, E., Hou, Z.G., Isensee, F., Jha, D., Jiang, T., Jin, Y., Kirtac, K., Kletz, S., Leger, S., Li, Z., Maier-Hein, K.H., Ni, Z.L., Riegler, M.A., Schoeffmann, K., Shi, R., Speidel, S., Stenzel, M., Twick, I., Wang, G., Wang, J., Wang, L., Wang, L., Zhang, Y., Zhou, Y.J., Zhu, L., Wiesenfarth, M., Kopp-Schneider, A., Müller-Stich, B.P., Maier-Hein, L., 2021. Comparative validation of multi-instance instrument segmentation in endoscopy: Results of the robust-mis 2019 challenge. *Medical Image Analysis* 70, 101920. URL: <https://www.sciencedirect.com/science/article/pii/S136184152030284X>, doi:<https://doi.org/10.1016/j.media.2020.101920>.
- Rupprecht, C., Lea, C., Tombari, F., Navab, N., Hager, G.D., 2016. Sensor substitution for video-based action recognition, in: 2016 IEEE/RSJ International Conference on Intelligent Robots and Systems (IROS), pp. 5230–5237. doi:10.1109/IROS.2016.7759769.
- Schoeffmann, K., Taschwer, M., Sarny, S., Münzer, B., Primus, M.J., Putzgruber, D., 2018. Cataract-101: video dataset of 101 cataract surgeries, in: César, P., Zink, M., Murray, N. (Eds.), *Proceedings of the 9th ACM Multimedia Systems Conference, MMSys 2018, Amsterdam, The Netherlands, June 12–15, 2018*, ACM. pp. 421–425. URL: <https://doi.org/10.1145/3204949.3208137>, doi:10.1145/3204949.3208137.
- Schuld, C., Laptev, I., Caputo, B., 2004. Recognizing human actions: a local svm approach, in: *Proceedings of the 17th International Conference on Pattern Recognition, 2004. ICPR 2004.*, IEEE. pp. 32–36.
- Seenivasan, L., Mitheran, S., Islam, M., Ren, H., 2022. Global-reasoned multi-task learning model for surgical scene understanding. *IEEE Robotics and Automation Letters* 7, 3858–3865.
- Sharghi, A., Haugerud, H., Oh, D., Mohareri, O., 2020. Automatic operating room surgical activity recognition for robot-assisted surgery, in: Martel, A.L., Abolmaesumi, P., Stoyanov, D., Mateus, D., Zuluaga, M.A., Zhou, S.K., Racoceanu, D., Joskowicz, L. (Eds.), *Medical Image Computing and Computer Assisted Intervention – MICCAI 2020*, Springer International Publishing, Cham. pp. 385–395.
- Sharma, S., Nwoye, C.I., Mutter, D., Padoy, N., 2023a. Rendezvous in time: an attention-based temporal fusion approach for surgical triplet recognition. *International Journal of Computer Assisted Radiology and Surgery*, 1–7.
- Sharma, S., Nwoye, C.I., Mutter, D., Padoy, N., 2023b. Surgical action triplet detection by mixed supervised learning of instrument-tissue interactions, in: *International Conference on Medical Image Computing and Computer-Assisted Intervention*, Springer. pp. 505–514.
- Shvets, A.A., Rakhlin, A., Kalinin, A.A., Iglvnikov, V.I., 2018. Automatic instrument segmentation in robot-assisted surgery using deep learning, in: 2018 17th IEEE International Conference on Machine Learning and Applications (ICMLA), pp. 624–628.
- Sigurdsson, G.A., Varol, G., Wang, X., Farhadi, A., Laptev, I., Gupta, A., 2016. Hollywood in homes: Crowdsourcing data collection for activity understanding, in: *Computer Vision—ECCV 2016: 14th European Conference, Amsterdam, The Netherlands, October 11–14, 2016, Proceedings, Part I 14*, Springer. pp. 510–526.
- Soomro, K., Zamir, A.R., Shah, M., 2012. Ucf101: A dataset of 101 human actions classes from videos in the wild. *arXiv preprint arXiv:1212.0402*.
- Stauder, R., Ostler, D., Kranzfelder, M., Koller, S., Feußner, H., Navab, N., 2017. The tum lapchole dataset for the m2cai 2016 workflow challenge. *arXiv:1610.09278*.
- Su, Y.H., Huang, I., Huang, K., Hannaford, B., 2018. Comparison of 3d surgical tool segmentation procedures with robot kinematics prior, in: 2018 IEEE/RSJ International Conference on Intelligent Robots and Systems (IROS), pp. 4411–4418. doi:10.1109/IROS.2018.8594428.
- Tanzi, L., Piazzolla, P., Porpiglia, F., Vezzetti, E., 2021. Real-time deep learning semantic segmentation during intra-operative surgery for 3d augmented reality assistance. *International Journal of Computer Assisted Radiology and Surgery* 16, 1435–1445. URL: <http://dx.doi.org/10.1007/s11548-021-02432-y>, doi:10.1007/s11548-021-02432-y.
- Tkachenko, M., Malyuk, M., Holmanyuk, A., Liubimov, N., 2020-2022. Label Studio: Data labeling software. URL: <https://github.com/heartexlabs/label-studio>. open source software available from <https://github.com/heartexlabs/label-studio>.
- Twinanda, A.P., Shehata, S., Mutter, D., Marescaux, J., De Mathelin, M., Padoy, N., 2016. Endonet: a deep architecture for recognition tasks on laparoscopic

- videos. *IEEE transactions on medical imaging* 36, 86–97.
- Valderrama, N., Ruiz Puentes, P., Hernández, I., Ayobi, N., Verlyck, M., Santander, J., Caicedo, J., Fernández, N., Arbeláez, P., 2022. Towards holistic surgical scene understanding, in: Wang, L., Dou, Q., Fletcher, P.T., Speidel, S., Li, S. (Eds.), *Medical Image Computing and Computer Assisted Intervention – MICCAI 2022*, Springer Nature Switzerland, Cham. pp. 442–452.
- Vaswani, A., Shazeer, N., Parmar, N., Uszkoreit, J., Jones, L., Gomez, A.N., Kaiser, Ł., Polosukhin, I., 2017. Attention is all you need. *Advances in neural information processing systems* 30.
- Vining, C.C., Skowron, K.B., Hogg, M.E., 2021. Robotic gastrointestinal surgery: learning curve, educational programs and outcomes. *Updates in Surgery* 73, 799–814. URL: <https://doi.org/10.1007/s13304-021-00973-0>, doi:10.1007/s13304-021-00973-0.
- Wagner, M., Müller-Stich, B.P., Kisilenko, A., Tran, D., Heger, P., Mündermann, L., Lubotsky, D.M., Müller, B., Davitashvili, T., Capek, M., Reinke, A., Reid, C., Yu, T., Vardazaryan, A., Nwoye, C.I., Padoy, N., Liu, X., Lee, E.J., Disch, C., Meine, H., Xia, T., Jia, F., Kondo, S., Reiter, W., Jin, Y., Long, Y., Jiang, M., Dou, Q., Heng, P.A., Twick, I., Kirtac, K., Hosgor, E., Bolmgren, J.L., Stenzel, M., von Siemens, B., Zhao, L., Ge, Z., Sun, H., Xie, D., Guo, M., Liu, D., Kenngott, H.G., Nickel, F., von Frankenberg, M., Mathis-Ullrich, F., Kopp-Schneider, A., Maier-Hein, L., Speidel, S., Bodenstedt, S., 2023. Comparative validation of machine learning algorithms for surgical workflow and skill analysis with the heichole benchmark. *Medical Image Analysis* 86, 102770. URL: <https://www.sciencedirect.com/science/article/pii/S1361841523000312>, doi:<https://doi.org/10.1016/j.media.2023.102770>.
- Wang, Y., Long, Y., Fan, S.H., Dou, Q., 2022. Neural rendering for stereo 3d reconstruction of deformable tissues in robotic surgery, in: *International Conference on Medical Image Computing and Computer-Assisted Intervention*, Springer. pp. 431–441.
- Yeung, S., Russakovsky, O., Jin, N., Andriluka, M., Mori, G., Fei-Fei, L., 2018. Every moment counts: Dense detailed labeling of actions in complex videos. *International Journal of Computer Vision* 126, 375–389.
- Yuan, J., Liu, Z., Wu, Y., 2009. Discriminative subvolume search for efficient action detection, in: *2009 IEEE Conference on Computer Vision and Pattern Recognition*, IEEE. pp. 2442–2449.
- Zhang, H., Li, F., Liu, S., Zhang, L., Su, H., Zhu, J., Ni, L., Shum, H.Y., 2023. DINO: DETR with improved denoising anchor boxes for end-to-end object detection, in: *The Eleventh International Conference on Learning Representations*. URL: <https://openreview.net/forum?id=3mRwyG5one>.
- Zhang, Y., Bano, S., Page, A.S., Deprest, J., Stoyanov, D., Vasconcelos, F., 2022. Large-scale surgical workflow segmentation for laparoscopic sacrocolpopexy. *International Journal of Computer Assisted Radiology and Surgery*, 1–11.
- Zhao, H., Torralba, A., Torresani, L., Yan, Z., 2019. Hacs: Human action clips and segments dataset for recognition and temporal localization, in: *Proceedings of the IEEE/CVF International Conference on Computer Vision*, pp. 8668–8678.
- Zhao, Z., Jin, Y., Heng, P., 2022. Trasetr: Track-to-segment transformer with contrastive query for instance-level instrument segmentation in robotic surgery, in: *2022 International Conference on Robotics and Automation (ICRA)*, pp. 11186–11193. doi:10.1109/ICRA46639.2022.9811873.
- Zhu, X., Su, W., Lu, L., Li, B., Wang, X., Dai, J., 2021. Deformable (detr): Deformable transformers for end-to-end object detection, in: *International Conference on Learning Representations*. URL: <https://openreview.net/forum?id=gZ9hCDWe6ke>.
- Zisimopoulos, O., Flouty, E., Luengo, I., Giataganas, P., Nehme, J., Chow, A., Stoyanov, D., 2018. Deepphase: Surgical phase recognition in cataracts videos, in: *Medical Image Computing and Computer Assisted Intervention – MICCAI 2018: 21st International Conference, Granada, Spain, September 16–20, 2018, Proceedings, Part IV*, Springer-Verlag, Berlin, Heidelberg. p. 265–272. URL: https://doi.org/10.1007/978-3-030-00937-3_31, doi:10.1007/978-3-030-00937-3_31.

Supplementary Material

Appendix A. Original Frame Pre-Processing

We modified the original frames captured by the da Vinci Surgical System. Initially, these frames included black borders at the top and bottom, along with indicators displaying the names of the instruments mounted in the robot and whether they were in use. To remove irrelevant visual information, we cropped all the sampled images to eliminate the black borders and the top and bottom indicators, reducing the frames' dimensions from 1024x1280 to 800x1280. Additionally, we applied black masks over the areas containing instrument names and usage indicators to eliminate potential model biases. The outcomes of these modifications are illustrated in Figure A.1. Our experiments were conducted using the sampled frames that incorporate the abovementioned adjustments. However, we will release both versions of the dataset for possible studies involving the original or the modified frames.

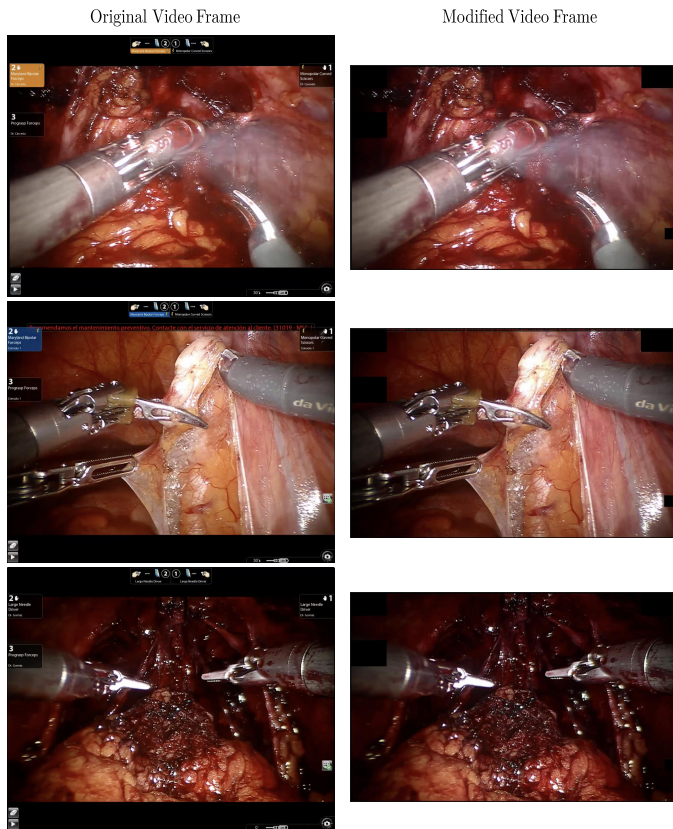


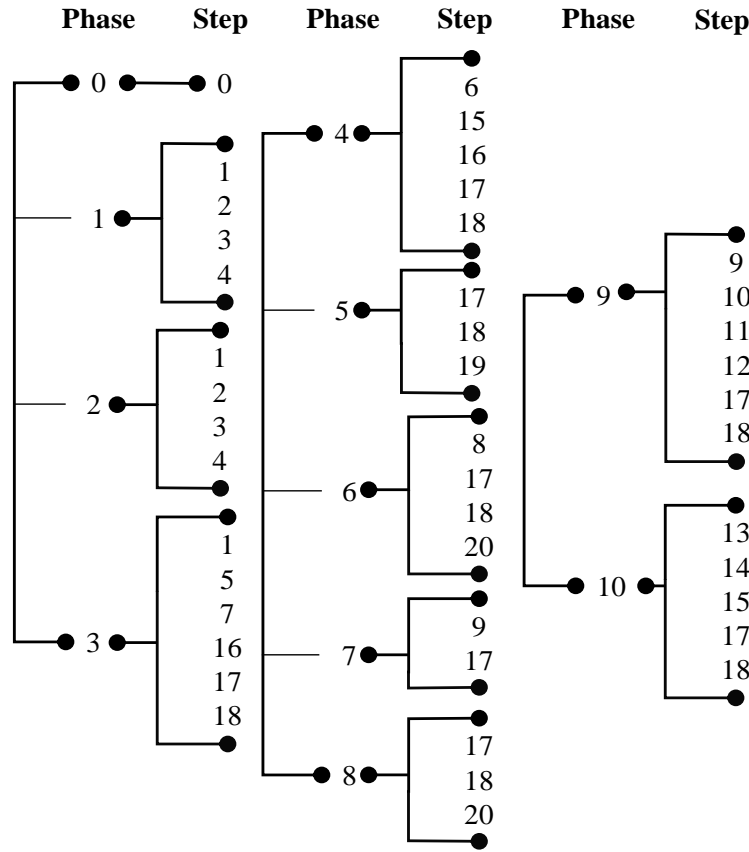
Fig. A.1: **Pre-processing examples of GraSP frames.** We removed the top and bottom black borders, along with the instrument name and usage indicators provided by the capturing system.

Appendix B. GraSP General Overview

We present Figure B.2 to facilitate the interpretation of phase, step, and action categories throughout their corresponding IDs, used in figures and tables along the main body of this work. In addition, the dendrogram aims to show the correspondence between phases and steps. These relationships reflect the usual proceedings inside operating rooms, where every surgical procedure has a “textbook” division into phases, which have themselves a “textbook” division into steps. They are also the results of the surgical team’s efforts to condense their experience into defining a set of processes that span a certain amount of time. Finally, it is essential to highlight the correspondence between the *idle* phase and *idle* step, as it shows that GraSP respects the logical relations between phases and steps. The consistency in the order of appearances of the phases and steps across all videos demonstrates that the GraSP dataset accurately represents the surgical scene.

Furthermore, Figure B.3 illustrates various instances from the GraSP dataset. These examples highlight a substantial diversity in the steps and phases and the relations between long-term and short-term tasks. For instance, in the ligation of the deep dorsal venous complex, completing that phase requires a specific task, such as the tie suture step. The annotations for instrument mask segmentation encompass two Large Needle Drivers, executing hold-still and travel sets of atomic actions. The successful accomplishment of each annotated phase and step crucially depends on using specific instruments and the corresponding actions they perform.

Finally, we display complex frame examples in Figure B.4. The GraSP dataset contains frames introducing diverse challenges, such as small instances of instruments, overlapping instruments, frames obscured by smoke post-cauterization, instances of instruments in varying exposure conditions, instrument occlusion by non-surgical objects, instruments concealed by tissue, and frames overlaid with blood. These examples reflect challenges encountered in surgical procedures and highlight the need to create methods that effectively overcome these complexities.



| Phase | Description | Step | Description |
|-------|--|------|---|
| 0 | Idle | 0 | Idle |
| 1 | Left pelvic isolated lymphadenectomy | 1 | Identification and dissection of the Iliac vein and artery |
| 2 | Right pelvic isolated lymphadenectomy | 2 | Cutting and dissection of the external iliac vein's lymph node |
| 3 | Developing the Space of Retzius | 3 | Obturator nerve and vessel path identification, dissection and cutting of the obturator lymph nodes |
| 4 | Ligation of the deep dorsal venous complex | 4 | Insert the lymph nodes in retrieval bags |
| 5 | Bladder neck identification and transection | 5 | Prevesical dissection |
| 6 | Seminal vesicle dissection | 6 | Ligation of the dorsal venous complex |
| 7 | Development of the plane between the prostate and rectum | 7 | Prostate dissection until the levator ani |
| 8 | Prostatic pedicle control | 8 | Seminal vesicle dissection |
| 9 | Severing of the prostate from the urethra | 9 | Dissection of Denonvilliers' fascia |
| 10 | Bladder neck reconstruction | 10 | Cut the tissue between the prostate and the urethra |

| Instrument ID | Name |
|---------------|---------------------------------|
| 1 | Bipolar Forceps (BF) |
| 2 | Prograsp Forceps (PF) |
| 3 | Large Needle Driver (LND) |
| 4 | Monopolar Curved Scissors (MCS) |
| 5 | Suction Instrument (SI) |
| 6 | Clip Applier (CA) |
| 7 | Laparoscopic Instrument (LI) |

| Action ID | Name | Action ID | Name | Action ID | Name |
|-----------|-----------|-----------|----------------|-----------|---------|
| 1 | Cauterize | 6 | Open | 11 | Still |
| 2 | Close | 7 | Open Something | 12 | Suction |
| 3 | Cut | 8 | Pull | 13 | Travel |
| 4 | Grasp | 9 | Push | 14 | Other |
| 5 | Hold | 10 | Release | | |

Fig. B.2: GraSP classes per task. (Top) phases and steps are presented according to their relations along the dataset. (Bottom) list of the class labels for the phase, step, atomic action recognition tasks, and instrument instance segmentation tasks.


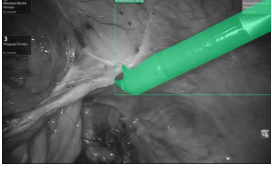

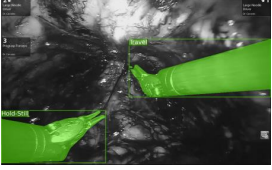

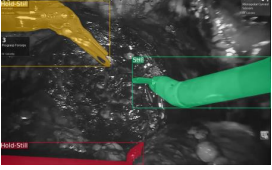
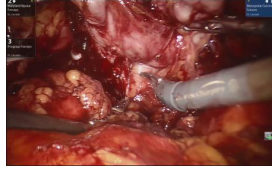
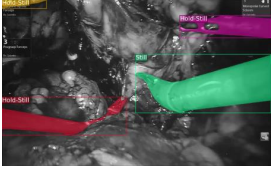
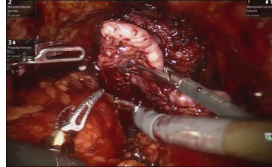
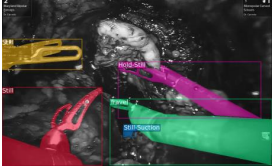
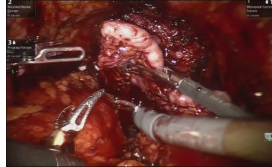
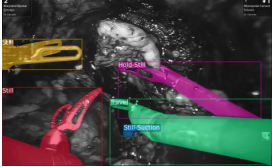
| Phase | Step | Original Image | Mask and Bounding Box Annotation |
|--|-------------------------------------|--|---|
| Developing the Space of Retzius | Prevesical dissection |  |  |
| Ligation of the deep dorsal venous complex | Tie suture |  |  |
| Prostatic pedicle control | Vascular pedicle control |  |  |
| Development of the plane between the prostate and rectum | Dissection of Denonvilliers' fascia |  |  |
| | |  |  |
| Idle | Idle |  |  |

Fig. B.3: Examples of the GraSP dataset, representing original radical prostatectomy image and their corresponding phase, step, instruments segmentation mask, and atomic action annotations.

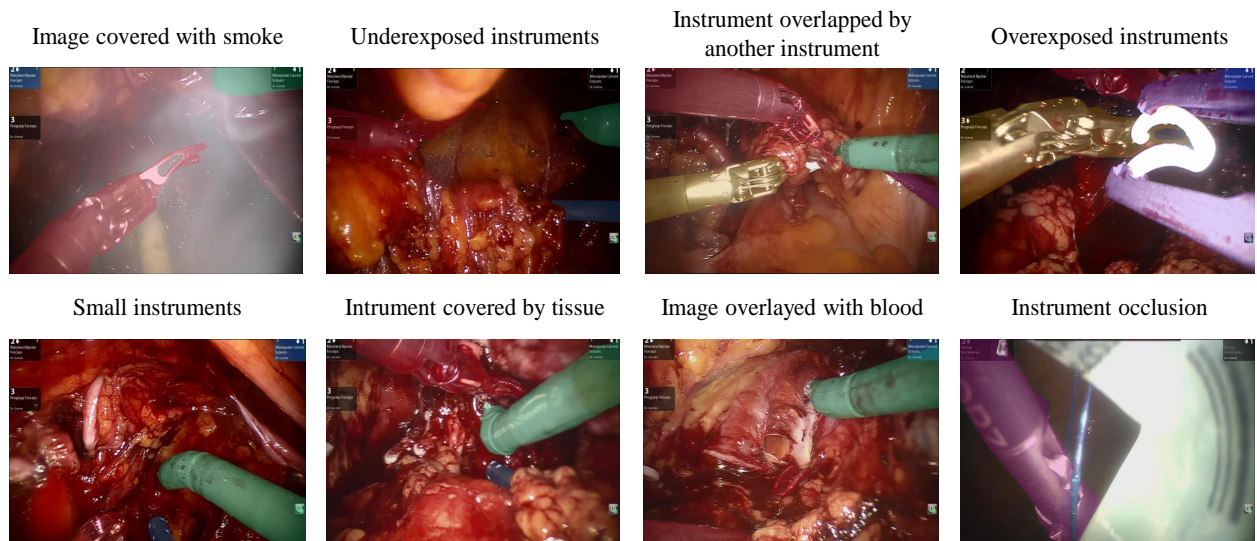


Fig. B.4: Examples of challenging frames in the GraSP dataset overlaid with multi-instance segmentations performed by experts.

Table B.1: **Number of frames sampled at 1fps for each phase in the GraSP dataset.** Phase categories are Idle (0), Left pelvic isolated lymphadenectomy (1), Right pelvic isolated lymphadenectomy (2), Developing the Space of Retzius (3), Ligation of the deep dorsal venous complex (4), Bladder neck identification and transection (5), Seminal vesicle dissection (6), Development of the plane between the prostate and rectum (7), Prostatic pedicle control (8), Severing of the prostate from the urethra (9), and Bladder neck reconstruction (10).

| Set | Phase Category ID | | | | | | | | | | |
|---------------|-------------------|------|------|------|------|------|------|------|------|------|------|
| | 0 | 1 | 2 | 3 | 4 | 5 | 6 | 7 | 8 | 9 | 10 |
| Fold 1 | 9938 | 4752 | 3719 | 4367 | 1355 | 3349 | 2899 | 680 | 1752 | 1198 | 4936 |
| Fold 2 | 8192 | 5815 | 3704 | 4506 | 1234 | 2274 | 2159 | 655 | 2529 | 1431 | 2715 |
| Test | 12934 | 4838 | 3433 | 5317 | 1478 | 2581 | 3608 | 1041 | 3657 | 902 | 3108 |

Table B.2: **Number of frames sampled at 1fps for each step in the GraSP dataset.** Step categories are Idle (0), Identification and dissection of the Iliac vein and artery (1), Cutting and dissection of the external iliac vein’s lymph node (2), Obturator nerve and vessel path identification, dissection, and cutting of the obturator lymph nodes (3), Insert the lymph nodes in retrieval bags (4), Prevesical dissection (5), Ligation of the dorsal venous complex (6), Prostate dissection until the levator ani (7), Seminal vesicle dissection (8), Dissection of Denonvilliers’ fascia (9), Cut the tissue between the prostate and the urethra (10), Hold prostate (11), Insert prostate in retrieval bag (12), Pass suture to the urethra (13), Pass suture to the bladder neck (14), Pull suture (15), Tie suture (16), Suction (17), Cut suture or tissue (18), Cut between the prostate and bladder neck (19), and Vascular pedicle control (20).

| Set | Step Category ID | | | | | | | | | | | | | | | | | | | | |
|---------------|------------------|------|------|------|------|------|-----|------|------|------|-----|-----|-----|-----|------|------|-----|------|------|------|------|
| | 0 | 1 | 2 | 3 | 4 | 5 | 6 | 7 | 8 | 9 | 10 | 11 | 12 | 13 | 14 | 15 | 16 | 17 | 18 | 19 | 20 |
| Fold 1 | 9917 | 3130 | 2605 | 2060 | 676 | 1612 | 377 | 135 | 2739 | 849 | 698 | 118 | 80 | 718 | 1272 | 992 | 712 | 938 | 5120 | 2895 | 765 |
| Fold 2 | 8192 | 4628 | 2109 | 1578 | 1204 | 1009 | 345 | 1233 | 1893 | 908 | 919 | 35 | 128 | 651 | 1163 | 801 | 559 | 1083 | 4292 | 1916 | 568 |
| Test | 12934 | 5340 | 3646 | 1366 | 545 | 630 | 481 | 783 | 3223 | 1112 | 456 | 84 | 62 | 818 | 1228 | 1305 | 491 | 1009 | 3506 | 2486 | 1392 |

Table C.3: **Number of segment instances for each instrument category in the GraSP dataset.** Instrument categories are Bipolar Forceps (BF), Prograsp Forceps (PF), Large Needle Driver (LND), Monopolar Curved Scissors (MCS), Suction Instrument (SI), Clip Applier (CA), and Laparoscopic Graspers/Instruments (LG).

| Set | Instrument Category | | | | | | |
|---------------|---------------------|-----|-----|-----|-----|----|-----|
| | BF | PF | LND | MCS | SI | CA | LG |
| Fold 1 | 876 | 386 | 524 | 915 | 405 | 28 | 101 |
| Fold 2 | 818 | 355 | 372 | 850 | 411 | 36 | 93 |
| Test | 809 | 330 | 449 | 844 | 310 | 38 | 81 |

Table C.4: **Number of annotated frames containing each of the possible amounts of instrument instances present.**

| Set | Number of Instruments | | | | |
|---------------|-----------------------|-----|-----|-----|---|
| | 1 | 2 | 3 | 4 | 5 |
| Fold 1 | 51 | 511 | 492 | 165 | 5 |
| Fold 2 | 65 | 412 | 446 | 172 | 4 |
| Test | 67 | 500 | 442 | 112 | 4 |

Appendix C. Additional GraSP Statistics

Appendix C.1. Frequency Distributions

We extend the statistical analysis of frequency distributions across all tasks within GraSP. Tables C.3, C.5, B.1, and B.2 demonstrate that we maintained the consistency in annotation and distribution throughout the two-fold cross-validation setup and in the test set. These tables show the total number of instances per task in each fold, enabling the identification of over-represented and under-represented instances in each task. This analysis provides insights into their correlation with real-life surgical scenarios.

Table C.4 presents the number of instrument instances per frame distribution. Notably, we observe that 80% of frames contain 2 or 3 instruments, and 95% of frames contain between 2 and 4 instrument instances. These values reflect the standard surgical practice of using multiple instruments to perform complex operations. Nonetheless, using too many instruments can clutter the surgical scene and limit working space. Consequently, across all surgeries analyzed, we find that less than 1% of frames show 5 instruments. Additionally, the frequency of the instrument can be found in Table C.3, displaying the importance of the *Bipolar Forceps* and the *Monopolar Curved Scissors* in the performance of the Radical Prostatectomy surgery. These instruments can execute many actions

(from holding, pulling, and pushing to cutting tissues) required throughout the surgical procedure.

Table C.6 presents the frequency distribution of action combinations in the GraSP dataset. We observe that the most common actions are (*hold, still*), (*still*) and (*travel*). This situation is expected as *still* and *travel* are actions fundamental to describing the activities of all instruments and are constantly and widely performed in any surgery instance. The other action shown here is *hold*. This situation coincides with the action distribution shown in Table C.5 where *hold* is the second most common action. This action cannot be performed alone and, thus, is always combined with another action to describe the activity of an instrument. These action combinations reflect the manipulation of tissues and objects within the surgical scene. We also observe that some sets of actions have a low frequency. These actions correspond to uncommon moves that are nonetheless valid activities that are part of usual procedures and can be seen in other surgeries.

Tables B.1 and B.2 represent the number of annotations for both tasks. The most frequent phase and step corresponds to idle, and this is because it represents the beginning and end points of the surgery and also transition times between other phases and steps.

Table C.5: **Number of instances for each class of the atomic action recognition task.** Action categories are Cauterize (Cau), Close (Clo), Cut (Cut), Grasp (Gra), Hold (Hol), Open (Open), Open Something (O.Sm), Pull (Pull), Push (Pus), Release (Rel), Still (Sti), Suction (Suc), Travel (Tra) and Other (Oth).

| Set | Action Category | | | | | | | | | | | | | |
|--------|-----------------|-----|-----|-----|------|-----|------|-----|-----|-----|------|-----|-----|-----|
| | Cau | Clo | Cut | Gra | Hol | Ope | O.Sm | Pul | Pus | Rel | Sti | Suc | Tra | Oth |
| Fold 1 | 93 | 94 | 50 | 43 | 1175 | 48 | 3 | 132 | 242 | 25 | 1883 | 211 | 838 | 5 |
| Fold 2 | 77 | 75 | 30 | 32 | 1013 | 41 | 15 | 99 | 222 | 25 | 1691 | 188 | 813 | 7 |
| Test | 59 | 71 | 42 | 56 | 923 | 51 | 25 | 108 | 182 | 15 | 1738 | 186 | 737 | 10 |

Table C.6: **Atomic actions combinations frequencies in the GraSP dataset.** We present the number of instances of each possible action combination in GraSP.

| Name | Count | Name | Count | Name | Count |
|-------------------------|-------|--------------------------|-------|-----------------------------------|-------------|
| (Hold, Still,) | 2532 | (Pull,) | 24 | (Close, Cut, Push) | 2 |
| (Still,) | 2311 | (Cauterize, Cut,) | 24 | (Still, Other,) | 2 |
| (Travel,) | 1882 | (Release, Travel,) | 22 | (Hold, Push, Other) | 1 |
| (Push,) | 465 | (Open, Release,) | 22 | (Close, Grasp, Pull) | 1 |
| (Still, Suction,) | 425 | (Open, Release, Travel) | 19 | (Hold, Pull, Other) | 1 |
| (Hold, Pull,) | 266 | (Cauterize, Travel,) | 17 | (Cauterize, Open, Travel) | 1 |
| (Hold, Travel,) | 203 | (Cauterize, Push,) | 14 | (Cauterize, Close, Still) | 1 |
| (Suction, Travel,) | 120 | (Open Something, Pull,) | 13 | (Close, Push) | 1 |
| (Close, Grasp,) | 92 | (Close, Other) | 10 | (Hold, Open Something, Pull) | 1 |
| (Cauterize,) | 89 | (Close, Still,) | 10 | (Push, Other,) | 1 |
| (Hold, Push,) | 70 | (Cauterize, Cut, Push) | 9 | (Cauterize, Open Something, Push) | 1 |
| (Open, Travel,) | 65 | (Cauterize, Hold, Still) | 8 | (Open, Push, Release) | 1 |
| (Close, Travel,) | 43 | (Cauterize, Close,) | 7 | (Open, Open Something,) | 1 |
| (Close, Cut,) | 42 | (Cut, Travel,) | 8 | (Cut, Pull,) | 1 |
| (Push, Suction,) | 40 | (Close, Grasp, Push) | 6 | (Cauterize, Open, Release) | 1 |
| (Grasp, Pull,) | 32 | (Cauterize, Cut, Travel) | 6 | (Cut, Open Something, Push) | 1 |
| (Cauterize, Cut, Close) | 25 | (Open, Push,) | 5 | (Cauterize, Open,) | 1 |
| (Open Something, Push,) | 25 | (Cut, Push,) | 4 | (Open Something, Hold) | 1 |
| (Cauterize, Hold,) | 25 | (Hold, Other,) | 4 | | |
| (Open, Still,) | 24 | (Travel, Other,) | 3 | Total | 9031 |

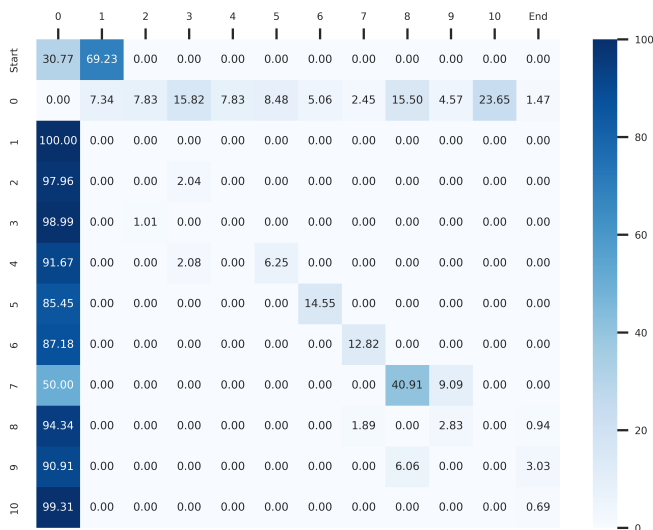


Fig. C.5: **Transition probabilities of phases (%) across the 13 cases.** Each value represents the probability of going from the previous step (rows) to the next step (columns) (e.g., in 50.00% of cases, phase 7 transitions to phase 0, but in 40.91% of cases, it transitions to phase 8).

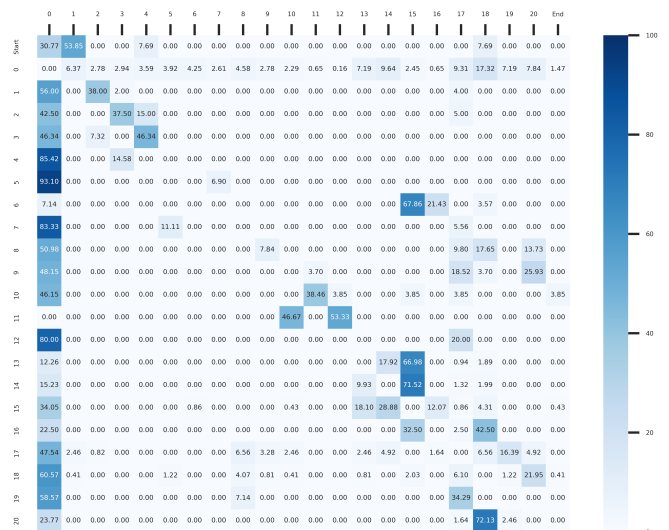


Fig. C.6: **Transition probabilities of steps (%) across the 13 cases.** Each value represents the probability of going from the previous step (rows) to the next step (columns) (e.g., in 15.23% of cases, step 14 transitions to step 0, but in 71.52% of cases, it transitions to step 15).

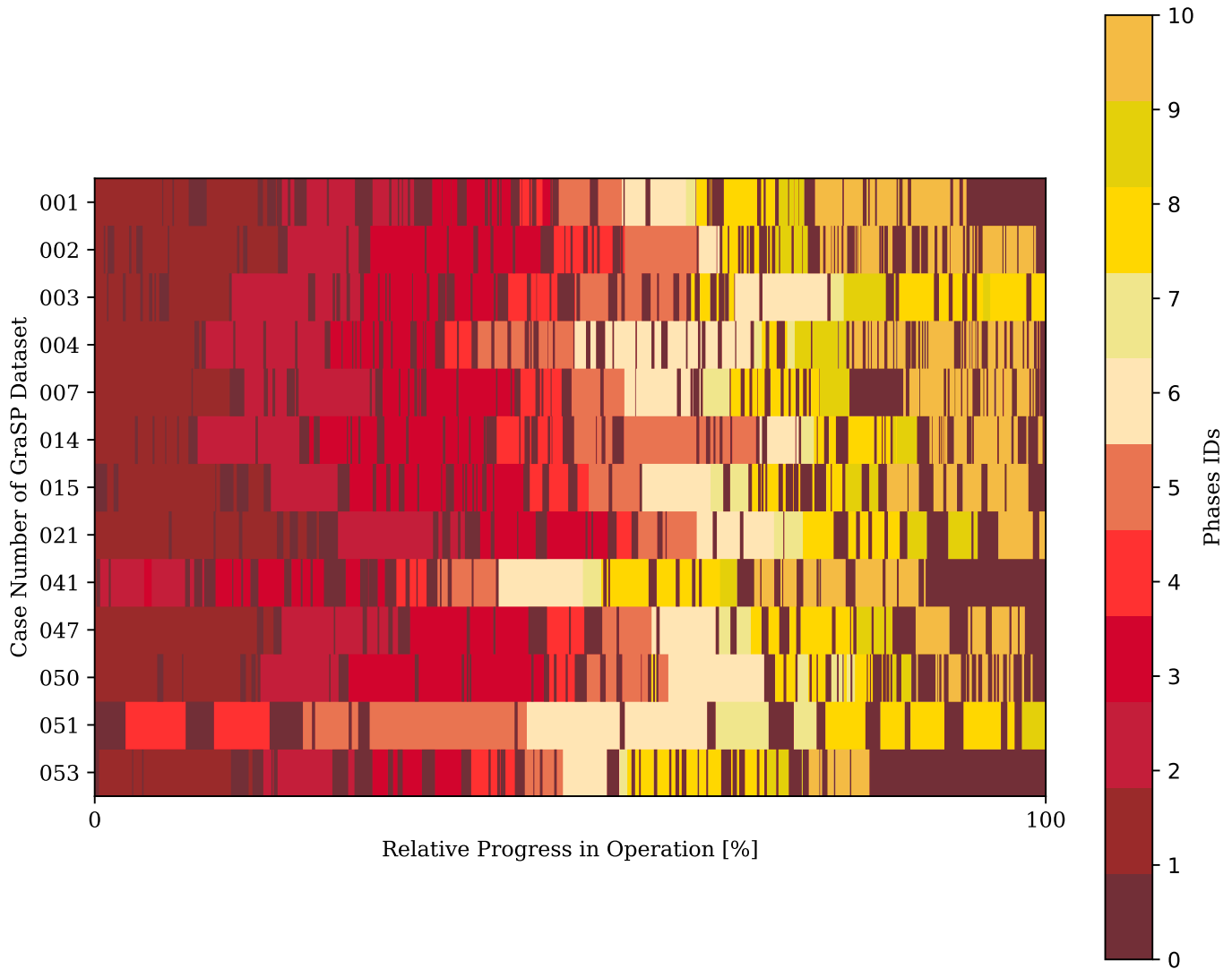


Fig. C.7: **Visual transition of phases in the GraSP dataset.** Each row in the y-axis represents one of the 13 surgeries in GraSP and the x-axis represents the relative temporal progression of the surgery from 0% (start) to 100% (end).

Appendix C.2. Surgical Transitions

Figures C.7 and C.9 show the transitions between phases and steps. These figures show how phase 0 and step 0 are recurrent throughout all surgeries and represent the transition between one step and another and one phase and another. Lastly, both tables and figures exhibit similarity in the order and duration of each phase and step during the temporal progression of the surgeries, hence showing the intrinsic procedural and ordered nature of surgical procedures and proving the consistency in annotation processes for both steps and phase tasks.

The transition matrices in Figures C.5 and C.6 present the transition probabilities of phases and steps across the GraSP dataset. Each value represents the probability of going from the previous step/phase (rows) to the next step/phase (columns). They demonstrate the logical connections between the phases and the steps. For instance, Figure C.5 shows that *Developing the space of Retzius* always follows the *Right pelvic isolated lymphadenectomy*, as defined by the surgical team. There can

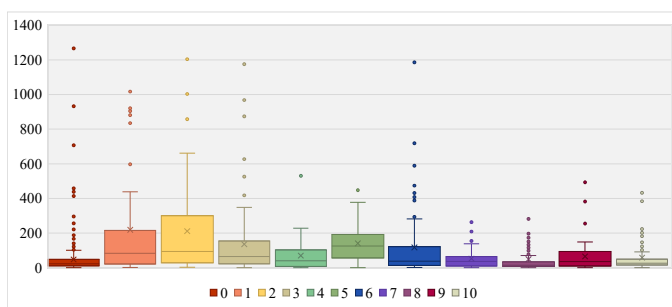


Fig. C.8: **Boxplot distribution of the duration of each phase category.** Each boxplot presents the distribution of the time span in seconds of all the present temporal windows corresponding to each phase category in our dataset. The figure contains the entire duration of each of the classes. The figure is best viewed in color.

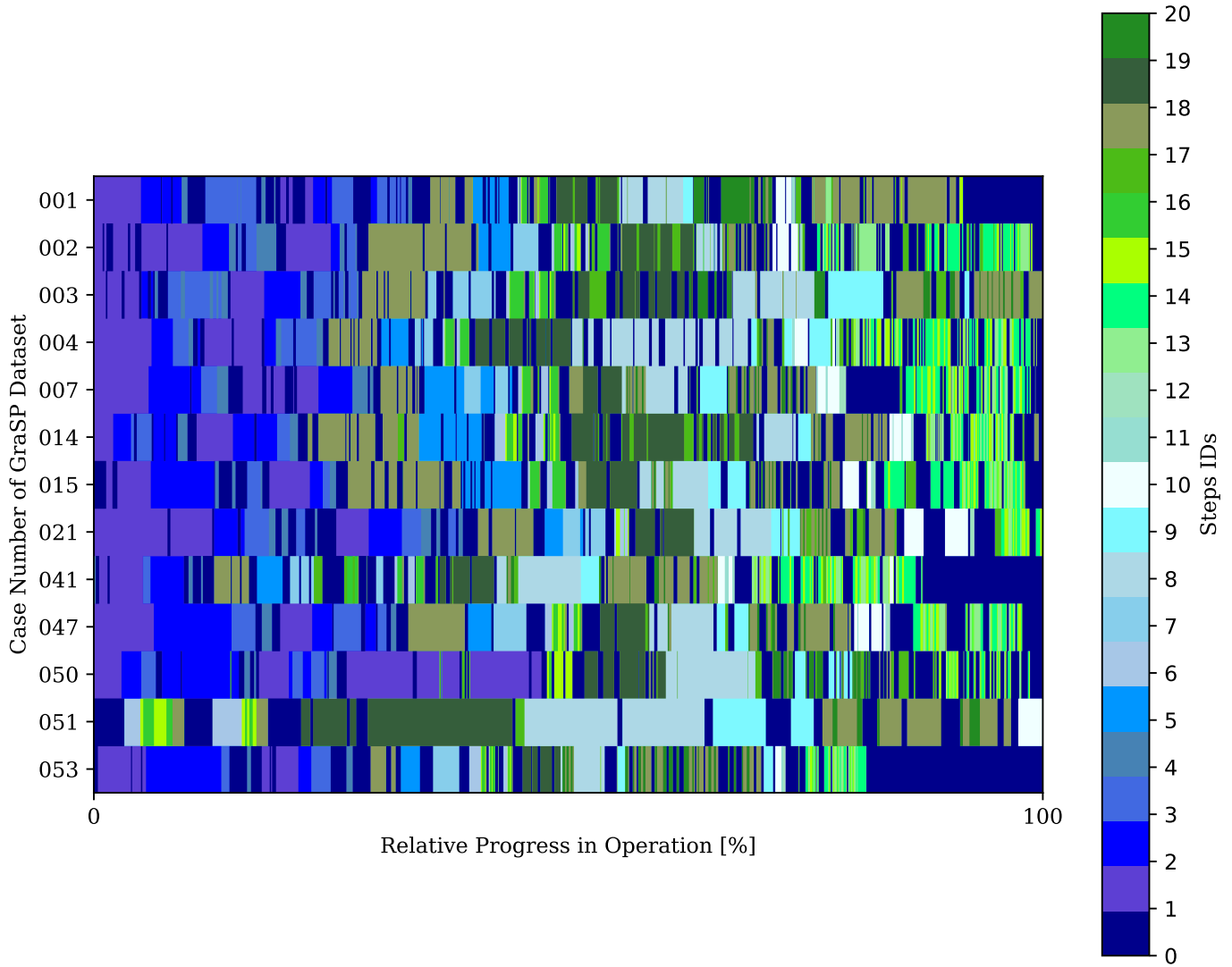


Fig. C.9: **Visual transition of steps in the GraSP dataset.** Each row in the y-axis represents one of the 13 surgeries in GraSP and the x-axis represents the relative temporal progression of the surgery from 0% (start) to 100% (end).

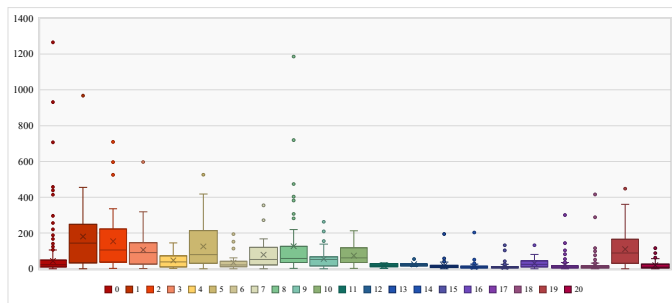


Fig. C.10: **Boxplot distribution of the duration of each step category.** Each boxplot presents the distribution of the time span in seconds of all the present temporal windows corresponding to each step category in our dataset. The figure contains the entire duration of each of the classes. The figure is best viewed in color.

be a pause between the two phases, corresponding to an *Idle* phase. The Figures show that most phases and steps transition from or to an *Idle* and that steps present more variability in their transition probabilities as step categories can show repeatedly throughout the procedure. Additionally, Figures C.8 and C.10 show the complete boxplots of the distribution of the duration of each phase and step categories. Besides the previous analysis in the Dataset Statistics Section, we observe that phase categories present more outliers, tending to have more extensive durations, once again proving the temporal granularity difference between phases and steps, where phases tend to represent broader temporal segments.

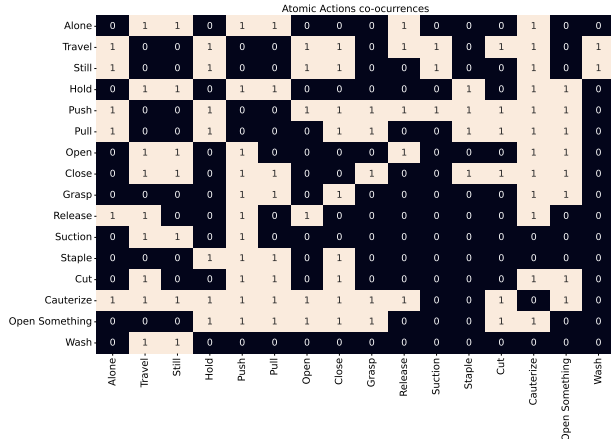


Fig. C.11: Expert-guided theoretical co-occurrences matrices made for annotation's validation. We present the possible co-occurrences between individual atomic actions and between instrument and individual atomic actions in GraSP. Matrix positions with a 1 denote possible co-occurrences of two actions within the same instrument instance or an action with a specific instrument, while a 0 denotes impossible co-occurrence. The *Alone* rows and columns represent whether an action can be performed solely without other simultaneous actions. In our final dataset, we set the Staple and Wash categories as "Other" categories due to the low frequencies of those actions.

Appendix C.3. Co-Occurrence Matrices

Figure C.11 portrays the theoretical matrixes established by the experienced surgical team. These matrices demonstrate possible combinations of actions that can occur simultaneously in the same instrument instance, and also the possible actions that each instrument can perform. We design the matrices to have a predefined *a priori* rule of possible annotations based on the extensive knowledge of our surgeons. We applied this matrix after the first annotation rounds to validate and correct our annotations.

Figures C.12 and C.13 display the inter-task co-occurrence matrices for instruments-phases and instruments-steps. These matrices demonstrate the varying frequency of distinct instruments during different stages of the surgery. Intuitively, the Large Needle Driver (LND) has the highest co-occurrence with the reconstructive phases of the surgeries like the *Ligation of the dorsal venous complex* and *Bladder neck reconstruction* phases, which involve the use of the LND to maneuver the surgical needles and threats to suture, ligate and reconstruct tissue. Hence,

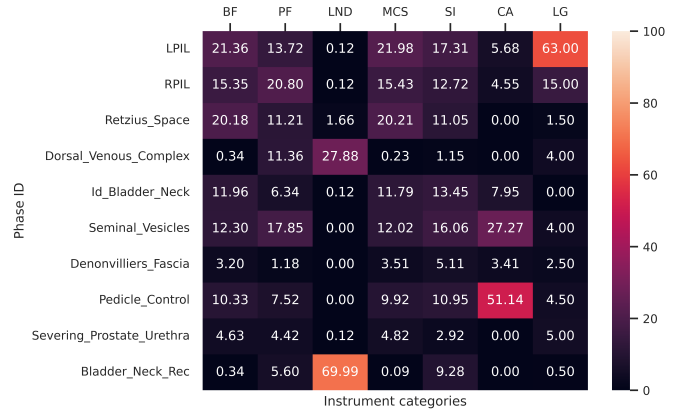


Fig. C.12: Co-occurrence distribution matrix of instruments in function of the surgical phase in GraSP.

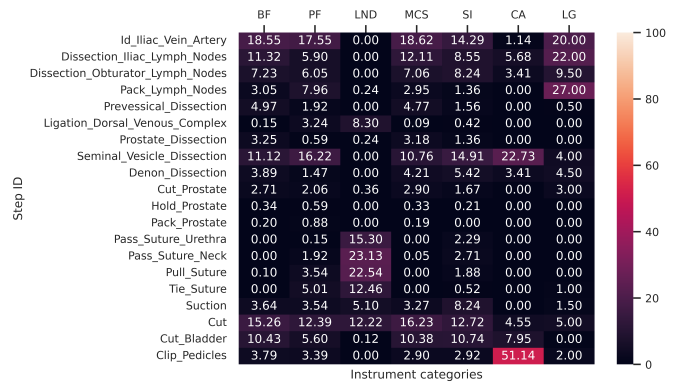


Fig. C.13: Co-occurrence distribution matrix of instruments in function of the surgical step in GraSP.

the LND is also the most frequent in suturing steps like *Pass suture to urethra or bladder neck* and *pull or tie suture*. Similarly, the Bipolar Forceps (BF) and Monopolar Curved Scissors are present in most phases and steps but especially towards phases like *Left or Right pelvic isolated lymphadenectomy*, *Bladder neck identification and transection*, and in steps like *Identification and dissection of the Iliac vein and artery* and *Seminal vesicle dissection*, which are mostly related to tissue manipulation and cutting. Moreover, the Clip Applier (CA) has a very high co-occurrence with the *Prostatic pedicle control* phase and the *Vascular pedicle control* step, which require tissue clipping for bleeding control. Also, the Laparoscopic Graspers/Instruments (LG or LI) show mostly in phases and steps requiring the holding of tissue or retrieval bags. Thus, these matrices again demonstrate the strong correlations between different semantic levels of surgical scene understanding.

The matrix in Figure C.14 presents the co-occurrences between the instruments and atomic actions in the GraSP dataset. In other words, this plot shows the typical functions of every instrument in the RARP instances of GraSP. The columns of the plot do not add to 100%, as instruments can perform up to 3 actions simultaneously. The plot reveals that the Bipolar Forceps usually holds tissues or objects, either in a *still* position or in movement between two locations (*travel*). The Prograsp

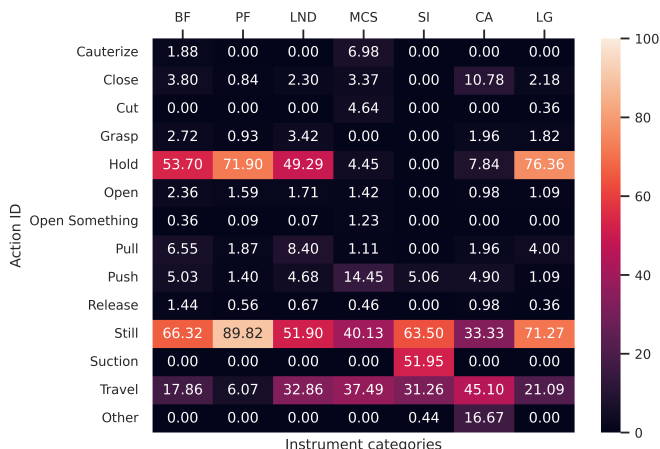


Fig. C.14: Co-occurrence distribution matrix of instruments in the function of atomic actions in GraSP.

Forceps differs from it because of its inability to cauterize. Additionally, it is usually used to hold still bigger tissues in the background passively, which explains why it has the highest realization of *still* and the second highest of *hold*. The Large Needle Driver usually stitches tissues with a needle and thread. As such, it is normal for it to be either still or traveling and holding an object. Because the whole purpose of this instrument is to perform the stitching, it travels more than other instruments with pincers that are sometimes used to hold tissues (such as the Bipolar Forceps, the Prograsp Forceps, or the Laparoscopic Graspers/Instruments). The Monopolar Curved Scissors is the only instrument to be equipped with a tip capable of cutting (apart from a particular type of LI that is observed in one case in the fold 1) and thus has the highest percentage of realization of the action *cut*. It is also one of the two instruments capable of performing *cauterize* (the other being the Bipolar Forceps). This action serves to control and prevent bleeding. The Suction Instrument is the only instrument able to perform *suction* and does it in more than half of the frames in which it is present. The actions it performs in the *other* action are instances of *wash*. The Clip Applier is often performing *close* and *release*. These actions can be seen when it takes hold or releases the tissue it has to staple. This instrument is not often seen in the dataset and appears for a short amount of time. It usually travels to the tissue, staples it, and leaves the frame. While it is there, no other procedure is performed. This specificity in its use explains why it is the instrument with the highest percentage of *travel*. Additionally, the action it performs in the *other* action are instances of *staple*. Finally, the Laparoscopic Instrument has a similar role to the Prograsp Forceps, presenting a similar distribution. Nonetheless, it is slightly more active and has a higher frequency of the *travel* action.

Appendix D. TAPIS performance in GraSP

Instrument segmentation

Figures D.15, D.16, and D.17 depict qualitative segmentation results from TAPIS on the GraSP dataset. As mentioned previously, TAPIS can perform accurate segmentation of complex images. In addition, Figure D.15 shows that TAPIS can segment instances of varying sizes, including bigger instrument arms and small tips. We show examples of inaccurate predictions in Figure D.17. We conduct an error mode analysis and observe cases where two instrument instances are predicted as one, given a high degree of overlap between them (see first row, upper left corner). Second, we observe cases where an instrument is classified as another, given a problematic view of the instrument. For example, the fifth row confuses Bipolar Forceps with Prograsp Forceps. These instruments are similar and difficult to distinguish from a profile view. Third, we observe cases where it wrongly identifies other objects as instruments. For instance, the third row identifies an instrument for recollecting waste as a Laparoscopic Instrument. Additionally, Tables D.7 and D.8 show the per-class results on instrument segmentation explained in the Instrument Segmentation Experiments Section.

Phase and step recognition

On the one hand, Figures D.18 and D.19 present qualitative outcomes of TAPIS in the phase recognition task. Notably, our model encounters challenges in recognizing phases with shorter durations. In instances where recognition occurs, the model tends to identify longer time segments than their actual duration. Conversely, phases with longer durations exhibit more accurate recognition by the model.

On the other hand, Figures D.20 and D.21 illustrate results in the steps recognition task. Notably, the model demonstrates noise in recognizing steps with longer durations while performing well in predicting short steps. Additionally, timestamps may experience shifts, indicating challenges in defining transitions between steps. Tables D.9 and D.10 present the per-class quantitative results on phases and steps recognition as explained in the Phases and Steps Experiments Section.

Action detection

The qualitative performance of TAPIS on the action detection task for the GraSP dataset is illustrated in Figure D.22. The outcomes reveal consistent predictions across various action categories. TAPIS exhibits proficiency in accurately predicting multiple categories for a single instrument, showcasing its capability to comprehend surgical procedures in the short term. However, some inaccuracies are observed in the predictions, including instances of predicting incorrect categories, limiting predictions to a single category when the instrument executes multiple actions, and occasional failure to detect the instrument in the scene.

Table D.7: **Comparative semantic segmentation results of TAPIS in the Instrument Segmentation Task of GraSP.** Instrument categories are Bipolar Forceps (BF), Prograsp Forceps (PF), Large Needle Driver (LND), Monopolar Curved Scissors (MCS), Suction Instrument (SI), Clip Applier (CA), and Laparoscopic Grasper (LG).

| Method | $mAP@0.5IoU_{segm}$ | Instrument Categories | | | | | | |
|---------------------|-------------------------|-----------------------|--------------|--------------|--------------|--------------|--------------|--------------|
| | | BF | PF | LND | MCS | SI | CA | LG |
| ISINet | 78.29 \pm 2.82 | 87.58 | 63.71 | 90.31 | 96.17 | 87.14 | 73.01 | 50.10 |
| QPD Mask DINO | 87.39 \pm 1.75 | 93.78 | 75.34 | 97.75 | 98.04 | 89.24 | 89.44 | 71.13 |
| TAPIS Frame (R50) | 88.65 \pm 1.43 | 93.63 | 75.61 | 97.75 | 98.44 | 89.68 | 89.23 | 76.21 |
| TAPIS Full (R50) | 87.20 \pm 1.12 | 93.25 | 72.73 | 97.76 | 98.48 | 88.73 | 86.64 | 72.81 |
| TAPIS Frame (SwinL) | 91.71 \pm 1.72 | 95.44 | 80.60 | 99.00 | 98.73 | 92.53 | 91.27 | 84.42 |
| TAPIS Full (SwinL) | 90.34 \pm 1.11 | 95.50 | 75.28 | 98.62 | 98.80 | 90.14 | 90.79 | 83.27 |

Table D.8: **Comparative semantic segmentation results of TAPIS in the Instrument Segmentation Task of GraSP.** Instrument categories are Bipolar Forceps (BF), Prograsp Forceps (PF), Large Needle Driver (LND), Monopolar Curved Scissors (MCS), Suction Instrument (SI), Clip Applier (CA), and Laparoscopic Grasper (LG).

| Method | mIoU | IoU | cIoU | Instrument Categories | | | | | | |
|---------------------|-------------------------|-------------------------|-------------------------|-----------------------|--------------|--------------|--------------|--------------|--------------|--------------|
| | | | | BF | PF | LND | MCS | SI | CA | LG |
| TernausNet | 41.74 \pm 5.07 | 24.46 \pm 6.04 | 16.87 \pm 3.70 | 29.24 | 7.28 | 6.60 | 50.20 | 24.69 | 0.00 | 0.04 |
| MF-TAPNet | 66.63 \pm 1.24 | 29.23 \pm 1.43 | 24.98 \pm 0.59 | 48.35 | 9.95 | 12.97 | 67.68 | 28.68 | 1.80 | 5.46 |
| ISINet | 78.44 \pm 1.13 | 70.85 \pm 0.00 | 56.67 \pm 1.46 | 68.89 | 46.29 | 53.37 | 87.09 | 67.70 | 42.87 | 30.52 |
| QPD Mask DINO | 83.89 \pm 1.23 | 82.56 \pm 1.14 | 74.36 \pm 1.04 | 81.60 | 58.10 | 89.06 | 91.80 | 76.77 | 68.27 | 54.90 |
| TAPIS Frame (R50) | 84.81 \pm 1.62 | 81.34 \pm 1.44 | 73.48 \pm 0.88 | 80.61 | 55.08 | 87.04 | 91.85 | 74.58 | 70.09 | 55.09 |
| TAPIS Full (R50) | 84.76 \pm 1.63 | 81.64 \pm 1.45 | 74.43 \pm 0.79 | 80.86 | 56.69 | 87.01 | 91.89 | 74.59 | 72.31 | 57.64 |
| TAPIS Frame (SwinL) | 86.91 \pm 1.59 | 83.92 \pm 0.68 | 77.59 \pm 0.08 | 83.18 | 60.42 | 90.93 | 92.75 | 77.56 | 75.36 | 62.94 |
| TAPIS Full (SwinL) | 87.05 \pm 1.63 | 84.45 \pm 0.72 | 78.82 \pm 0.88 | 83.92 | 62.00 | 91.18 | 92.90 | 77.96 | 78.50 | 65.26 |

Table D.9: **Comparative results of TAPIS in the Phase Recognition Task of GraSP.** Phase categories are Idle (0), Left pelvic isolated lymphadenectomy (1), Right pelvic isolated lymphadenectomy (2), Developing the Space of Retzius (3), Ligation of the deep dorsal venous complex (4), Bladder neck identification and transection (5), Seminal vesicle dissection (6), Development of the plane between the prostate and rectum (7), Prostatic pedicle control (8), Severing of the prostate from the urethra (9), and Bladder neck reconstruction (10).

| Method | mAP (%) | Phase categories (AP %) | | | | | | | | | | |
|-----------|-------------------------|-------------------------|--------------|--------------|--------------|--------------|--------------|--------------|--------------|--------------|--------------|--------------|
| | | 0 | 1 | 2 | 3 | 4 | 5 | 6 | 7 | 8 | 9 | 10 |
| SlowFast | 65.90 \pm 4.99 | 64.94 | 70.93 | 73.74 | 81.14 | 72.89 | 84.36 | 62.24 | 33.03 | 43.82 | 66.05 | 71.74 |
| TAPIS-VST | 64.72 \pm 1.64 | 61.41 | 69.92 | 76.06 | 78.17 | 72.40 | 83.78 | 66.75 | 26.83 | 40.45 | 61.10 | 75.04 |
| TAPIS | 72.90 \pm 1.65 | 70.61 | 78.57 | 77.99 | 87.07 | 82.30 | 86.70 | 72.00 | 27.99 | 57.79 | 79.85 | 81.09 |

Table D.10: **Comparative results of TAPIS in the Step Recognition Task of GraSP.** Phase categories are Idle (0), Identification and dissection of the Iliac vein and artery (1), Cutting and dissection of the external iliac vein's lymph node (2), Obturator nerve and vessel path identification, dissection, and cutting of the obturator lymph nodes (3), Insert the lymph nodes in retrieval bags (4), Prevesical dissection (5), Ligation of the dorsal venous complex (6), Prostate dissection until the levator ani (7), Seminal vesicle dissection (8), Dissection of Denonvilliers' fascia (9), Cut the tissue between the prostate and the urethra (10), Hold prostate (11), Insert prostate in retrieval bag (12), Pass suture to the urethra (13), Pass suture to the bladder neck (14), Pull suture (15), Tie suture (16), Suction (17), Cut suture or tissue (18), Cut between the prostate and bladder neck (19), and Vascular pedicle control (20).

| Method | mAP (%) | Step categories (AP%) | | | | | | | | | | | | | | | | | | | | |
|-----------|-------------------------|-----------------------|--------------|--------------|--------------|--------------|--------------|--------------|--------------|--------------|--------------|--------------|-------------|--------------|--------------|--------------|--------------|--------------|--------------|--------------|--------------|--------------|
| | | 0 | 1 | 2 | 3 | 4 | 5 | 6 | 7 | 8 | 9 | 10 | 11 | 12 | 13 | 14 | 15 | 16 | 17 | 18 | 19 | 20 |
| SlowFast | 42.60 \pm 3.57 | 70.40 | 64.62 | 34.93 | 34.61 | 67.62 | 33.09 | 38.24 | 31.51 | 54.98 | 26.05 | 64.07 | 0.93 | 49.35 | 22.32 | 37.11 | 21.02 | 76.26 | 17.08 | 50.18 | 76.56 | 23.61 |
| TAPIS-VST | 41.02 \pm 1.63 | 66.01 | 65.29 | 31.83 | 34.64 | 76.90 | 33.82 | 48.87 | 31.78 | 69.09 | 18.54 | 67.03 | 2.99 | 50.76 | 12.82 | 32.50 | 12.28 | 46.02 | 11.34 | 55.36 | 79.22 | 14.30 |
| TAPIS | 48.36 \pm 1.14 | 73.14 | 74.15 | 42.22 | 34.92 | 80.18 | 39.30 | 41.60 | 35.83 | 65.32 | 24.48 | 63.62 | 1.35 | 77.41 | 35.49 | 36.68 | 17.88 | 77.34 | 23.13 | 63.56 | 83.41 | 24.47 |

Table D.11: **Comparative results of TAPIS in Atomic Action Detection.** Action categories are Cauterize (Cau), Close (Clo), Cut (Cut), Grasp (Gra), Hold (Hol), Open (Open), Open Something (O.Sm), Pull (Pull), Push (Pus), Release (Rel), Still (Sti), Suction (Suc), Travel (Tra) and Other (Oth).

| Region Proposal Method | $mAP@0.5IoU_{box}$ | Atomic Actions Categories | | | | | | | | | | | | | |
|------------------------|-------------------------|---------------------------|--------------|--------------|--------------|--------------|-------------|--------------|--------------|--------------|-------------|--------------|--------------|--------------|--------------|
| | | Cau | Clo | Cut | Gra | Hol | Ope | O.Sm | Pul | Pus | Rel | Sti | Suc | Tra | Oth |
| Deformable DETR | 28.54 \pm 0.68 | 59.70 | 12.44 | 29.15 | 9.56 | 53.45 | 7.95 | 3.67 | 11.60 | 27.95 | 6.75 | 59.24 | 51.03 | 58.61 | 8.44 |
| DINO | 31.37 \pm 0.50 | 60.97 | 15.73 | 30.06 | 12.03 | 53.28 | 5.52 | 20.60 | 15.08 | 27.74 | 5.54 | 57.47 | 47.72 | 61.88 | 25.61 |
| TAPIS Frame (R50) | 31.24 \pm 1.84 | 54.94 | 14.00 | 18.78 | 13.04 | 66.20 | 3.56 | 9.08 | 15.20 | 28.74 | 2.18 | 71.37 | 57.07 | 60.64 | 22.57 |
| TAPIS Frame (SwinL) | 34.04 \pm 2.40 | 55.56 | 13.65 | 22.68 | 11.30 | 70.78 | 4.53 | 13.82 | 18.25 | 33.16 | 5.21 | 77.76 | 63.12 | 62.66 | 24.10 |

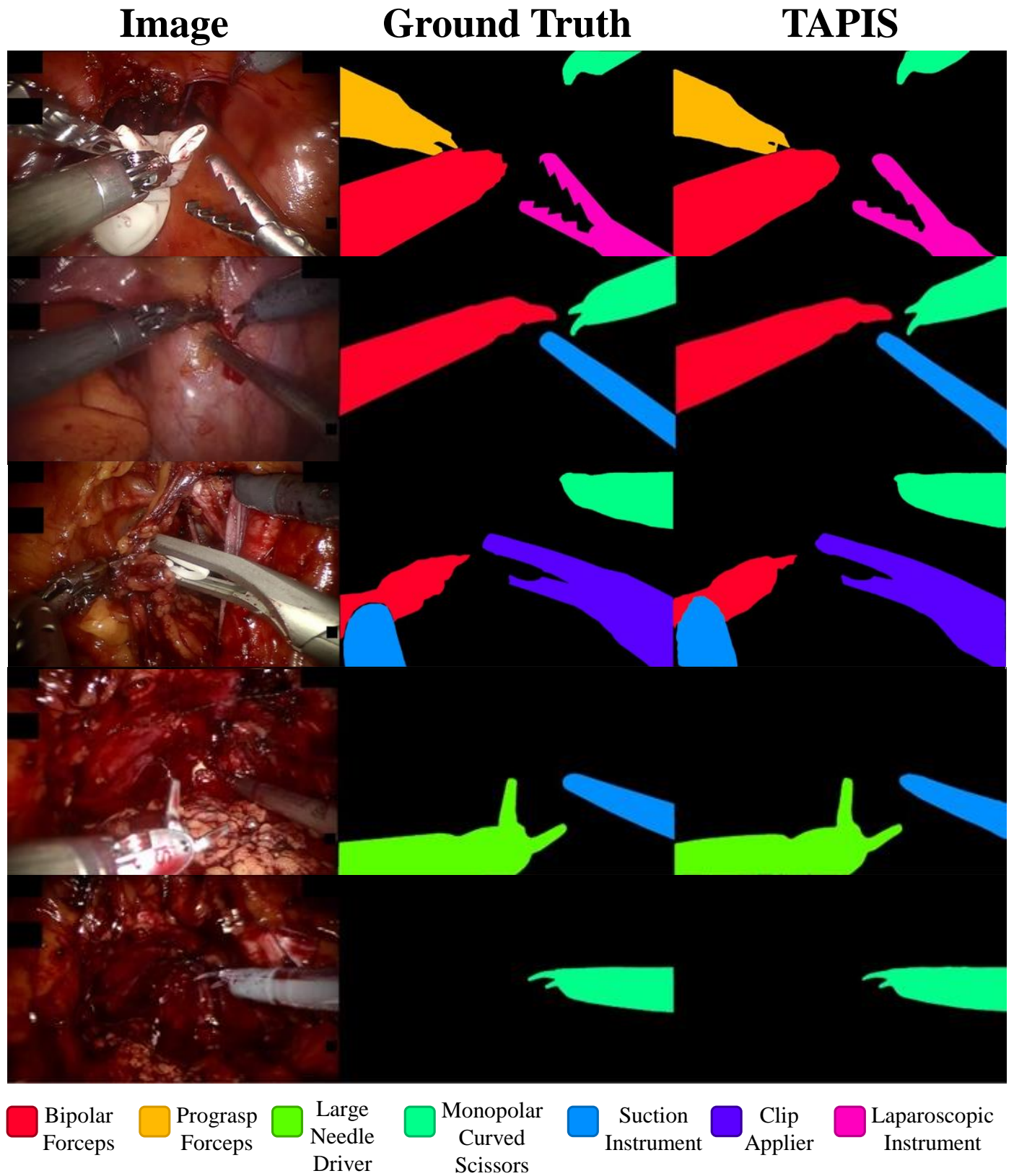


Fig. D.15: **Qualitative instance segmentation performance** comparison between TAPIS and corresponding ground truth. We show examples where TAPIS performs remarkably. The figure is best viewed in color.

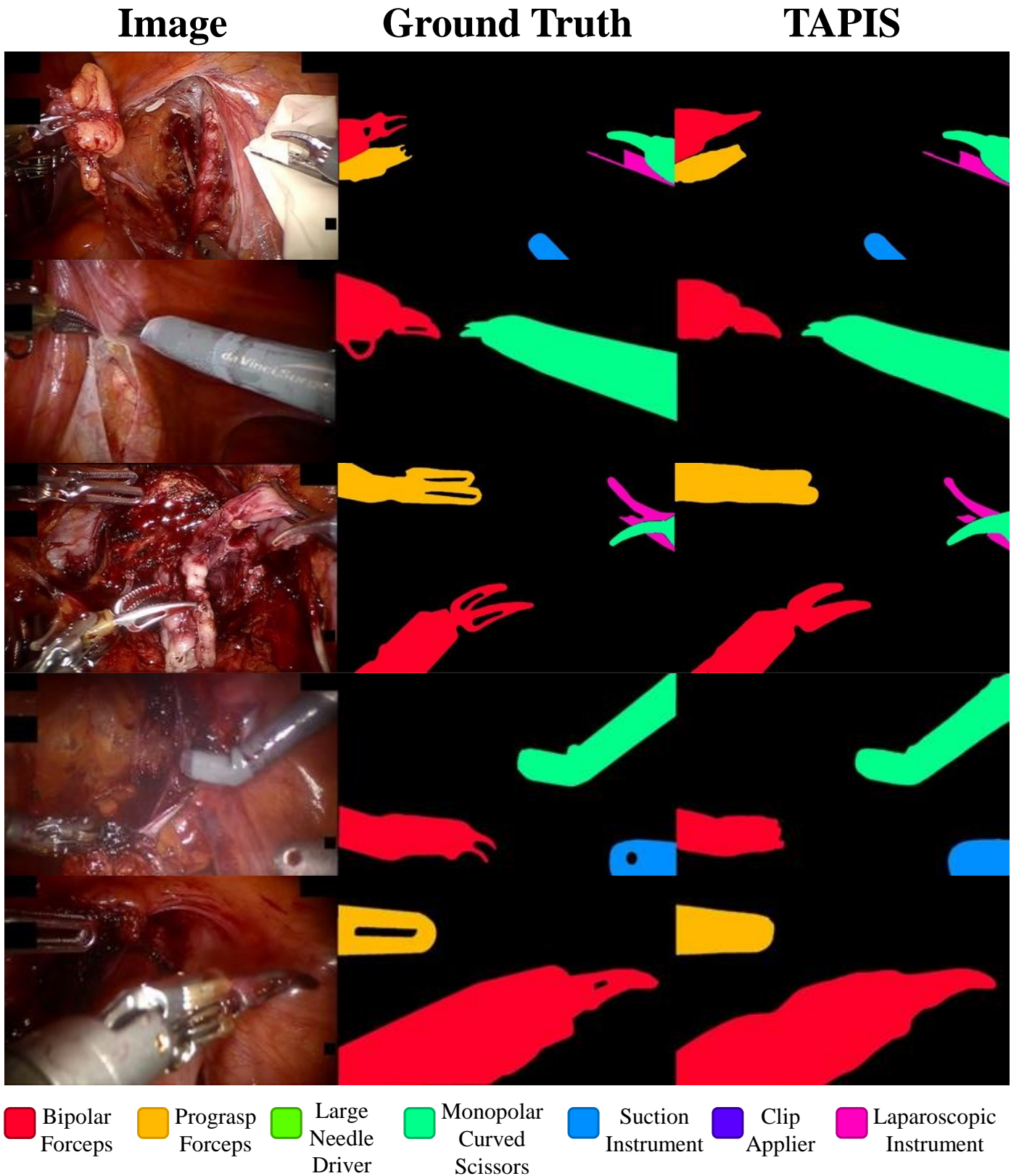


Fig. D.16: **Qualitative instance segmentation performance** comparison between TAPIS and corresponding ground truth. We show examples where TAPIS performs satisfactorily. The figure is best viewed in color.

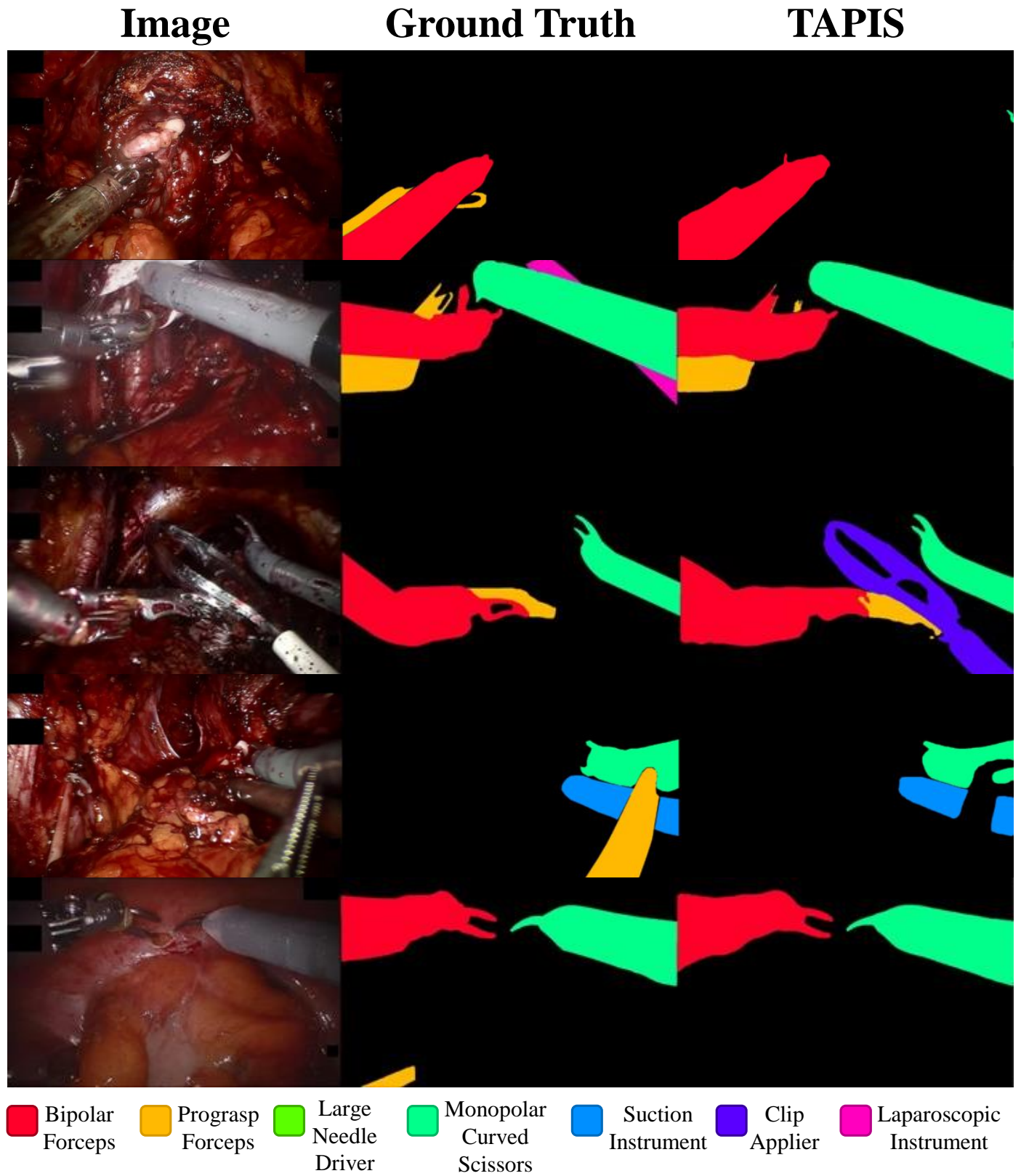


Fig. D.17: **Qualitative instance segmentation performance** comparison between TAPIS and corresponding ground truth. We show examples of TAPIS' error modes. The figure is best viewed in color.

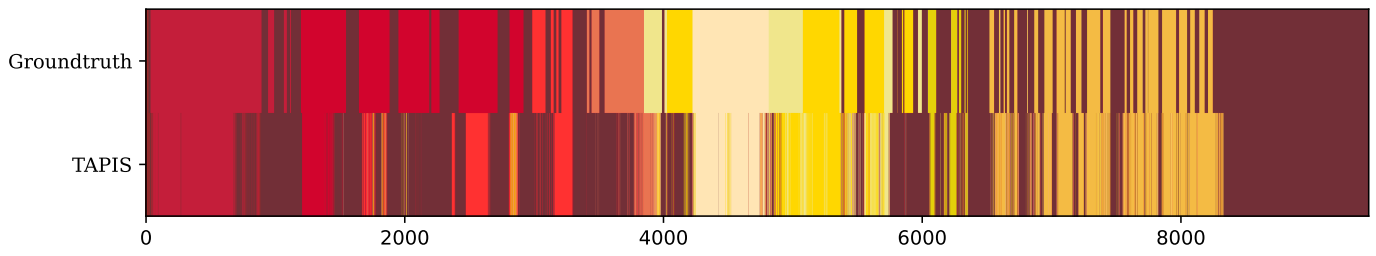


Fig. D.18: **Qualitative phase recognition performance** comparison between TAPIS and the Groundtruth in CASE041.

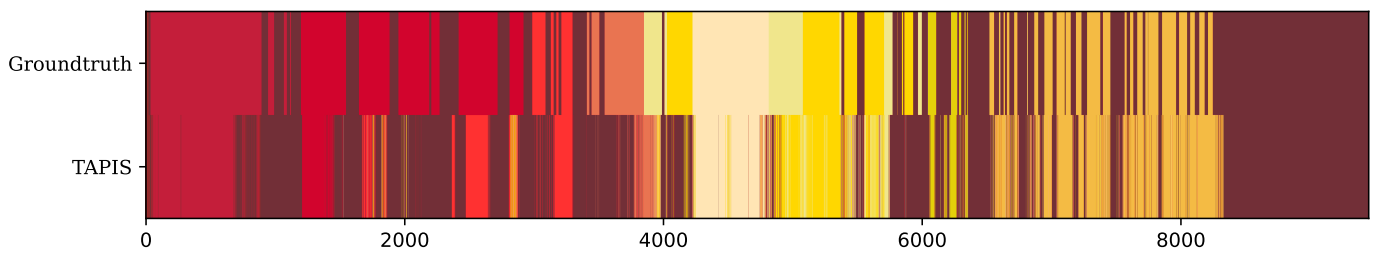


Fig. D.19: **Qualitative phase recognition performance** comparison between TAPIS and the Groundtruth in CASE047.

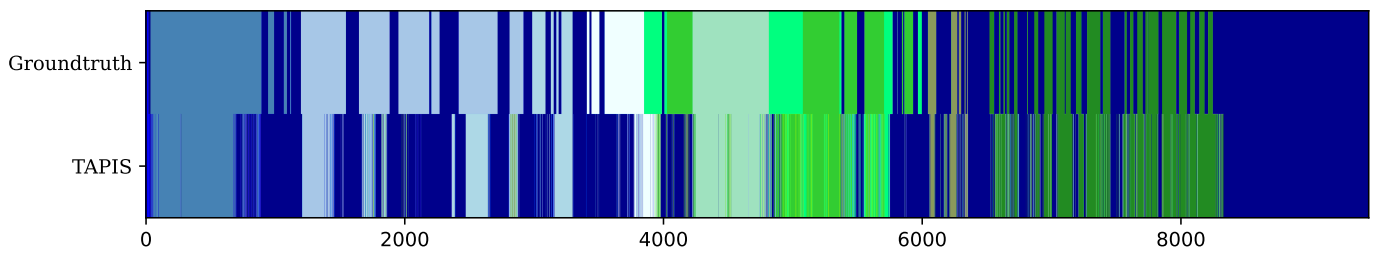


Fig. D.20: **Qualitative step recognition performance** comparison between TAPIS and the Groundtruth in CASE041.

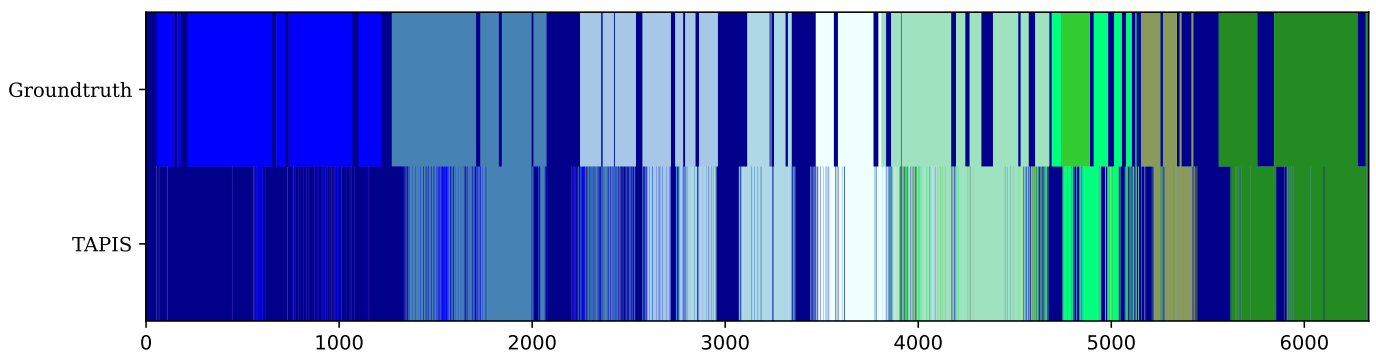


Fig. D.21: **Qualitative step recognition performance** comparison between TAPIS and the Groundtruth in CASE047.

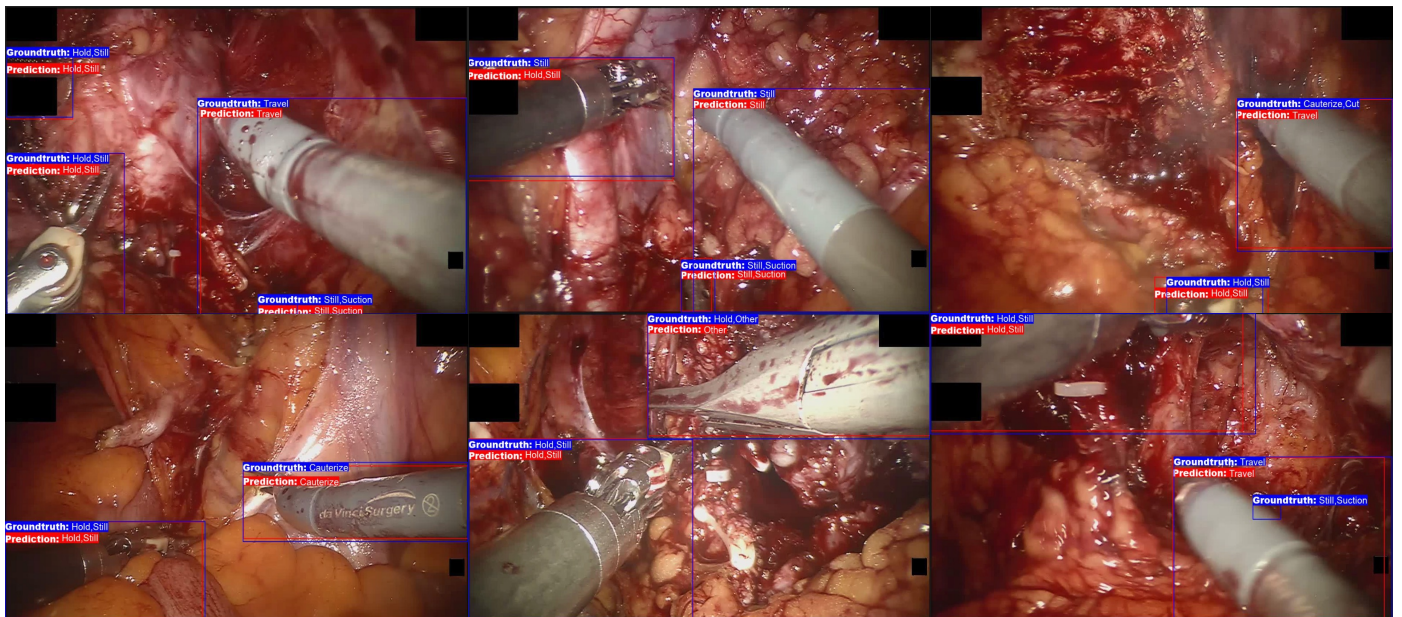


Fig. D.22: **Qualitative action detection performance** comparison between TAPIS and the Groundtruth. The Groundtruth boxes are marked in blue, while the ones predicted by our model are highlighted in red.